Università degli Studi di Ferrara

DOCTORAL COURSE IN PHYSICS

CYCLE XXXV

COORDINATOR Prof. Eleonora Luppi

Performance optimization of metal oxides for gas sensing: the case of WO_3 and SnO_2

Scientific/Disciplinary Sector (SDS) FIS/01

Candidate
Dott. Spagnoli Elena

Supervisor
Prof. Guidi Vincenzo

Year 2019/2022

Questions are seeds of knowledge.
Be curious and your garden will thrive.

Contents

INTRODUCTION AND MOTIVATION 7

CHAPTER 1- CHEMICAL SENSING WITH CHEMORESISTIVE DEVICES 9

1.1 INTRODUCTION TO CHEMORESISTIVE GAS SENSORS 9

1.2 BACKGROUND ON SOLID-STATE PHYSICS 10
1.2.1 Band theory and electronic band structure of solids 10
1.2.2 The surface of semiconductor materials 12

1.3 WORKING PRINCIPLE OF CHEMIRESISTIVE GAS SENSORS 16
1.3.1 Gas diffusion inside a porous layer 16
1.3.2 Solid/gas interfaces: physical and chemical adsorption 18
1.3.3 Influence of adsorbed gas on the conductance of nanostructured porous films 20
1.3.4 Structural parameters of metal oxides controlling gas-sensing properties 23
1.3.5 The thermal activation of metal-oxide sensors 24

1.4 APPLICATIONS FOR CHEMORESISTIVE GAS SENSORS 26
1.4.1 Applications for ethanol sensors 26
1.4.2 Applications for hydrogen sensors 27

CHAPTER 2- MATERIALS AND EXPERIMENTAL METHODS 29

2.1 STATE OF THE ART 29
2.1.1 WO_3 and morphology 29
2.1.2 Solid solutions based on SnO_2 31

2.2 CHEMICALS AND SYNTHESIS OF THE SENSING MATERIALS 32
2.2.1 WO_3 nanoflakes powder 32
2.2.2 SnO_2, $(Sn,Ti)_xO_2$, $(Sn,Ti,Nb)_xO_2$ nanoparticles powders 33

2.3 METHODS FOR MORPHOLOGICAL, CHEMICAL, AND STRUCTURAL CHARACTERIZATION OF SMOX MATERIALS 34
2.3.1 Electron microscopes 34
2.3.2 X-ray powder diffraction 36
2.3.3 X-ray photoelectron spectroscopy 37
2.3.4 Micromeritics automated gas sorptometer 38
2.3.5 Electron paramagnetic resonance spectroscopy 39
2.3.6 UV-visible spectroscopy 40

2.4 PROCESSES FOR THICK FILM SENSORS PREPARATION 42
2.4.1 Screen-printing deposition 42
2.4.2 Sensor final manufacture 43

2.5 SENSORS ELECTRICAL CHARACTERIZATION 44

2.6 *OPERANDO* DRIFT CHARACTERIZATION SETUP 46

CHAPTER 3- CHARACTERIZATION OF THE SENSING MATERIALS 49

3.1 MORPHOLOGICAL, CHEMICAL, AND STRUCTURAL CHARACTERIZATION OF SMOX MATERIALS 49
3.1.1 WO_3 49
3.1.2 $(Sn,Ti,Nb)_xO_2$ 53

3.2 ELECTRICAL CHARACTERIZATION OF SMOX MATERIALS 60
3.2.1 WO_3-based film for ethanol detection 60
3.2.2 $(Sn,Ti,Nb)_xO_2$, $(Sn,Ti)_xO_2$, SnO_2-based film for hydrogen and ethanol detection 64

3.3 DRIFT STUDY ON THE GAS SENSING MECHANISM OF $(Sn,Ti,Nb)_XO_2$ 74

3.4 WO_3 NF AND $(Sn,Ti,Nb)_XO_2$-BASED SENSORS COMPARED TO OTHER SMOX MATERIALS FROM THE LITERATURE 82

CHAPTER 4- GAS SENSING MECHANISM 85

4.1 WO_3 NF- BASED SENSORS 85

4.2 $(Sn,Ti,Nb)_XO_2$-BASED SENSORS 86

CHAPTER 5- CONCLUSIONS AND FUTURE PROSPECTIVES 89

BIBLIOGRAPHY 91

ACTIVITY REPORT 107

Publications 108

Introduction and motivation

In 1938, Wagner and Hauffe found that molecules adsorbed on the surface of semiconductors change their electrical resistance [1]. Then, Heiland [2], Bielanski et al. [3], and Seiyama et al. [4] laid the groundwork for the possible construction of a commercial device based on semiconductors for the detection of gaseous molecules. Metal oxide semiconductor gas sensors have been extensively researched since the pioneering work reported in 1962 by Seiyama et al. [5] and Taguchi [6]. Immediately following the commercialization success of Figaro in 1969, tremendous R&D efforts were expended in this newly emerging field [7]. The research of this period focused not only on experimental investigations, but also on the comprehension of the theoretical basis behind sensor operation. **Chapter 1** summarizes up-to date properties of a semiconductor based on quantum physics and the working principle of chemoresistive gas sensors.

In the late 1980s, the primary application of commercialized semiconducting metal oxides (SMOXs)-based devices was as alarm devices to prevent fires and accidents in habitations through real-time monitoring of the indoor amount of explosive and dangerous gases [8]. Afterwards, the recognized impacts of air pollution on human health, especially in industrial environments such as the chemical, mining, and manufacturing industries, prompted substantial research to identify the safe limits for the exposition of known airborne hazardous chemicals [9]. Legislation imposed numerous significant constraints on industrial activities, including the introduction of gas exposure criteria, such as the threshold limit value (TLV) and short-term exposure limit (STEL), as legal benchmarks for human safety. As a result, the number of applications needing reliable detection of a wide range of gases has increased dramatically. Moreover, recent advances in the miniaturization of SMOX-based gas sensors have significantly reduced their size, production costs and energy consumption, thereby enabling their integration into consumer devices for large-scale applications [10], e.g. emerging technology for the Internet of Things. SMOXs sensors are now used in a wide range of applications, including industrial emission control, household security, vehicle emission control, environmental monitoring and agricultural and biomedical applications. [8]. Many companies now provide types of solid-state sensor, including Figaro, FIS, MICS, UST, CityTech, AppliedSensors, NewCosmos, Alphasense, Sensirion, and others [11].

The increased demand for gas sensors for a wide range of applications has highlighted not only the capabilities of these devices, but also their limitations. Indeed, the new applications require precise sensors, functioning under the effects of interfering agents and complex conditions (e.g. high temperature and pressure), which can affect analyte detection [12]. In addition to distinguishing the gas target from the others being present at the same time, the sensors must detect low levels of its concentration in the surrounding environment and be reproducible across short, medium and long-time periods [8].

SnO_2 is nowadays the most extensively investigated and employed metal-oxide material due to its excellent sensing capabilities, which enable high-sensitivity detection of low concentration levels of various gases. Unfortunately, the high sensitivity of SnO_2 to a wide range of gases makes it inherently unselective and often unsuitable for many an application [8]. The quest for highly selective and high-performance gas sensors encouraged research into new sensing materials. The sensing properties of SMOXs other than SnO_2, such as TiO_2, WO_3, ZnO, Fe_2O_3, and In_2O_3, have been examined. However, as comprehensively discussed in **Chapter 1**, even

though SMOXs are catalytically active, different strategies are required to improve their selectivity and sensitivity.
Two approaches, outlined in "state of the art", **Chapter 2**, were used in this thesis to enhance the sensing capabilities of SMOX films for detecting ethanol and hydrogen, i.e., two analytes of widespread interest for several applications.
The first strategy aimed to control the size and shape of WO_3 nanostructured powders used to produce thick films. Indeed, because several synthesis approaches may be employed to manipulate the crystalline structure and morphological characteristics of this material, it is particularly well suited to being tailored for target gas detection in complex environments. Two-dimensional (2D) WO_3 was evaluated as the most promising for the optimization of active surface area and film porosity for ethanol sensing.
The second approach tuned the chemical composition and structure of SnO_2 through substitution of Sn sites with Ti and Nb in different contents. Ti, Nb and Sn have similar ionic radii and bimetallic oxide solid solution of $(Sn,Ti)_xO_2$ and $(Ti,Nb)_xO_2$ have been claimed to enhance the sensing properties of single oxides, although some limitations remain. Nevertheless, the large number of compositional and structural combinations that these materials offer, makes it possible still unexplored possibilities.
Material productions and experimental methods for their morphological, chemical, structural and electrical characterizations are reviewed in **Chapter 2**, together with the processes for thick-film preparation of the sensors.
Chapter 3 presents the results of the aforementioned characterizations for both the 2D-WO_3 and the $(Sn,Ti,Nb)_xO_2$ solid solution. Sections 3.1.1 and 3.1.2 describe the chemical-physical properties of the two materials, whereas Sections 3.2.1 and 3.2.1 exhibit their sensing capabilities. While the reactions between the target gas and the surface of WO_3 are well documented in the literature, those that occur over $(Sn,Ti,Nb)_xO_2$ are unknown due to the new chemical nature of the material. Therefore, operando Diffuse Reflectance Infrared Fourier Transform (DRIFT)-spectroscopy was employed to explore the interactions between water vapour, ethanol and hydrogen with the surface of the most promising $(Sn,Ti,Nb)_xO_2$ sensors while they were being under operation (Section 3.3). The sensors capability vs. hydrogen and ethanol were compared to that of other semiconducting metal oxides from the literature in section 3.4.
Finally, the detection mechanisms for both the 2D-WO_3 and the $(Sn,Ti,Nb)_xO_2$ films are proposed in **Chapter 4** considering all the evidences from experimental results in **Chapter 3**.
Chapter 5 concludes this thesis by providing a critical assessment of the work done and the results gained, as well as future perspectives on the development of gas sensors based on WO_3 and SnO_2 via morphological and structural engineering.

This thesis has been organized in terms of topics rather than of materials. However, a re-organization of the thesis by materials is possible by first reading all of the sections devoted to WO_3 (n.m.1) and then all of those linked to $(Sn,Ti,Nb)_xO_2$ (n.m.2).

Chapter 1- CHEMICAL SENSING WITH CHEMORESISTIVE DEVICES

1.1 INTRODUCTION TO CHEMORESISTIVE GAS SENSORS

A chemical sensor for gas detection, defined by the International Union of Pure and Applied Chemistry (IUPAC), *"is a device that transforms chemical information, ranging from the concentration of a specific sample component to total composition analysis, into an analytically useful signal"*. They are composed of a receptor and a transducer unit (see **Fig. 1.1 a**). The receptor detects the presence of the gas and transforms a chemical or physical information into a form of energy which is measured by the transducer. The transducer is the unit that transforms the energy, carrying the information about the sample, into a useful analytical signal [13].
Chemical sensors may be classified according to the operating principle of the transducer unit in optical, electrochemical, electrical, mass sensitive, magnetic or thermometric devices. As examples, various types of commercial gas sensors belonging to different classes are depicted in **Fig. 1.1 b**. Among them, electrical sensors are the most simple to develop, and thus have been largely investigated and utilized in practical applications [14]. *"Electrical devices are based on measurements, where no electrochemical processes take place, but the signal arises from the change of electrical properties caused by the interaction of the analyte"* (IUPAC). Chemoresistive sensors, such as metal oxide (MOX) semiconductor-based sensors, belong to this class [13] and the interaction of the gas with the receptor unit is based on reversible redox processes over its surface.

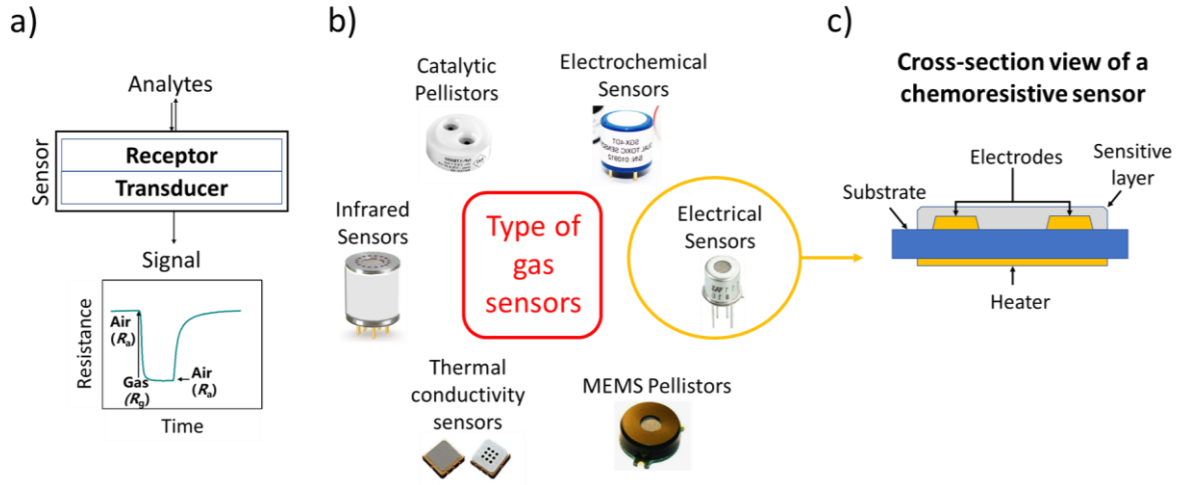

Fig. 1.1 a) Representation of the basic principle of a chemical sensor based on two units: receptor and transducer. The signal of a chemoresistive gas sensor is shown as an example. **b)** Different types of chemical sensors classified according to their operating principle. **c)** Cross-section view of a typical chemoresistive gas sensor.

The chemoresistive sensor typically consists of a sensitive semiconducting layer deposited on the top of a substrate equipped with electrodes used to measure the electrical signal (see **Fig. 1.1 c**). Moreover, the sensitive film is commonly thermo-activated by means of a heater, which is separated from the sensing film by an electrical insulating layer. The technological advancement of this type of sensor aims to improve the efficiency of all its components, i.e.,

sensing layer, substrate, electrodes/heater configuration, in order to reduce their size and energetic consumption, as well as to increase the sensitivity, selectivity and stability of the analyte detection.
This thesis work focused on the optimization of semiconducting metal-oxide (SMOX) films as sensitive layers for gas sensing applications. Therefore, chapter 1 seeks to provide the framework to understand the working principle of SMOX reception, i.e., influence of the adsorbed gas on the conductance of the films. Moreover, structural parameters of metal oxides controlling gas sensing properties will be summarized.

1.2 BACKGROUND ON SOLID-STATE PHYSICS

The unique properties of semiconducting materials enable the development of numerous technological devices. Notably, they are suitable materials for the production of chemically sensitive solid-state sensors since their electrical properties are affected by physical (temperature and light) and chemical (gas composition) changes in the environment. The modern understanding of the properties of a semiconductor relies on quantum physics to explain the movement of charge carriers in a crystal lattice. The following paragraphs discuss the band theory and electronic band structure of the solids in the bulk and at the surface to provide background models describing the properties of semiconductors and, especially, metal-oxide semiconductors.

1.2.1 Band theory and electronic band structure of solids

Semiconductors are materials which have resistivities lying in the range of 10^{-2} and 10^{9} Ω*cm. Their properties are described through the band theory and the electronic band structure of solids.
The band theory in solid-state physics is a theoretical model describing the band of energies permitted in a solid, which are related to the discrete energy levels (allowable states) that electrons may assume in a single, isolated atom according to the four-quantum numbers: the principal quantum number (n), the orbital angular momentum quantum number (l), the magnetic quantum number (m_l) and the electron spin quantum number (m_s). When the atoms are brought together to form a solid, atomic orbitals combine in molecular orbitals (MOs) and the interactions lead to a splitting in energy of each orbital. MOs can be bonding MOs, full of electrons, if there is a constructive interaction between atomic orbitals that lowers the original orbitals energy, or antibonding MOs, empty, if there is a destructive interaction between atomic orbitals that raises the original orbitals energy. As a result of the infinite number of atoms and the consequential number of interacting orbitals that must be considered, the electronic structure can be discussed in terms of energy bands. Therefore, the allowed bonding and antibonding electronic energies fall into different bands of closely spaced levels, where each band is separated by forbidden band gaps.
The highest occupied and the lowest unoccupied energy levels are called respectively valence band (VB) and conduction band (CB). In particular, for metal oxides, the valence band derives from the filled *2p* orbitals of O^{2-}, while the conduction band results from the empty *nd* (*n* from 3 to 5) orbitals of the metal. The energy difference between VB and CB is the energy band gap (Eg), that determines the properties of the material (see **Fig. 1.2 a**). The entity of the energy band gap is determined essentially by the degree of overlap between the atomic orbitals in the

crystal lattice. In general, semiconductors have a band gap that ranges between 0.3 and 3.5 eV and it is temperature-dependent. Indeed, with the increase of the temperature the band gap becomes smaller because the lattice parameter increases due to thermal expansion.
The probability for an electron to occupy an electronic state with energy E is given by the Fermi-Dirac distribution [15]:

$$f(E) = \frac{1}{1 + e^{\frac{(E-E_F)}{kT}}} \qquad eq.1.1$$

where $f(E)$ is the probability that an energy state E will be filled with an electron, k is the Boltzmann's constant, T is the absolute temperature and E_F is Fermi Energy. At absolute zero, the probability of finding an electron would go from 1 in the VB to 0 in the CB. When E is equal to E_F and $T > 0$, $f(E)$ becomes $\frac{1}{2}$, so the Fermi level is the virtual energy level which has 50% of probability to be occupied by electrons.

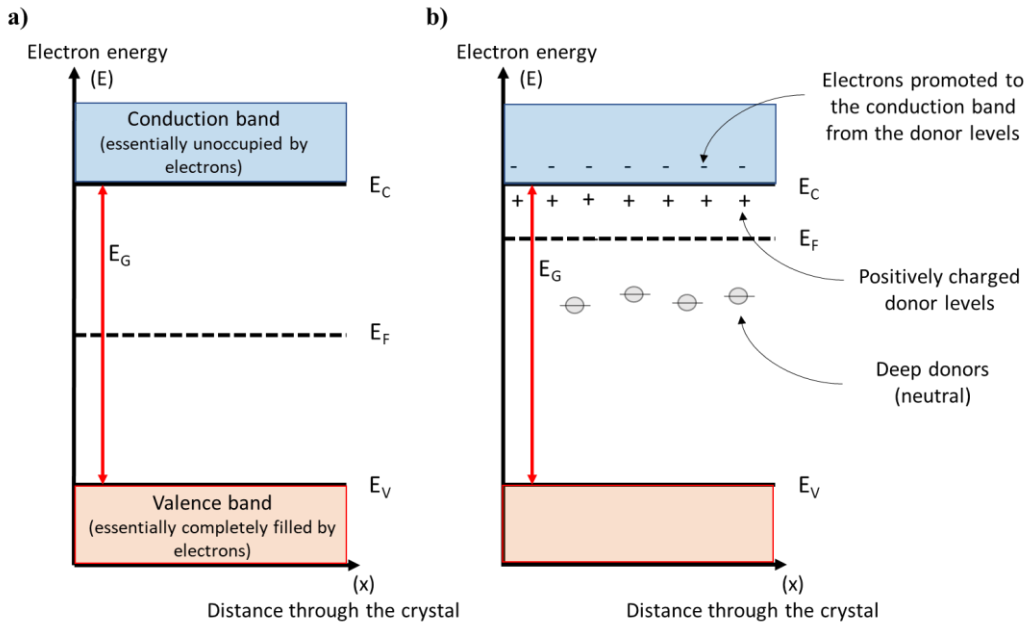

Fig. 1.2. Representation of band gap structure of an **a)** intrinsic and **b)** extrinsic n-type semiconductors.

In intrinsic semiconductors (see **Fig. 1.2 a**), the Fermi level is placed close to the middle of the band gap, since the number of electrons in the CB is equal to the number of holes in the VB. However, the semiconductor lattice usually presents defects, such as impurities, vacancies, e.g., oxygen vacancies in metal oxides, interstitial atoms, and dislocations. Then, the resulting material is known as extrinsic semiconductor. The presence of electron-rich or electron-deficient atoms and defects in the lattice bring to ionizable levels energetically near to the CB or to the VB, respectively. When ionizable levels are energetically near to the CB, as in **Fig. 1.2 b**, thermal excitation of electrons from the donor levels to the CB results in an excess of negative moving carriers (e^-) and the Fermi level moves closer to the CB. The probability of the above-mentioned process depends on the Boltzmann distribution:

$$\frac{N_D^+}{N_D} = e^{\frac{-\Delta E}{kT}} \qquad eq.1.2$$

where N_D is the concentration of donor levels, N_D^+ is the concentration of ionized donors, ΔE is the energetic difference between the CB and the donor levels. Such semiconductors are known as n-type. A similar description could be used to describe the behaviour of p-type semiconductor, in which electrons from the VB are excited to acceptor levels, leading to an excess of positive moving carriers (holes, h^+).
The concentration of electrons, n, in the CB of n-type semiconductors and the concentration of holes, p, in the p-type semiconductors are given by **eq. 1.3** and **1.4**, respectively:

$$n = N_C e^{\frac{-(E_C - E_F)}{kT}} \quad eq.1.3$$

$$p = N_V e^{\frac{-(E_F - E_V)}{kT}} \; eq.1.4$$

where E_C and E_V are the CB and VB edge levels, while N_C and N_V are the effective density of states near to E_C and E_V, respectively.

1.2.2 The surface of semiconductor materials

In addition to three-dimensional electron energy bands and impurity levels in the bulk of the semiconductor, two dimensional localized levels exist in the band gap on the semiconductor surface. The energy levels show acceptor or donor behavior, as they can capture or give up electrons, respectively. Such levels are called surface states ε_{ss} and are classified in two categories according to their origin: surface dangling states, and surface ion-induced states.
Surface dangling states are characteristic of covalent semiconductors, where dangling bonds of surface atoms are present. Usually, the surface reconstruction takes place to reduce the surface energy and the dangling bonds combine with an adjacent dangling bond to form bonding or antibonding levels, which are donor or acceptor levels, respectively.
In ionic semiconductors, the difference between the internal lattice potential and the surface lattice potential creates surface ion-induced states. Surface cation levels provide acceptor levels close to the conduction band, while surface anion levels provide donor levels close to the valence band. So, for metal-oxide semiconductor, the metal can be a cation and have the tendency to capture extra electrons (acts as acceptors), while the oxygen can be an anion and have the tendency to give up electrons (acts as donors).
The surface ion-induced and the surface dangling states may coexist in semiconductors, which are partially ionic and partially covalent, such as transition metal oxides. Moreover, depending on the environment in which the surface is exposed, adsorbed particles and surface films can produce extrinsic surface states.
The range of the concentration of the surface states (density of states, N_S) is from 10^{10} to 10^{14} cm^{-2} which is 1/10 to $1/10^5$ of the concentration of surface atoms (~10^{15} cm^{-2}) [16]. Usually, the concentration of surface state is lower on the smooth surface than on the rough surface.

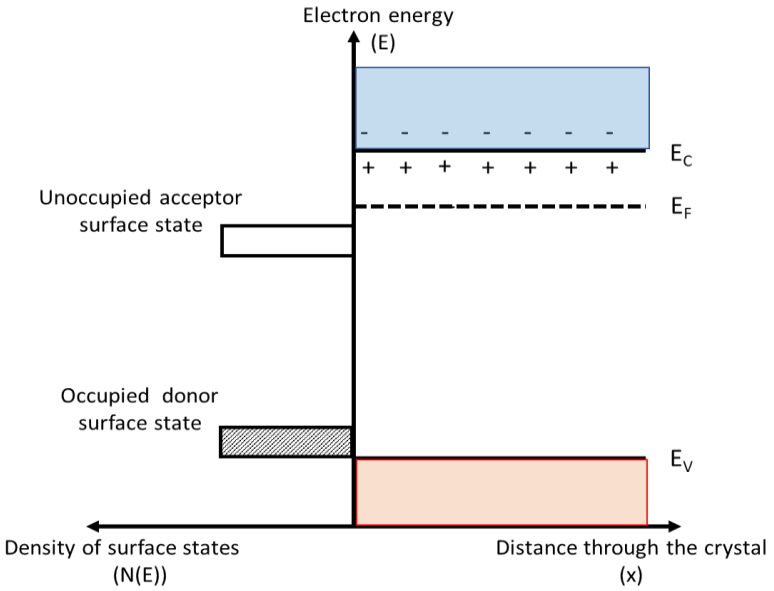

Fig. 1.3. Acceptor and donor state bands at n-type semiconductor's surface. It is assumed that the surface states are neutral, i.e. acceptor states are unoccupied and donor states are occupied [16].

Fig. 1.3 shows the so-called flat-band case, where no net surface charge is present. Unoccupied acceptor and occupied donor surface states are represented as bands because of the heterogeneity of the surface. Indeed, many surface state levels are formed from different crystal planes, surface steps and "terraces", grain boundaries, dislocations, mixed phases, amorphous regions, impurities, patches of oxides or other foreign phase [16]. Consequently, the surface and the interior of the semiconductors can be considered as two distinct entities in contact with each other. Indeed, the interior Fermi level, E_F in **eq. 1.5**, which depends on the bulk impurity concentrations, is different from the surface Fermi level, E_F^S, which depends on the surface states. The Fermi level for the surface with a donor surface state at energy level ε_{ss} and the Fermi level for the surface containing an acceptor surface state at energy level ε_{ss} are express as in **eq. 1.6** and **1.7**, respectively, where N_{ss} is the concentration of the surface state, and ב is a conversion factor between the volume concentration and the surface concentration [15].

$$E_F = \frac{1}{2}(\varepsilon_C + \varepsilon_D) - \frac{1}{2}kTln\frac{2N_C}{N_D} \quad eq.1.5$$

$$E_F^S = \frac{1}{2}(\varepsilon_C + \varepsilon_{ss}) - \frac{1}{2}kTln\frac{N_C}{בN_{ss}} \quad eq.1.6$$

$$E_F^S = \frac{1}{2}(\varepsilon_V + \varepsilon_{ss}) + \frac{1}{2}kTln\frac{N_V}{בN_{ss}} \quad eq.1.7$$

Because E_F must be equivalent to E_F^S, electrons (or holes) transfer between the surface state levels and the CB (or VB) is established until the electron transfer equilibrium. As a result, an electric charge, Q_{SC}, is generated inside the semiconductor and the band level bands downward or upward near the surface forming a space charge layer.

Fig. 1.4 shows a common n-type semiconductor at equilibrium. After electrons move from the donor ions to the surface states through the CB, a double layer is formed. Negatively charged surface states form a negative sheet of charges on the surface, which is exactly compensated by

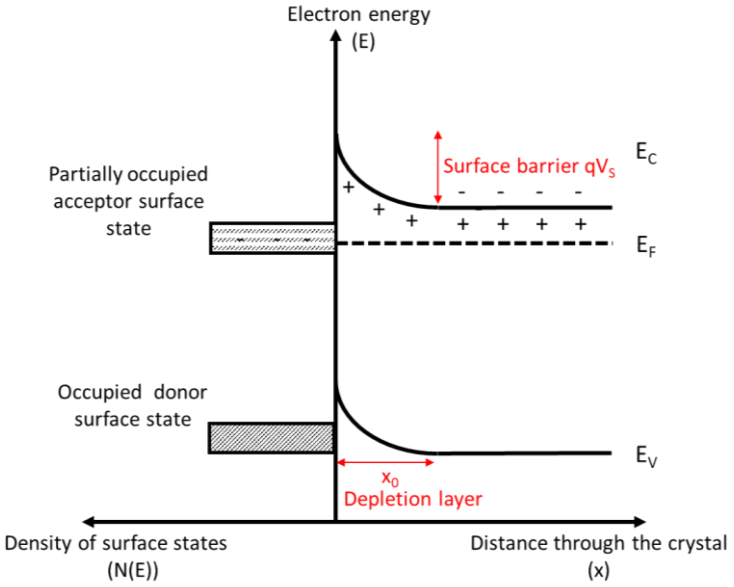

Fig. 1.4 Band model for a depletion layer. Acceptor surface states capture electrons from the conduction bands leading to a negatively charged surface. The counter-charge in the bulk are the positively charged donors near the surface [16]. qV_s is called surface barrier and is due to band banding associated with the surface phenomena.

the positively donor ions in the semiconductor space charge layer. The charge density of ions in the space charge layer is

$$N_i = N_D - N_A \quad eq.1.8$$

where N_D is the donor density and N_A is the acceptor density. Because the space charge layer has been exhausted of all its mobile carriers, which moved to the surface, it is usually called "depletion layer".
The Poisson equation describes the charge density in the space charge layer:

$$\frac{d^2\Phi}{dx^2} = \frac{qN_i}{\varepsilon\varepsilon_0} \quad eq.1.9$$

considering the potential Φ, which is in function of the distance through the space charge layer, ε the dielectric constant of the semiconductor, and ε_0 the permittivity of free space [16]. To continue the discussion with the formalism of the band diagram, it is useful to define the parameter $V(x)$ as:

$$V(x) = \Phi_b - \Phi(x) \quad eq.1.10$$

where Φ_b is the potential in the bulk of the semiconductor. So, from the first and the second integration of the Poisson's equation we obtain:

$$\frac{dV}{dx} = \frac{qN_i(x - x_0)}{\varepsilon\varepsilon_0} \quad eq.1.11$$

$$V = \frac{qN_i(x - x_0)^2}{2\varepsilon\varepsilon_0} \quad eq.1.12$$

where x_0 is the thickness of the space-charge region. For **eq. 1.11**, at $x = x_0$ there is the boundary condition in which $\frac{dV}{dx} = 0$. When $x \geq x_0$, the semiconductor is uncharged, while $\frac{dV}{dx} \neq 0$ when $x < x_0$. From **eq. 1.12** the value of the surface barrier, V_s, also called Schottky barrier, is extracted at x = 0:

$$V_s = \frac{qN_i{x_0}^2}{2\varepsilon\varepsilon_0} \quad eq.1.13.$$

For n-type semiconductor, the number of ions per unit area $N_i x_0$ is equal to the number of donors per unit area $N_D x_0$. Considering all donors ionized, $N_D x_0$ is equal to the number of electrons that are extracted from the CB in the surface region of thickness x_0, that is equal to the number of electrons moved to the surface (N_S):

$$N_i x_0 = N_S \quad eq.1.14$$

Then, V_s can be written in function of N_S:

$$V_s = \frac{q{N_s}^2}{2\varepsilon\varepsilon_0 N_i} \quad eq.1.15$$

The energy difference qV_s of electrons between the surface and the bulk is represented in **Fig. 1.4**.

Considering the **eq. 1.3** multiplied by the Boltzmann factor involving qV_s, the density of electrons at the surface of an n-type semiconductors (n_s) is:

$$n_s = N_C e^{\frac{-(qV_s+\varepsilon_C-\varepsilon_F)}{kT}} \quad eq.1.16$$

In addition to the depletion layer, the surface can also form an accumulation or an inversion layer, as schematically represented in **Fig. 1.5** for n-type semiconductors. The surface forms an accumulation layer when the surface states are near or within the majority carrier band, e.g. donor level near to the CB in **Fig. 1.5 a**, and the majority carriers are injected rather than extracted. On the other hand, the inversion layer arises when strong acceptor surface states extract electrons from the VB, as in **Fig. 1.5 b**, and a double layer appears between the positively

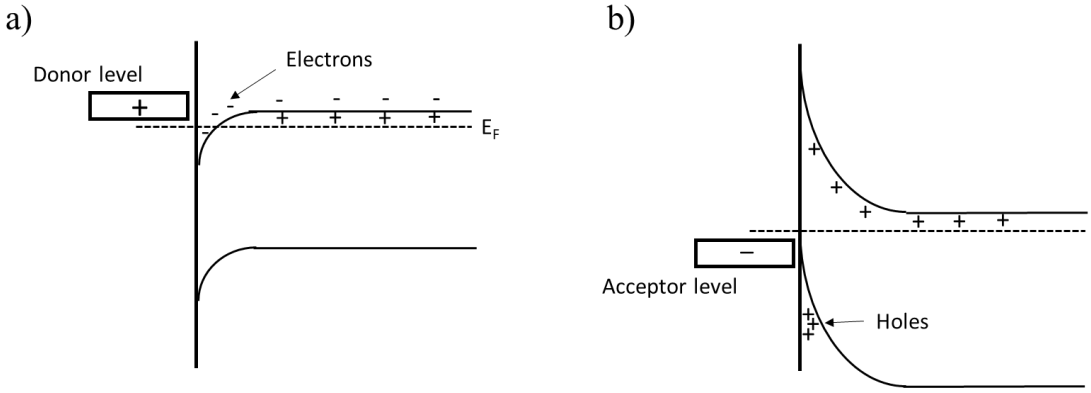

Fig. 1.5 Band model for **a)** an accumulation and **b)** an inversion layer due to the presence of strong acceptor [16].

charged donors and charged holes near the surface and the very negative surface charge. These scenarios will not be extensively discussed because they rarely occur in gas sensors.

1.3 WORKING PRINCIPLE OF CHEMIRESISTIVE GAS SENSORS

The reception by SMOX-based gas sensors of gas molecules in the surrounding atmosphere is strongly related to the formation of adsorbates on the surface of the active material. The following paragraphs describe the gas diffusion inside the porous layer, its adsorption and the influence of the solid/gas interface on the semiconductor properties, i.e. transduction process. In the end, the main structural parameters controlling the gas sensing properties of a SMOX-based sensor and the influence of the operating temperature on the sensitivity and the selectivity will be summarized.

1.3.1 Gas diffusion inside a porous layer

The sensitive metal-oxide film can be deposited as a compact or porous layer [17]. In compact layers, the analyte interaction occurs only at the geometric surface because the gas cannot penetrate the sensing film. On the contrary, in porous layers the volume of the film is also accessible to the gas, leading to a much higher active surface than that of compact layers.
Commonly, nanostructured films are preferred over dense films to maximize the surface-to-volume ratio in contact with the gases. Then, gaseous species diffusion along the pores of the layer affects the active SMOX surface exploited for chemical reactions, i.e., the process that eventually generates the sensor signal.
Porous materials are classified as microporous, mesoporous, or macroporous based on pore width, according to International Union of Pure and Applied Chemistry (IUPAC) [18]. The micropore width does not exceed about 2 nm, the mesopore width is between 2 and 50 nm, and the macropore width is greater than 50 nm. The pore size depends on the dimension and shape of the nanostructures which compose the film. Conventional sol-gel syntheses yield particles with limited sizes in the nanometer range and (typically) approximately spherical shape [19]. As a result, this morphology is usually referred for a general explanation of the phenomena underlying the sensing mechanism. **Figure 1.6 a** shows a schematic drawing of a section of the sensing film composed of spherical particles loosely packed, with infinite small contact areas between each other [19]. In this configuration, increasing particles size leads to larger pore, but smaller specific surface area. Furthermore, in practice, the film is commonly calcined at high temperatures, such as 450-650°C, to obtain a sufficiently stable porous network. As shown in **Fig. 1.6 b**, the sintering process increases the degree of particle interconnectivity required for electronic conductance while decreasing the specific surface area. Then, the most common pore size in SMOX film is in the range of meso-macropore width, with non-ordered pore morphology [19].

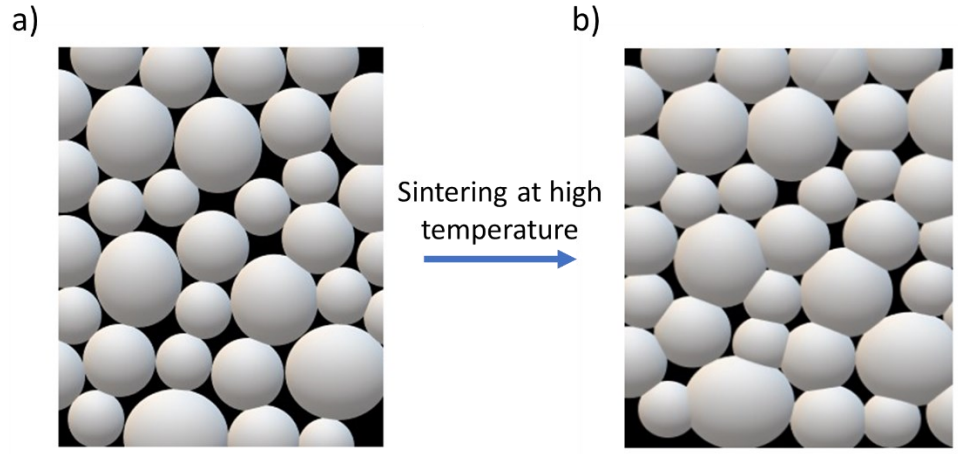

Fig. 1.6 Schematic drawing of a section of the sensing film composed of nanoparticles, representing the mutual interplay between grain size, grain interconnectivity, pore size and specific surface area. **a)** Particles loosely packed, with infinite small contact areas between each other. **b)** Effect of sintering which reduces both the pore size and the specific surface area while increasing the grain interconnectivity and, thus, the stability of the structure.

In mesoporous systems, gas diffusion is marked by the fact that the dimensions of the pores are roughly comparable to the free mean paths of the gas molecules [20]. In transition regimes, the diffusion coefficient, which measures diffusivity, is a crucial physical variable to consider [21]. As previously reported [22,23], the empirical Bosanquet formula can be used to predict gas diffusivity under transition regimes (D_{pore}):

$$D_{pore} = \frac{1}{D_b} + \frac{1}{D_K} \quad eq.1.17$$

where D_b is the gas molecular diffusivity and D_K is the Kundsen diffusivity. The microscopic expression of molecular diffusivity can be obtained by applying the Chapman-Enskog expansion solution to the Boltzmann transport equation [24], and it is directly proportional to T^3, $1/\sqrt{m}$, and $1/d_g^2$ (see **eq. 1.18**), where T, m and d_g are temperature, mass and molecular diameter, respectively. The Knudsen diffusion coefficient can be calculated using the kinetic theory of gases as in **eq. 1.19** where d is the local pore size [21].

$$D_b = \frac{3k_BT}{8pd_g^2}\sqrt{\frac{k_BT}{\pi m}} \quad eq.1.18$$

$$D_K = \frac{4d}{3}\sqrt{\frac{k_BT}{2\pi m}} \quad eq.1.19$$

Even though the pore size common inhomogeneity makes modelling gas diffusion inside the mesoporous film using **eqs. 1.18** and **1.19** difficult, some general considerations can be made. When considering the physical quantities d and T constant, diffusivity is significantly affected by the mass and diameter of the gas molecules. Lighter molecules diffuse faster and deeper into the sensing layer than heavier molecules. This would have a significant impact on the porous sensor's selectivity.

1.3.2 Solid/gas interfaces: physical and chemical adsorption

When a gas is brought into contact with a clean solid surface, there is an accumulation of gas at the interface. This phenomenon is known as adsorption and it refers to the binding of a gas molecule, i.e. adsorbate, onto a solid surface, i.e. adsorbent. Any solid is capable of adsorbing a certain amount of gas, the extent of which depends on temperature and pressure of the gas and on effective surface area of the adsorbent.

The adsorption of gas molecules can be classified in two major categories, i.e. physisorption and chemisorption. Physisorption is a non-specific weak adsorption, usually associated with Van der Waals interactions between the adsorbent and the adsorbate. On the contrary, chemisorption is a specific adsorption, which mostly requires an activation energy, and involves the formation of chemical bonds between the adsorbent and the adsorbate. It can be associative, if bonds in adsorbed molecules are changed in strength but not broken, or dissociative, if bonds in the adsorbed molecules are broken. The main characteristics of physisorption and chemisorption are summarized in **Table 1.1**.

Table 1.1 Characteristics of physisorption and chemisorption [16].

Properties	**Physisorption**	**Chemisorption**
Enthalpy of adsorption (ΔH)	$\Delta H_{phys} \leq 6 \ \ kcal/mol^{-1}$	$\Delta H_{chem} \geq 15 \ \ kcal/mol^{-1}$
Activation Energy (ΔE_a)	No appreciable ΔE_a (non-specific)	A ΔE_a is involved (specific)
Reversibility	Reversible, i.e. the adsorbate can be removed easily from the surface in an unchanged form	Irreversible, i.e. the adsorbate is removed with difficulty in a changed form
Number of adsorbed layers	Monomolecular layer formed at low pressure, followed by an additional layer as pressure increases (multilayer)	Restricted to formation of a monolayer
Rate of adsorption	Rapid at all temperatures	The rate increases rapidly with rise in temperature

The Lennard-Jones model shown in **Fig. 1.7 a** represents the energy of the system adsorbate/adsorbent as a function of their distance *d* and is a simple way to visualize some of the main properties described in **table 1.1**, e.g., the enthalpy of physical and chemical adsorption, ΔH_{phys} and ΔH_{chem}, respectively, and the activation energy of chemisorption, ΔE_a, obtained from the intersect between physisorption and chemisorption curves. As the molecule approaches the substrate (curve a in **Fig. 1.7 a**), it can polarize and induce an equivalent dipole in the surface, resulting in a van der Waals dipole/dipole interaction with an ΔH_{phys} binding energy. However, a further approach results in atom-substrate repulsion, which increases the energy of the system. As a result, the physiosorbed molecule is stably located at an energy minimum (r_p) at a substantial distance from the surface. Because there is no activation energy for this process, the rate of physisorption becomes temperature independent. On the contrary, desorption increases with temperature. Therefore, physisorption is predominant at low temperatures and almost non-existent at high temperatures [25].

A molecule, on the other hand, can dissociate into "atoms" in the presence of a large dissociation energy (ΔE_D) and as the atom approaches to the surface (curve b in **Fig. 1.7 a**) a strong

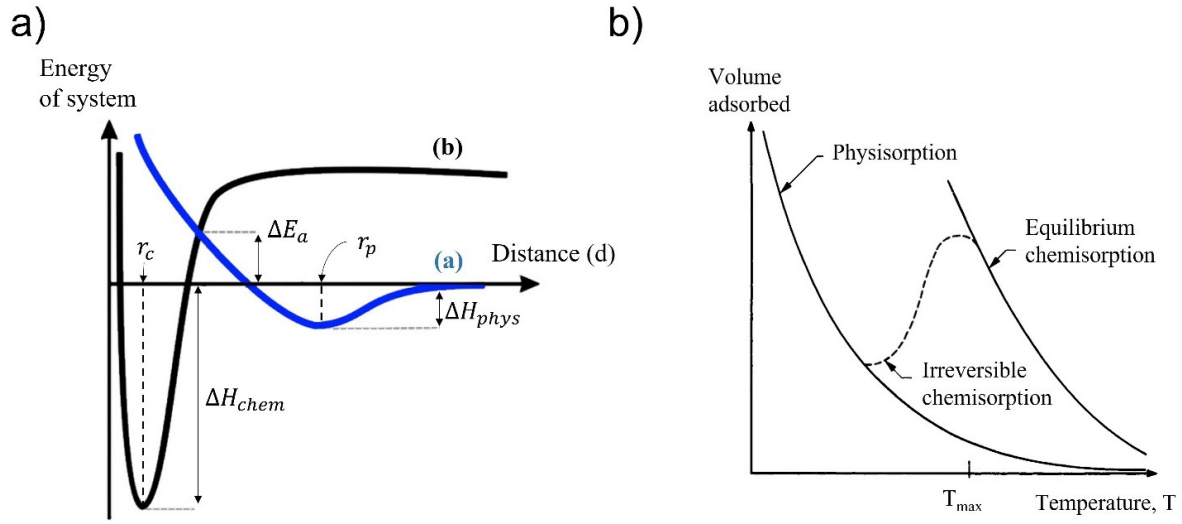

Fig. 1.7 a) Lennard-Jones Model of (a) physisorption and (b) chemisorption. The graph shows the energy of the system as a function of the distance, d, between the adsorbent and the adsorbate. **b)** Typical adsorption isobar curve, i.e. volume adsorbed as a function of temperature for a constant gas pressure. Figure is adapted from [16].

interaction, generally involving electron transfer, occurs to form a chemical bond with the adsorbate at a distance r_c. The enthalpy ΔH_{chem} is much larger than ΔH_{phys} and sometimes approaches the heat of compound formation [25]. However, direct chemisorption of molecules appears less likely due to the large energy (ΔE_D) required for dissociation into atoms. In practice, adsorption occurs through physisorption followed by chemisorption, for which a much lower energy of ΔE_a is demanded [16].

The rate of chemisorption from the molecular gas phase, in the case ΔE_a is thermally provided, is:

$$\frac{d\theta}{dt} = k_{ads}\exp\left(\frac{-\Delta E_a}{kT}\right) \quad eq.1.20$$

where θ is the fraction of available surface sites covered [16]. Desorption, on the other hand, is represented in Lennard-Jones model by the energy $\Delta E_a + \Delta H_{chem}$. Then, the net rate of adsorption is given by:

$$\frac{d\theta}{dt} = k_{ads}\exp\left(\frac{-\Delta E_a}{kT}\right) - k_{des}\theta exp\frac{-(\Delta E_a + \Delta H_{chem})}{kT} \quad eq.1.21$$

Setting $\frac{d\theta}{dt} = 0$ for the steady state, the equilibrium coverage θ is:

$$\theta = \frac{k_{ads}}{k_{des}} exp\left(\frac{\Delta H_{chem}}{kT}\right) \quad eq.1.22.$$

Because both the adsorption and desorption processes require energies, they occur at an elevated temperature compared with physisorption.

The isobar curve in **Fig. 1.7 b** depicts the temperature dependence of the coverage for physiosorbed and chemisorbed species on a solid in a schematic form [16]. At low temperature, adsorption follows an unactivated physisorption process. Then, the coverage of chemisorbed species appears to increase with increasing temperature up to a maximum adsorption at

temperature T_{max}. Below this value the theoretical desorption rate is substantially lower than the adsorption rate [25]. Above T_{max}, the rate of desorption becomes appreciable, and the surface coverage decreases with increasing temperature [16].
A form of chemisorption, ionosorption, is a key player in reactions on metal-oxide surfaces [25]. Ionosorption is the formation of an adsorbed ion by transfer of electrons between defects deep in the solid and the adsorbate, namely, the adsorbate acts as a surface state. Then, the ion is held to the surface by electrostatic attraction [16]. The ionosorption of oxygen is of particular importance in gas sensors, as will be explained in Section 1.3.3.
In addition to adsorption, the gas can also react and penetrate through the surface into the core of the solid. This phenomenon is called absorption and causes change in stoichiometry of the solid [16].

1.3.3 Influence of adsorbed gas on the conductance of nanostructured porous films

Chemiresistive gas sensors are usually composed of nanostructured porous films of metal-oxide semiconductors. In such films, the conductance is the result of electrons transport through the network of interconnected nanostructures surrounded by the atmosphere. In order to cross from one nanostructure to another, free carriers must overcome the Schottky barrier, qV_s, built as a result of surface charge formation, which very strongly depends on adsorbed gases. Thus, the conductance is limited by and proportional to the density of electrons n_s with energy qV_s, where n_s is given by **eq. 1.16** [16]. The phenomenological **eq. 1.23** is normally used to describe the conductance in polycrystalline metal-oxide semiconductors, in which G_0 is the flat band conductance.

$$G = G_0 \exp\left(-\frac{qV_s}{kT}\right) \quad eq.1.23$$

Fig. 1.8 a shows a schematic representation of few grains in contact and in presence of oxygen, which is the main reactive component of ambient air. As introduced in Section 1.3.2, when a sensor is exposed to air at a working temperature between 100 and 500 °C usually atmospheric oxygens ionosorb as molecular (O_2^-) and atomic (O^-, O^{2-}) forms by capturing electrons at a surface state of the semiconductor [26], i.e. creating surface acceptor states. A simple model for the adsorption of oxygen can be described using the following reaction steps, assuming chemisorption equilibrium (no reducing agent present) and neglecting the role of surface sites and oxygen vacancies [16,27,28].

$$O_{2,gas} \leftrightarrows O_{2,ads} \quad \text{eq. 1.24}$$
$$O_{2,ads} + e^- \leftrightarrows O_{2,ads}^- \quad \text{eq. 1.25}$$
$$O_{2,ads}^- + e^- \leftrightarrows O_{2,ads}^{2-} \quad \text{eq. 1.26}$$
$$O_{2,ads}^{2-} \leftrightarrows 2O_{ads}^- \quad \text{eq. 1.27}$$
$$O_{ads}^- + e^- \leftrightarrows O_{ads}^{2-} \quad \text{eq. 1.28}$$

Then, the presence of negative species on the surface of the metal oxide builds up a depletion layer, whose positive charge exactly compensates for the charge captured at the surface, leading to electroneutrality in the Schottky approximation [29]. The formation of this depletion layer causes the energy bands at the surface to bend upwards with the respect of the Fermi level, as

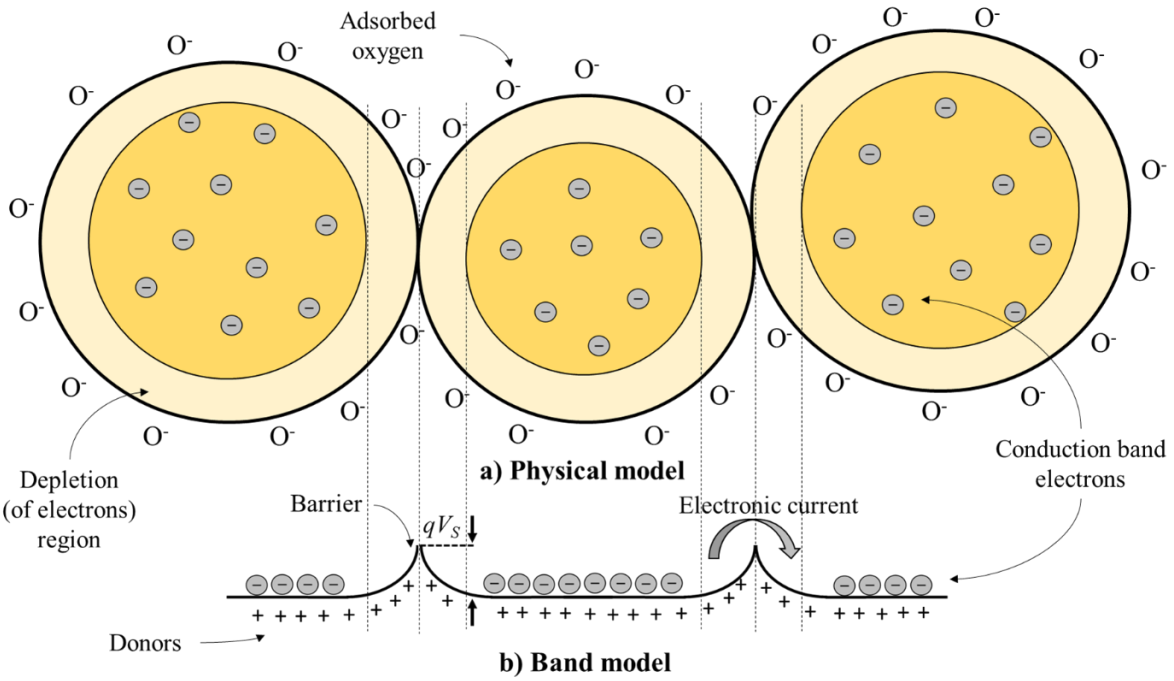

Fig. 1.8 Schematic of three semiconductor grains in oxygen atmosphere. In **a)** the physical model shows the space-charge region around the surface of each grain, being depleted by atmospheric oxygen ionosorption. The band model of the same group of grains is represented in **b)** to show how the intergranular contact resistance appears.

represented in the band model of the same group of grains in **Fig. 1.8 b**. The increase of qV_s decreases the conductance along the film.

Commonly, the changes in conductance (or resistance) of the gas-sensing material are induced not only by oxygens adsorption (**Fig. 1.9 a**), but also by the other surrounding gases, which can show reducing or oxidizing properties. **Fig. 1.9 b** schematically represents the possible sites on

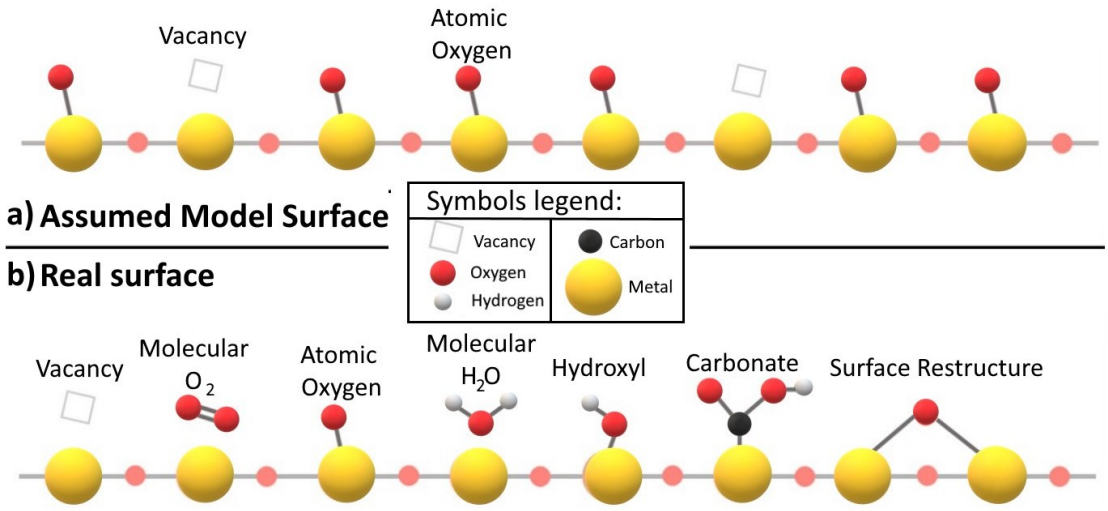

Fig. 1.9 Illustration of a schematic simplified metal-oxide surface in air at high operating temperature before interaction with the analyte. In **a)**, the SMOX surface is represented as most studies assume it to be, interacting with only oxygens. In **b)**, an SMOX surface under real-world operation conditions, i.e. in presence of oxygen, humidity, CO_2, and surface reconstruction. Figure reprinted from [30].

real operating conditions, i.e., in presence of oxygen, humidity, CO_2, and surface reconstruction [30].

In particular, water molecules are commonly highly reactive and might directly interact with the SMOX surface changing the active sites while affecting the electrical properties of the film and could hide the presence of gaseous analytes in the environment by limiting their adsorption and reaction. The effect of humidity on the semiconducting film is thus critical in determining the applicability of the sensors for practical uses. H_2O adsorption includes physisorption (**eq. 1.29**) and associative (**eq. 1.30**) or dissociative (**eq. 1.26**) chemisorption [16,31]. Physisorption prevails at low temperatures, often forming multilayers. Associative adsorption of water is due to H-bond formation at intermediate temperatures and may cover active adsorption sites (**eq. 1.30** and **eq. 1.31**). At high temperatures water dissociates in H^+ protons and OH^- hydroxyl groups. OH^- hydroxyl groups passivate the metal active adsorption sites $(OH)_S$, while H^+ protons react with the chemisorbed O^- species forming neutral OH groups and affecting the conductance $(OH)_0$ [32].

$$H_2O_{gas} \leftrightarrows H_2O_{phys} \quad \text{eq. 1.29}$$

$$H_2O_{gas} + O_0 \leftrightarrows HO \cdots H \cdots O_0 \quad \text{eq. 1.30}$$

$$H_2O_{gas} + (Sn-OH)_{Sn} \leftrightarrows H_2O \cdots HO \cdots Sn_{Sn} \quad \text{eq. 1.31}$$

$$H_2O_{gas} + O_0 + S \leftrightarrows (OH)_0 + (OH)_S \quad \text{eq. 1.32}$$

Barsan et. al. summarized water adsorption mechanism and classified different hydroxyl groups that may be located on the surface of SMOXs [32–34]. **Fig. 1.10** differentiated between interacting and isolated hydroxyl groups, with the latter further subdivided into terminal (onefold coordinated) and rooted (two- or threefold coordinated) [32].

In addition to the aforementioned reactions, the SMOX film conductance depends on various processes, which can take place both at the surface and in the bulk of the material [35], as represented in **Fig. 1.11**. The main effect of such processes, based on general conception, are (1) the change of the concentration of free charge carriers, (2) the change of the Schottky barrier height at the inter-crystallite boundary and (3) the change of bulk electrophysical parameters of

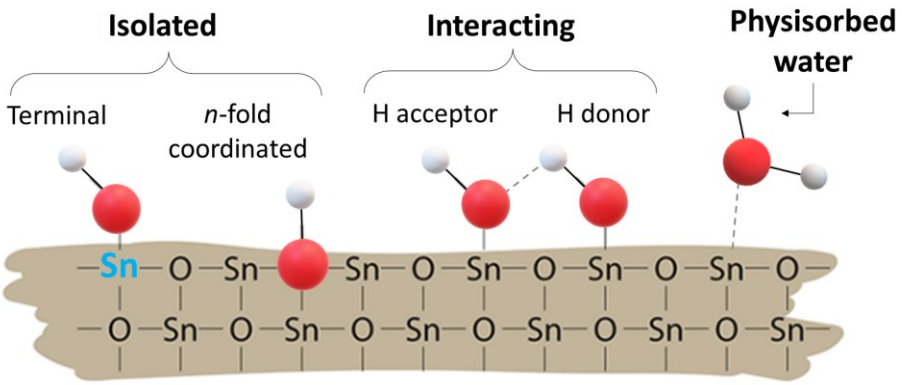

Fig. 1.10 Two-dimensional representation of the SnO_2 surface with isolated and interacting hydroxyl groups and physisorbed water. Figure reprinted from [32].

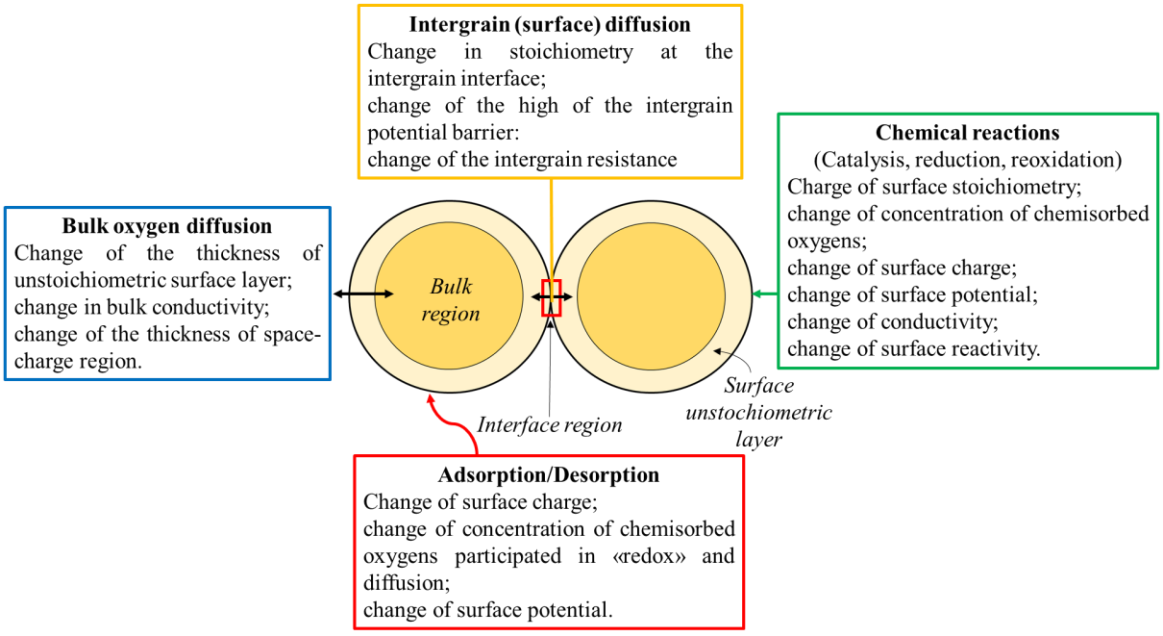

Fig. 1.11 Diagram illustrating the main bulk and surface processes taking place on metal oxides when exposed to gases and their effect on the materials properties. Figure adapted from [36].

metal oxide, such as the concentration of ionized centers and the mobility of bulk charge carriers [36].

1.3.4 Structural parameters of metal oxides controlling gas-sensing properties

Considering the complexity of bulk and surface processes which can take place as a consequence of solid/gas interface formation (**Fig. 1.11**), it becomes clear that the gas sensing mechanism is influenced by a great number of various structural parameters. **Fig. 1.12** illustrates (**a**) the main parameters controlling (**b**) the gas sensing properties of a SMOX-based device.

Even though SMOXs are catalytically active, different strategies are often pursued to improve their selectivity and sensitivity, for example surface modification by noble metals [37–39]. When present as a separate phase (inhomogeneous dispersion), noble metals influence the reception and/or transduction of the sensing material by chemical or electrical sensitisation mechanism. The first is related to spill-over of gases [40], while the second is based on the alignment of the Fermi levels of the SMOX and the noble metal phase [37–39].

Moreover, chemical composition of a SMOX can be modified by incorporation of atoms other than those composing the host material. Such atoms, usually transition metals, can either form a solid solution by substitution of the host atoms from the lattice or can be interstitially present in the host lattice [41]. Then, incorporating foreign atoms influences the properties of SMOXs by changing the strain in the lattice and, when ionized, by affecting the electro neutrality condition.

Furthermore, the sensing properties of the active films can be modulated by shape and size of the nanomaterials, which have an impact on the number of surface reactive sites, on the surface reaction rate and on gas diffusion [42].

Lastly, crystal structure plays a critical role in determining the electronic band structure both in bulk and at the surface of a SMOX material, therefore influencing its physical and chemical properties, such as band gap, electron mobility and surface reactivity. In particular, every crystal form has its own combination of crystallographic planes, framing the nanocrystal. Crystal planes exposed on the surface determine surface composition and surface structure, strongly

affecting the adsorption/desorption energies of interacting gas molecules, concentration of adsorption surface states, energetic position of surface Fermi level, activation energy of native point defects, and so on. This implies that the chemisorption characteristics change noticeably from the crystal surface orientation to another [35].
As will be described in section 2.1, the engineering of morphology and chemical composition have been exploited to obtain sensitive nanostructured materials for thick film solid-state devices with improved gas sensing properties with the respect to SMOX in the literature. Firstly, tungsten trioxide (WO_3) morphology has been optimized for ethanol detection. Secondly, chemical composition and grain size of a solid solution of tin, titanium and niobium oxides have been tuned for hydrogen and ethanol sensing.

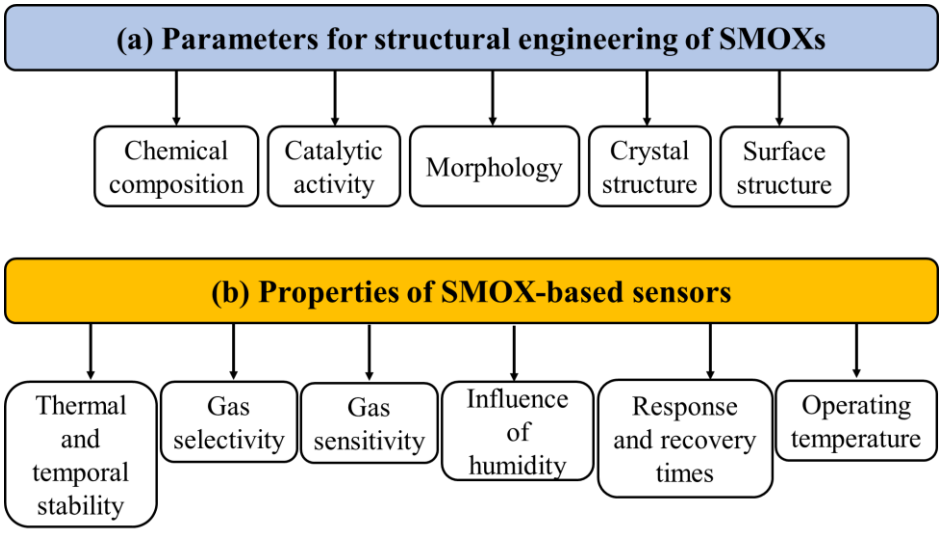

Fig. 1.12 Diagram illustrating the materials parameters (a) controlling the properties (b) of SMOX-based sensors. Scheme adapted from [202].

1.3.5 The thermal activation of metal-oxide sensors

Aside from the SMOX material properties, the temperature of operation has a direct impact on the sensing film, i.e. influencing its conductance, promoting surface reactions with the gases, and affecting the surface barrier V_s.
At low temperature, such as room temperature (RT = 25 °C), the conductivity of the semiconducting films is commonly very low and derives from charge carriers in shallow levels (defects states with the energy only few k_BT away from the band edges) which are thermally promoted into the bands and participate in transport phenomena [43]. At higher temperatures, charge carriers from deeper levels inside the gap may contribute to the conductance of the film, which consequently increases.
The working temperature influences not only the conductance in the bulk of the nanostructures, but also the surface states of the sensitive material and the reactions during the detection process. As a result, the response of chemoresistive gas sensors to an analyte typically exhibits a "volcano" shape (increase-peak-decrease) relationship with operating temperature [44].
The increase of the response with the rise in operating temperature is mainly the result of two effects. Firstly, it is proved by IR (infrared analysis), TPD (temperature programmed desorption), and EPR (electron paramagnetic resonance) that at temperature between 100 and 500 °C, i.e. common chemoresistive sensor working temperatures, the interaction with

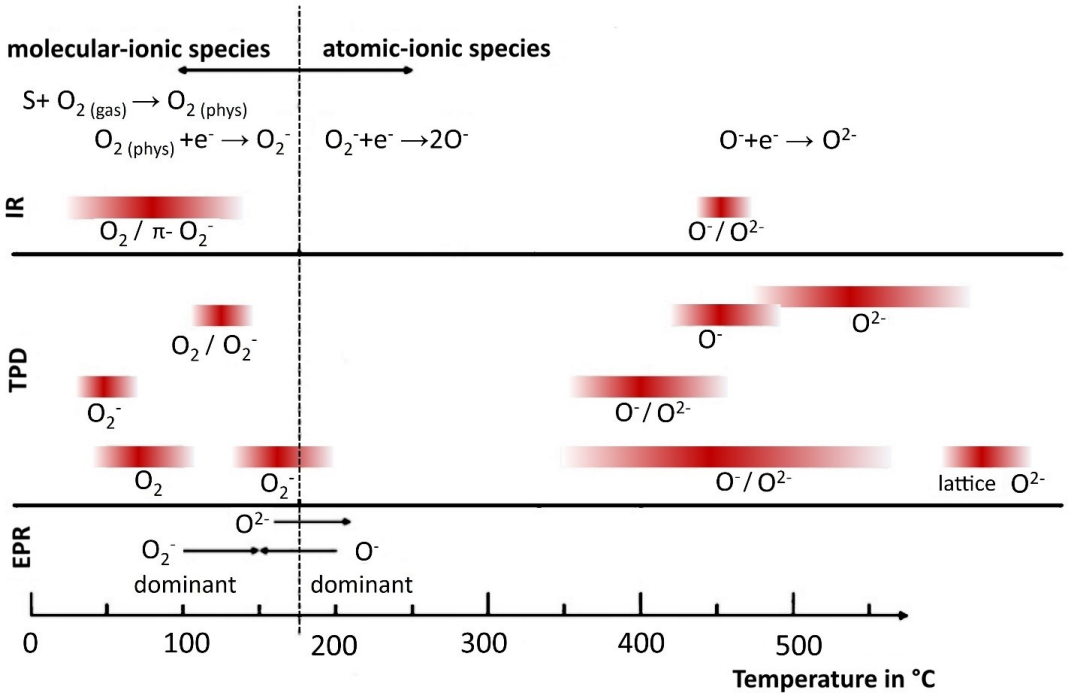

Fig. 1.13 A review of the literature on oxygen species detected at various temperatures on SnO_2 surfaces using IR (infrared analysis), TPD (temperature programmed desorption), and EPR (electron paramagnetic resonance). Image adapted from [17].

atmospheric oxygen leads to its ionosorption in molecular (O_2^-) and atomic (O^-, O^{2-}) forms, as described in **Fig. 1.13** [17]. These species became active sites for surface transfer reactions with the ambient gases. They have different reactivity, O^- being the most reactive sites for reducing gases [16]. Secondly, chemical reactions, e.g. chemisorption or ionosorption, between the surface of the adsorbent and the adsorbate, requires an activation energy to be supplied. At low operating temperatures gaseous molecules do not have enough thermal energy to react with the adsorbed oxygen species and the reaction rate is essentially low. While, as temperature increases, the thermal energy obtained is high enough to overcome the activation energy barrier to promote adsorbate reaction with the active sites on the surface of the SMOX.

To summarize, as the temperature rises, the ionosorbed oxygens trap more electrons and become more reactive, while the gases have enough energy to react with the active sites. The effect is that both the concentration of charge carriers in the bulk of the material and the Schottky barrier V_s change more significantly after the target gas/solid reaction.

Above the optimal operating temperature, the rate of gas desorption becomes appreciable (see section 1.2.2) and a decrease in the amount of adsorbed gas molecules at surface lowers the gas response [44,45].

In addition to maximizing the sensitivity of the material, the operating temperature is also important for tuning the selectivity. According to Ponzoni et al. [46], oxides are more sensitive to reducing gases at higher temperatures (200-250 °C), because active oxygen species (O^-, O^{2-}) are available on the sensor surface beyond this temperature. On the other hand, lower operating temperatures are generally recommended for oxidizing gases. Because there are fewer surface adsorbed oxygen species available at lower temperatures, the sensor surface is more susceptible to oxidation.

In conclusion, a sensor exhibits maximum sensitivity and selectivity at a specific temperature depending on the gas species to be detected because of (1) temperature-dependent oxygen

adsorption rate and (2) temperature-dependent catalytic activity of the sensing element vs. the analyte.

1.4 APPLICATIONS FOR CHEMORESISTIVE GAS SENSORS

Gas sensors based on the chemoresistive effect that occurs in nanostructured semiconductors have been extensively studied over the years as the simplicity of their transducer/receptor configuration makes them easy to fabricate, miniaturize and less expensive than other types of sensors, such as electrochemical and infrared sensors. According to the new gas sensors market report [47], this business is expected to be valued at USD 2.1 billion by 2027, with a compound annual growth rate of about 8.9 % between 2022 and 2027. The market's expansion is attributed to the increasing adoption of gas sensors in automotive and transportation applications, consumer electronics industry, building automation, wastewater treatment, metal & chemical industry, mining industry, medical industry, and, with the rising levels of air pollution, the need for air quality monitoring in smart cities [47]. Nowadays, solid-state/metal-oxide semiconductors are used to detect oxygen, carbon monoxide, carbon dioxide, ammonia, chlorine, hydrogen sulphide, nitrogen oxide, volatile organic compounds, sulphur dioxide, methane, hydrocarbons and hydrogen. Nevertheless, the market continues to seek sensors with greater control over material properties for improved gas response and durability, as well as increasing levels of detection control for the different environmental conditions expected in the aforementioned applications.
The third and fourth chapters will focus on the development and characterization of chemoresistive sensors for the detection of ethanol and hydrogen. Therefore, the potential applications of these sensors will be discussed further below.

1.4.1 Applications for ethanol sensors

Ethanol sensors find applications in various areas, such as detection of alcohol abuse and monitoring of fermentation and other processes in chemical industries [48].
The detection of alcohol concentrations in the brain is critical for road and workplace safety. Blood alcohol concentration (BAC), defined as the percentage of alcohol in the blood, is conveniently used to assess the alcohol level in brain tissue as a measure of impairment from alcohol poisoning. At 0.05% BAC, most people exhibit measurable mental impairment. Above this limit, the ability to drive a car deteriorates progressively as blood alcohol levels rise. The average person has a BAC of 0.4% when they are unconscious. Basic body functions such as breathing and heartbeat can be depressed above 0.5% BAC, leading to death [25]. The alcohol concentration in the deep lung breath is one of the most convenient and non-invasive methods of determining BAC. Approximately 0.01% BAC corresponds to 16 ppm alcohol in the breath stream (BrAC is frequently used to indicate that the measurement is a breath measurement), and BAC values thereafter increase proportionally to the alcohol concentration in the breath [25,49].
Moreover, ethanol is a clear, colorless liquid that is used in the processing of food and alcoholic beverages, as well as the manufacture of fuel and personal and household products. When it makes contact with air it can accumulate as vapour if not properly ventilated. Ethanol gas is not only highly flammable, but it also poses serious health risks to people working in commercial or industrial settings. Gas detection sensors play an important role in detecting ethanol levels

and ensuring they are within safe and acceptable limits. Any ethanol-producing facility should implement gas monitoring protocols for safety and compliance. Among the applications that require ethanol detection sensors are breweries, distilleries, and wineries [50], manufacturing of chemicals, cosmetics, pharmaceutical, food and beverage manufacturing and refineries.

1.4.2 Applications for hydrogen sensors

Real-time hydrogen detection is necessary in a wide range of industrial fields. Among these, the automotive industry is one of the most promising hydrogen markets. Automobiles are primarily powered by gasoline and diesel, but these fossil fuels are associated with major issues such as air pollution and global warming. Because it emits no greenhouse gases, there has been an increase in research interest in the use of hydrogen as a fuel in automotive applications over the last decade [51]. Furthermore, hydrogen is widely used in a variety of industrial processes, including the production of methanol and ammonia, as well as petroleum refining. Due to its widespread use, the global hydrogen generation market was valued at USD 117.49 billion in 2019, and it is expected to grow steadily in the future [52]. However, it is critical to monitor hydrogen leaks in its production, storage, and transportation. In fact, hydrogen is a dangerous gas, forming explosive mixtures with air in the 4-75% volume range [53,54].
Secondly, the rapid spread of portable electronic devices, electric vehicles, and smart grids has resulted in a large demand for high energy density energy storage systems with long-term electrochemical performance. Lithium-ion batteries, which have high voltage, lightweight, high energy density, and low environmental pollution, have become the main research direction for new energy storage technologies [55]. However, because of the high energy density as well as the flammable and explosive properties of both the liquid organic electrolyte and the polymer-based separator, lithium-ion batteries have sparked widespread concern since their introduction. Internal/external lithium battery defects and various abuse circumstances will result in irreversible redox reactions, a large amount of heat by-products, and the release of toxic and flammable gases [55], as summarized in **Fig. 1.14** [56].

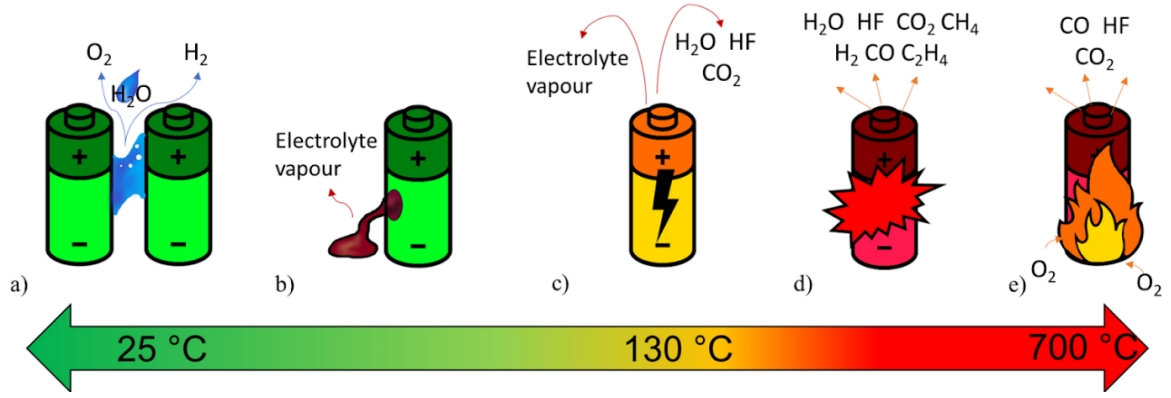

Fig. 1.14 Gas emissions from battery failure cases. **a)** Unwanted electrolysis, **b)** vaporizing electrolyte of damaged cells, **c)** the first venting of a failing cell, **d)** the thermal runway and **e)** battery fire. Step **a)** and **d)** may include the emission of H_2 [55,56].

Chemoresistive sensors have been widely used in the field of thermal runaway gas detection and battery early warning because, when compared to other types of gas sensors, they feature more advantages such as high sensitivity, high stability, low cost, ease of integration. H_2 sensors

may be integrated in sensor arrays to monitor the gas release during unwanted electrolysis and thermal runway in battery packs (**Fig. 1.12 a** and **d**).
Additionally, chemoresistive sensors found applications in breath analysis for identification of various diseases. Indeed, a number of recent studies have found a strong correlation between exhaled breath components and specific diseases, suggesting that exhaled breath sensors have a high potential for clinical diagnostic applications [57]. Hydrogen breath tests, for example, are widely used to investigate the pathophysiology of functional gastrointestinal (GI) disorders such as small intestinal bacterial overgrowth (SIBO) and carbohydrate malabsorption, which have been proposed to be important for GI disease symptoms [57–59]. Indeed, bacteria in the bowel produce hydrogen gas during carbohydrate fermentation, which occurs when dietary carbohydrates, e.g., glucose, lactose, fructose, are not absorbed in the small intestine and remain as undigested material as it travels along the digestive tract into the large intestine [58]. Before the test, a predetermined amount of carbohydrate is usually administered. The increase in hydrogen concentration above baseline from 10 to 20 ppm is then used to determine a positive test [60].

Chapter 2- MATERIALS AND EXPERIMENTAL METHODS

2.1 STATE OF THE ART

2.1.1 WO_3 and morphology

Tungsten(VI) oxide, also known as tungsten trioxide (WO_3), is an wide band gap n-type semiconductor with excellent conductivity and high electron hall mobility. The interest in WO_3 has developed since its sensing properties are highly dependent on the synthesis technique by which crystal structure and morphology can be tuned [61].

The variation of crystal structure parameters is a commonly used strategy for controlling the sensing properties of WO_3-based sensors. Indeed, WO_3 exhibits multiple polymorphs, despite its simple stoichiometry, because the ideal cubic crystal structure can undergo structural distortions and phase transitions [62]. Temperature-induced WO_3 phase changes from monoclinic (ε-WO_3), triclinic (δ-WO_3), monoclinic (γ-WO_3), orthorhombic (β-WO_3), to tetragonal (α-WO_3) result from WO_3 octahedral tilting and W atom displacement from the center of the octahedral sites (Magneli phases) [62]. Furthermore, hexagonal (h-WO_3) can be obtained by slow dehydration of tungstite [62,63]. Monoclinic, triclinic, and hexagonal are the most stable phases at *RT*, but WO_3 usually transforms into orthorhombic from 330 °C to 740 °C and tetragonal at temperatures higher than 740 °C.

In addition to the variety of crystal structures, capping agents and structure-directing agents during the synthesis [64,65] can be used to engineer the exposed crystal facets, which strongly influence the adsorption behavior of oxygen and target gaseous molecules on the surface.

Besides crystal structure engineering, the relatively wide variety of precursors, e.g. tungsten chloride, tungstic acid, ammonium tungstate, sodium tungstate dehydrate, silicon tungstic acid and metal tungstate, allows for the use of different syntheses to regulate WO_3 morphology [66]. The objective of morphological modification is to increase surface area by enhancing porosity and volume ratio, which promotes catalytic reaction centers. The nanomaterials are classified as 0D (zero dimensional), 1D (one dimensional), 2D (two dimensional) or 3D (three dimensional) according to the number of dimensions (D) which are outside the nanoscale (<100 nm) range.

Gas sensors based on 0D WO_3, such as tiny nanoparticles and quantum dots (QDs), generally exhibit poor gas sensing performances because of their insufficient specific surface area and very small porous structures, which do not favor gas absorption and diffusion [66].

1D (e.g. nanofibers, nanotubes, nanorods, and nanowires) and 2D (e.g. nanoplates, nanolamellas, nanodiscs and nanoflakes) WO_3 are more promising nanomaterials than 0D WO_3 because they display a higher surface-to-volume ratio (SA:V) which provide a large specific surface area and numerous active sites for gas adsorption. Commonly, they are synthetized through solvothermal or hydrothermal routes by modulation of synthetic conditions, such as type of solvent, reaction temperature and time, and with the assistance of additives or templates. The synthesis can be microwave or magnetic field assisted [66]. Other methods include electrospinning, Physical Vapor Deposition (PVD), Atomic Layer Deposition (ALD), Pulsed Laser Deposition (PLD), Chemical Vapor Deposition (CVD) and sputtering [66].

Assembled 1D or 2D nanostructures results in 3D WO_3 which typically appears as microspheres, microflowers, urchin-like structures, mesoporous structures, and other irregular structures. These WO_3 are reported to achieve high gas sensing properties for various gas detection too, due to the large surface area and rich porosity [66]. The synthesis methods typically include microwave assisted hydrothermal method [67] and sonochemical route [68,69] and the use of structure-directing agents such as hard templates, e.g. SBA-15 silica [70,71] and cubic KIT-6 silica [72,73], or soft templates, e.g. amphiphilic poly(ethylene oxide)-b polystyrene (PEO-b-PS) [74,75]. The simplest routes without any templates, catalysts, or substrates usually requires long time procedures, e.g., 16-24h, for hydrothermal or solvothermal synthesis at high temperatures, i.e., in the range of 100-180°C [76–79]. Therefore, despite the excellent detection performances, the expensive and time-consuming synthesis processes may discourage widespread commercial use of 3D WO_3.

In conclusion, 1D and 2D materials are the most attractive nanostructures for the development of WO_3-based devices with tailored gas sensing capabilities because they can combine a high surface-to-volume ratio with low cost and high efficiency production via process parameter optimization. **Table 2.1** summarizes the gas sensing performances of some WO_3-based devices with 1D and 2D morphologies.

Table 2.1 Synthesis methods for 1D and 2D WO_3-based sensors for the detection of different target gases. The response is given at their optimal operating temperature.

Dimension	Microstructures	Synthesis method	Target gas	Concentration (ppm)	T (°C)	Response[a]	REF.
1D	Nanofibers	Hydrothermal	ethanol	100	350	62	[203]
		Electrospinning	NH_3	100	300	1.7	[204]
		Electrospinning	NH_3	100	200	5.5	[205]
	Nanotubes	Electrospinning	H_2S	1	450	203.5	[206]
		Electrospinning	NO	5	350	100.3	[207]
		Solvothermal	ethanol	300	340	16.9	[138]
	Nanorods	Hydrothermal	butanol	1000	200	232	[208]
		Thermal oxidation	NO_2	10	225	2.02	[209]
	Nanowires	Hydrothermal	NO	500	300	37	[210]
		Hydrothermal	ethanol	100	300	18	[211]
2D	Nanoplates	Hydrothermal	NO_2	100	100	132	[212]
	Nanosheets	Solvothermal	NO_2	1	100	62.1	[213]
	Nanolamella	Hydrothermal	ethanol	10	200	11.3	[44]
	Nanoflakes	Hydrothermal	NH_3	1	200	27	[211]

[a] Gas response $R = \frac{R_{air}}{R_{gas}}$.

Despite the high response levels, 1D nanostructures present some disadvantages, such as their thermal and chemical instability as a result of their low melting point and high resistivity [80]. In addition, their sensor operating temperatures are on average higher than those of 2D-based sensors for the same target analytes.

The studies in [44] showed that nanolamellas WO_3-based film synthetized through hydrothermal method highlighted promising characteristics for ethanol detection at a low operating temperature. Although measurements were performed with different concentrations

of ethanol and some interferents, the influence of humidity on the response as well as the response to a wider spectrum of gases to which WO_3 is usually sensitive was not considered. Moreover, in this work the sensor characteristics were measured with a commercial NMDOG Multifunctional Precision Sensor Analysis Tester by using a static process under laboratory conditions, i.e. fresh air at 35% relative humidity and 25 °C. This system did not allow for total control of the atmosphere content in the chamber, which could be instead acquired using synthetic air, and it also did not enable investigations in dry conditions or variations in humidity content.

This motivated the search for a 2D WO_3-based film for ethanol detection which could combine high sensitivity and selectivity with good repeatability, stability, and low operating temperature. WO_3 nanoflakes powders (WO_3 NF) have been synthetized through a simple and time effective solvothermal method. Then, WO_3 NF-based films were electrically characterized to investigate their potential as ethanol sensors in dry and wet conditions. Finally, in section 3. 4 the ethanol-sensing performance of the WO_3 NF film in this work was compared to that of other WO_3 sensors with different morphologies, as well as several commonly used metal oxide sensors in the literature, **Table 3.8**.

2.1.2 Solid solutions based on SnO_2

Approximately 90% of the SMOXs used as sensing films in chemoresistive devices are semiconductors such as SnO_2, ZnO, TiO_2, WO_3, In_2O_3, and CuO [8]. A scarcity of reactive metal oxides may limit the sensing performance described by the 3S rule (selectivity, sensitivity, and stability). A solid solution of two independently sensitive metal oxides would allow the sensing qualities of the solution to be varied with continuity, with the relative percentage of the metal as a free parameter to be tuned [29]. The goal is to enhance the properties of single oxides, e.g. catalytic and physical properties, while perhaps mitigating their limitations.

As a particle example, a solid solution of Sn and Ti oxide was reported to have lower cross-sensitivity to humidity during ethanol detection than pure SnO_2 [81]. This solid solution is an intriguing case study since Ti and Sn oxides are completely miscible, resulting in a substitutional solid solution $(Sn,Ti)_xO_2$ at any Sn/Ti ratio [82–84]. This material would take advantage of SnO_2 high sensitivity to most analytes and TiO_2 low cross-sensitivity to humidity [81,85]. Although promising, the $(Sn,Ti)_xO_2$ solid solution has some limitations, including increased film resistance with increasing Ti concentration, grain coalescence at temperatures required for solid solution formation, and anatase-to-rutile phase transition [81]. Previous investigations have shown that doping with transition metals can inhibit particle growth and improve thermal stability. In [86] Ferroni et al. investigated the effect of Nb^{5+} incorporation within a TiO_2 lattice, proving that it can inhibit grain growth and anatase-to-rutile transition. The average grain size

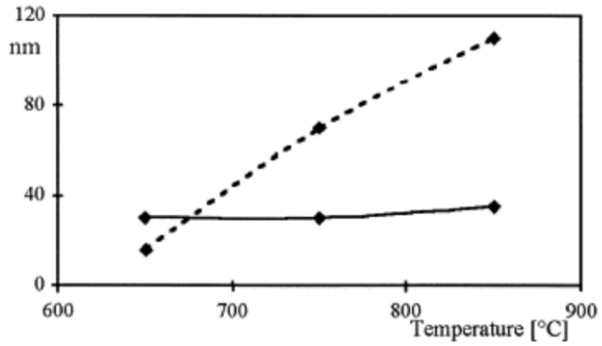

Fig. 2.1 Grain size of undoped (dashed line) and Nb-doped (solid line) TiO_2 films as a function of firing temperature (from TEM measurement). Figure reprinted from [86].

of the powders as a function of firing temperature shown in **Fig. 2.1** highlighted that the undoped TiO_2 powder exhibited large grain coarsening while Nb–TiO_2 grains size was maintained in the range 650-850 °C, indicating that the driving force for grain growth was reduced by Nb addition [86]. According to [87], the effects of the presence of a new compound in a nanograined structure on the rate of grain growth and density of rutile nucleation sites can be summarized via two basic mechanisms: (i) segregation at the grain boundary of a phase reduces the grain's surface energy or (ii) occupation of bulk lattice sites hinder the ionic mobility.

In addition to the beneficial effect on the SMOX thermal stability, foreign atoms, when ionized, affect the electro neutrality condition. Indeed, to maintain bulk charge neutrality, the charge at the aliovalent cation site relative to the perfect lattice must be compensated by a lattice defect of the opposite charge [88]. Dopant cations are classified as donor centers if they have a greater charge than that of the cation they replace, otherwise they are defined as acceptor centers [88]. In the first case, the lattice defect that compensates for the excess positive charge of the donor center can be either cation vacancy or oxygen interstitial. In the second case, the lattice defect that compensates for excess negative charge of the acceptor center can be either oxygen vacancy or cation interstitial [88]. The formation of new reactive sites on the surface of the SMOX may affect its sensitivity and selectivity by changing the activation energy and providing alternative reaction pathways.

The influence of Nb addition in the solid solution of Sn and Ti was investigated with regard to the morphological, structural and electrical properties. Nanograined powders with Nb contents of 1.5, 3.5 and 5% were produced using a sol-gel process, while maintaining the Sn/Ti ratio constant at the ideal value for sensing performance of the solid solution without Nb, i.e., Sn/Ti = 70:30 [89]. The effect of calcination temperature was also evaluated by heating the powders at 650 and 850 °C. The formation of a solid solution was revealed by the linear relationship between lattice parameter and dopant concentration because the presence of substitutional or interstitial foreign atoms influences the strain in the host lattice. The purpose of this research was to take advantage of $(Sn,Ti)_xO_2$ beneficial qualities, while mitigating its shortcomings, namely grain coalescence, structural thermal instability, and high resistance of the nanostructured film, through Nb addition.

2.2 CHEMICALS AND SYNTHESIS OF THE SENSING MATERIALS

2.2.1 WO_3 nanoflakes powder

The preparation method for the synthesis of nanocrystalline WO_3 powder was inspired by Grimes [65] and described in [90]. In a typical synthesis procedure, a 0.25M solution of tungstic acid (H_2WO_4, purity ≥99.5 %, from Alfa Aesar) was prepared by dissolving 1.25 g of the W precursor in 10 mL of millipore water and 10 mL of 35 wt % hydrogen peroxide (H_2O_2, from Acros Organics) while heating and stirring at 95 °C in a hot water bath. Then, 18 mL of such solution, 1.2 g of oxalic acid dihydrate (purity ≥99.5 % from Alfa Aesar) and 3 mL of 6M hydrochloric acid (HCl ≥37 %, from Supelco Merck ACS grade) were mixed under stirring to a solution of 60 mL of acetonitrile (from VWR Chemicals) and 15 mL of Milli-Q water. This mixture was transferred into a 1000 mL Teflon-lined stainless-steel autoclave and heated at 180

°C for 2 h in a Binder heating chamber with forced convection. After cooling to RT, the resulting yellowish green powder was collected and washed several times with acetonitrile and water prior to drying in air at 110 °C for 4 h and calcined at 500 °C for 2 h.
As suggested by Grimes, oxalic acid, and hydrochloric acid in the precursor solution play important roles in determining the morphology of WO_3. Indeed, surfactants and capping agents can control the nanocrystal shape by changing the free energies of the various crystallographic surfaces, thus altering their growth rates [91]. In many papers, Cl^- appears to be a growth-directing ion in forming 1D nanowires [65,91]. On the other hand, oxalic acid was found to be responsible for the evolution of WO_3 from nanowires to nanoflakes, probably due to its chelating properties [65,91,92].

2.2.2 SnO_2, $(Sn,Ti)_xO_2$, $(Sn,Ti,Nb)_xO_2$ nanoparticles powders

SnO_2, $(Sn,Ti)_xO_2$ and $(Sn,Ti,Nb)_xO_2$ powders were prepared according to the procedures described in [12,29,93].
In a typical synthesis procedure, required stoichiometric proportions of Sn(II)ethylhexanoate, Ti(IV)butoxide, and $NbCl_5$ were dissolved in a hydroalcoholic solution as Sn(II), Ti(IV), and Nb(V) precursor. The total cation concentration was kept at $[M^{n+}]$ tot = 0.1 M for each synthesis batch. The molar ratio between Sn, Ti and Nb used for the synthesis are listed in **Table 2.2**. Nb concentration were varied to 1.5, 3.5 and 5 %, while Sn-Ti ratio kept constant to 70:30 mol/mol. Firstly, the precursors were dissolved in 70 ml of 2-propanol. Then, 1 mL of 0.1 M HNO_3 solution was dropped to hydrolyze the metal-organic molecules, and 30 mL of mQ water was added to achieve a colloid. The entire process was carried out by maintaining the solution under gentle stirring. The colloidal solution was kept in the ice bath for 3 h and left to rest at RT overnight. The colloid was separated from the solution by vacuum filtration and washed several times with 2-propanol and water. The resultant xerogel was dried in air at 110 °C for 4 h and calcined at either 650 or 850 °C for 2 h under air in a muffle oven. As summarized in **Table 2.2**, SnO_2, $(Sn,Ti)_xO_2$, and $(Sn,Ti,Nb)_xO_2$ powders were labelled according to the molar ratio between Sn, Ti, and Nb used for the synthesis and the calcination temperature.

Table 2.2 SnO_2 $(Sn,Ti)_xO_2$ and $(Sn,Ti,Nb)_xO_2$ sample labels according to the molar ratio between Sn, Ti and Nb used for the synthesis and the calcination temperature [12].

Sn:Ti:Nb molar ratio	Calcination temperature	Sensor label
100	650°C	SnO_2_650
70:30:0	650°C	ST30_650
70:30:0	850°C	ST30_850
66.5:28.5:5	650°C	STN5_650
66.5:28.5:5	850°C	STN5_850
67.6:28.9:3.5	650°C	STN3.5_650
67.6:28.9:3.5	850°C	STN3.5_850
69.0:29.5:1.5	650°C	STN1.5_650
69.0:29.5:1.5	850°C	STN1.5_850

All of the chemicals, with reagent-grade purity and without any further purification, were from Sigma-Aldrich. Double-distilled water passed through a Millipore Elix water purification system.

2.3 METHODS FOR MORPHOLOGICAL, CHEMICAL, AND STRUCTURAL CHARACTERIZATION OF SMOX MATERIALS

A wide characterization of semiconducting nanomaterials requires a comprehensive approach, by combining techniques in a complementary way. **Table 2.3** summarizes the methodologies used for the characterization of nanomaterials during the PhD period. Scanning electron microscopy (SEM), transmission electron microscopy (TEM) and high-resolution TEM (HRTEM) provided morphological information. X-ray powder diffraction (XRPD) data were collected to obtain the structural parameters. Energy-dispersive X-ray spectroscopy (EDX) and X-ray photoelectron spectroscopy (XPS) characterizations allowed to estimate the composition of the nanostructured films in the bulk and at the surface. To estimate the film porosity and Brunauer-Emmett-Teller (BET) surface area, nitrogen gas adsorption isotherms at 77 K were adopted. Electron paramagnetic resonance (EPR) spectral measurements were carried out to investigate the presence of paramagnetic species. The optical properties in the Ultraviolet-visible (Uv-vis) spectra were investigated by using a double beam spectrophotometer.

Table 2.3 Parameters determined and the corresponding characterization techniques used.

Entity characterized	Characterization techniques
Size (structural properties) and shape	SEM, TEM, HRTEM, XRPD
Elemental-chemical composition	XRPD, XPS, SEM-EDX
Crystal structure	XRPD, STEM, HRTEM
Chemical oxidation-state	XPS, EPR
Surface composition	XPS
Surface area, specific surface area and porosity	BET
Optical-electrical properties	UV-Vis-NIR

All the characterizations were possible thanks to the collaboration with the Department of Physics and Earth Sciences of the University of Ferrara, the Structural Characterization Department of the CNR-IMM division in Bologna, the MNF- Micro Nano Facility, Sensors and Devices center of Bruno Kessler Foundation in Trento and Cimprogetti S.r.l. Lime Technologies.

2.3.1 Electron microscopes

The morphology of nanostructured powders is commonly investigated by electron microscopes, i.e. scanning and transmission electron microscopes (SEM and TEM), which provide high-quality images of micro-nanoscale samples.

The electron microscopes have four key components, i.e. electron source, column, electronics and control software. The electrons are thermionically emitted from the electron source (W, LaB_6 or field emission guns) and are condensed into a nearly parallel beam at the specimen by the electromagnetic lenses placed along the column. Conventional electron microscopes require

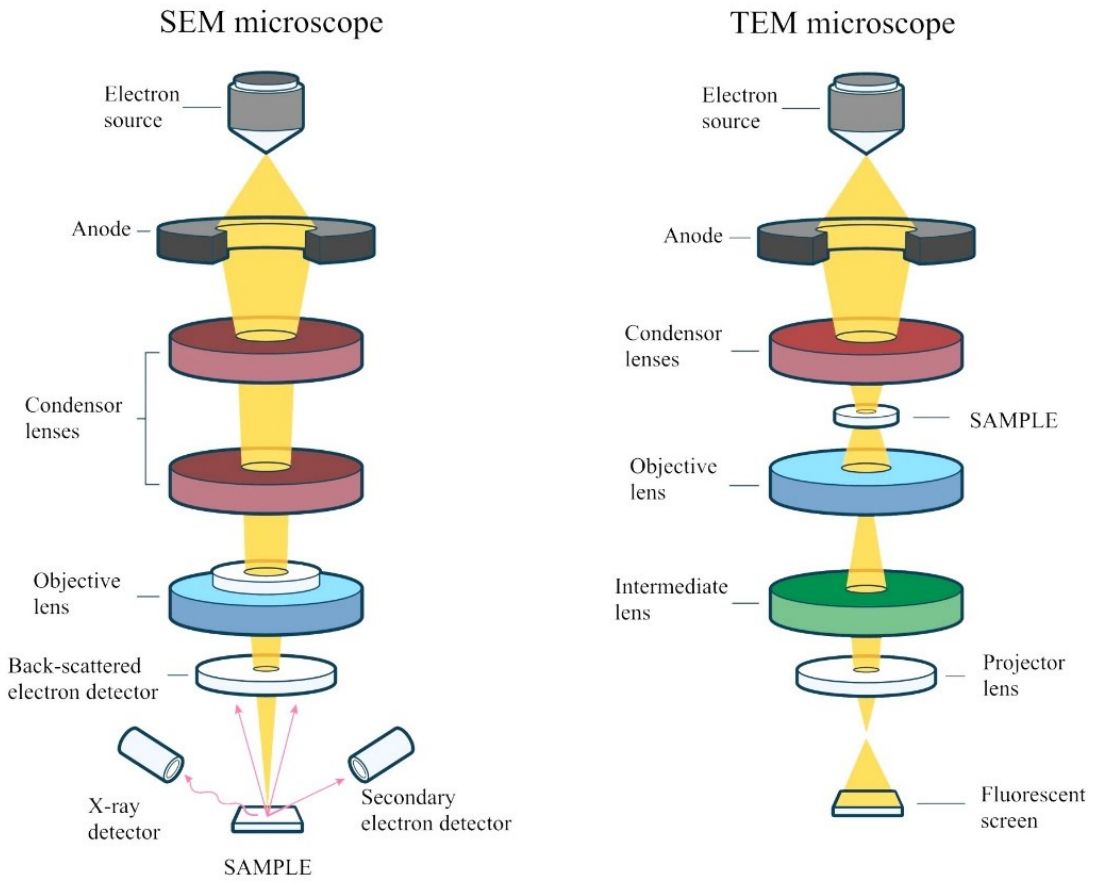

Fig. 2.2 The optics of a basic Scanning Electron Microscope (SEM) and basic Transmission Electron Microscope (TEM)

that the inside of the electron optical system and the specimen chamber are kept at high vacuum (10^{-3} to 10^{-4} Pa) because a gaseous atmosphere rapidly spreads and attenuates electron beams. The layout of optical components in a basic SEM and TEM microscope are shown in **Fig. 2.2** while **Table 2.4** lists their principal characteristics.

Table 2.4 Summary of the main differences between a SEM and a TEM.

Aspect / feature	SEM	TEM
High tension	0.2 – 40 kV	60-300 kV
Classification of electron used	Scattered (backscattered or secondary) electrons	Transmitted electron beam
Image formation process	Detection of primarily, secondary, and backscattered electrons from the sample surface	Fourier recombination of electrons that are scattered by the sample
Image presentation	3-D	2-D
Magnification	Up to 2 million magnification level	Up to 50 million magnification level
Resolution	0.4 nm	0.5 Å
Sample thickness	No restriction	Ultrathin samples only
Operation	Little or no sample preparation, easy to use	Laborious sample preparation, trained users required

The SEM instruments are typically coupled with the energy-dispersive X-ray spectroscopy (EDS or EDX), an analytical technique used for the elemental analysis or chemical characterization of a sample. EDX detects and analyses the energy of the X-rays that are generated by electron beam irradiation of the sample. The X-rays have energies that are unique for each element, so it is possible to determine the elements from the energy spectrum. Moreover, the intensity of the spectrum yields information about the relative composition.
The TEM instruments can also be equipped with a dispersion micro-analysis of energy (EDS) and a scanning TEM (STEM) accessory for elemental mapping. Moreover, modern TEM allows for selected area diffraction (SEAD) analysis which can be used to identify crystal structure, determine their orientations, examine crystal defects, measure crystal characteristics, or material texture.
The morphology of the sensing materials was investigated as received by SEM using a LEO 1530 FEG microscope or a Zeiss EVO 40 microscope. For TEM analyses, the powders were dispersed in isopropyl alcohol and sonicated for 20 minutes. The solutions were deposited on a perforated carbon film supported by a copper grid. The preparations were thus dried at 80 °C. The TEM analyses were performed with a FEI TECNAI F20 microscope operating at 200 keV. The instrument is also equipped with a dispersion micro-analysis of energy (EDS) and the STEM accessory. The TEM images were taken in the phase contrast mode and Selected Area electron diffraction (SAED). STEM pictures were recorded using a High Angle Annular Dark Field (HAADF) detector: in this imaging mode the intensity I is proportional to $Z^{1.7}t$, where Z is the mean atomic number and t is the thickness of the specimen.

2.3.2 X-ray powder diffraction

X-ray diffraction (XRD) provides information about the crystalline structure, nature of the phase, lattice parameters and crystalline size. The composition of the nanostructured powders can be determined by comparing the position and intensity of the peaks with the reference patterns available from the International Centre for Diffraction Data (ICDD) database [94].
XRD is based on constructive interference of monochromatic X-rays and a crystalline sample. X-rays are generated by a cathode ray tube and filtered to produce monochromatic radiation. The monochromatized beam passes through a slit which determines the angular width of the beam (smaller slits give less energy but better resolution) and is directed toward the sample. Crystalline materials are made up of many small crystals, and each of these crystals is composed of a regular arrangement of atoms. Since the X-ray wavelength is similar to the distance between atoms in the crystal, the incident X-rays are primarily scattered through elastic scattering by interaction with the atoms' electrons (scatterer). A regular array of scatterers produces a regular array of spherical waves. In the majority of directions, the waves cancel each other out through destructive interference. The interaction of the incident rays with the sample produces constructive interference (and a diffracted ray) only when conditions satisfy Bragg's Law, see **eq. 2.1** and **Fig. 2.3 a**, where λ is the wavelength of electromagnetic radiation, θ is the diffraction angle and d is the lattice spacing in a crystalline sample.

$$n\lambda = 2d\ sin\theta \quad eq.2.1$$

By scanning through a range of 2θ angles (**Fig. 2.3 b**) all directions which satisfy Bragg's Law appear as spots on the diffraction pattern and are called reflections. Conversion of the

diffraction peaks to d-spacings allows identification of the mineral because each mineral has a set of unique d-spacings.

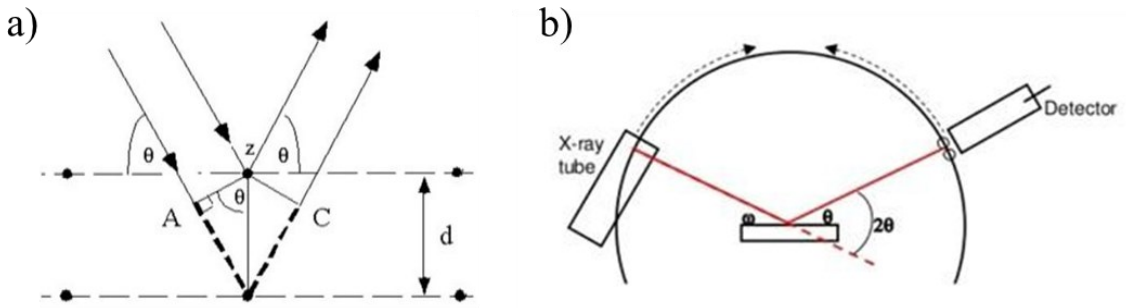

Fig. 2.3 a) The Bragg interpretation of scattering conditions and **b)** a schematic representation of an X-rays diffraction experiment.

X-ray powder diffraction (XRD) data were collected at room temperature on a Bruker D8 Advance Da Vinci diffractometer working in Bragg-Brentano geometry and equipped with a LynxEye XE silicon strip detector (angular range of the detector window size = 2.585° 2θ) set to discriminate Cu Kα1,2 radiation. Qualitative phase analysis of collected patterns was performed by means of the Bruker AXS EVA software (v.5) and refined by means of the fundamental-parameter approach (TOPAS v.5.0).

2.3.3 X-ray photoelectron spectroscopy

X-ray photoelectron spectroscopy is a surface sensitive technique which can detect all elements, except hydrogen and helium, existing within the material up to a depth of 5-10 nm from the surface [95]. The sample is irradiated with soft X-rays (energy lower than 6 keV) generated by an Al-anode. Photon's energy ionizes a core level electron when it interacts with a sample atom. An electron spectrometer with high resolution records the kinetic energy ($K.E.$) of emitted photoelectrons. The $K.E.$ of the emitted electrons is expressed as:

$$K.E. = h\nu - B.E. - \phi_{spec.} \quad eq.2.2$$

where $h\nu$ is the energy of the X-ray, $B.E.$ is the binding energy of the electron and $\phi_{spec.}$ is the spectrometer work function, a constant value (**Fig. 2.4**). High vacuum (≈ 10^{-10} torr) assists

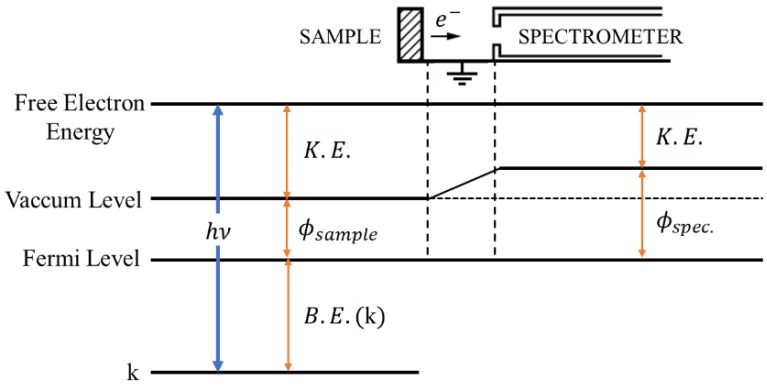

Fig. 2.4 Energy level diagram illustrates schematically the basic components of **eq. 2.2**, including the photon energy $h\nu$, the binding energy of the electron $B.E.$ and the spectrometer work function $\phi_{spec.}$.

photoelectron transport to the analyser and avoids recontamination of clean samples. A typical XPS spectrum is obtained at a given photon energy by recording the number of photoelectrons as a function of the $B.E.$ obtained from **eq. 2.2**. Since the $B.E.$ are different for each chemical element, the technique determines the surface composition of an unknown sample and assesses its degree of cleanliness. Moreover, the $B.E.$ of a given element depends on the chemical environment of the atoms and energy shifts may occur when inequivalent atoms of the same elemental species are present. By comparing the data of well-known standard substances, the $B.E.$ shifts can be used to determine oxidation states and to gain insight into the nature of the chemical bonds formed by the atoms.

X-ray Photoelectron Spectroscopy (XPS) analyses were performed using Kratos AXIS UltraDLD instrument (Kratos Analytical, Manchester, UK) equipped with a hemispherical analyser and a monochromatic Al Kα (1486.6 eV) X-ray source, in spectroscopy mode. The analyses were performed with a take-off angle between the analyzer axis and the normal to the sample surface of 0°. For the measurements, the powders were attached to the sample holder using double-sided carbon tape. For each sample, the survey, the high-resolution scans of the Sn 3d, Ti 2p and Nb 3d core levels were collected. XPS quantification was performed using the instrument sensitivity factors and the high-resolution scans. Charge compensation was achieved using a flood gun and all core levels were referenced to the C-C/C-H component in C 1s at 285.0 eV. All XPS data were analyzed using the software described in Speranza and Canteri [96].

2.3.4 Micromeritics automated gas sorptometer

A Micromeritics automated gas sorptometer is a surface area and porosity analyser. Nitrogen is the most commonly employed gaseous adsorbate for probing surface(s). For this reason, standard BET analysis is most often conducted at the boiling temperature of N_2 (77 K). Successive doses of the adsorptive gas probe are sent to the solid material, preliminarily dried, and evacuated. The amount of gas molecules that can adsorb onto the surface of the solid is derived from the evolution of the pressure in the system. The cumulative amount of adsorbate plotted with respect to the pressure is the adsorption isotherm. The specific surface area (m^2/g) of solid phase, porous materials, is estimated using the Brunauer, Emmett and Teller (BET) theory from a specific region of a gas adsorption isotherm where inert gas molecules form a monolayer on the solid substrate due to weak van der Waals forces.

According to the ISO 9277:2010(E), the BET method is applicable only to adsorption isotherms of type II (disperse, nonporous or microporous solids) and type IV (mesoporous solids, pore diameter between 2 nm and 50 nm).

Gas porosity and specific surface area of the powders were investigated using a Micromeritics TriStar II Plus automated gas sorptometer, with nominal resolution of > 0.01 m^2/g. The running program of N_2 adsorption-desorption isotherm consisted of 83 points of relative pressure, from 0.05 (p/p_0) up to 1.00 (p/p_0) and back, being p the pressure of the adsorptive in equilibrium with the adsorbate and p_0 the saturation vapour pressure of the adsorptive. The specific surface area was determined according to Brunauer-Emmett-Teller Specific Surface Area (BET-SSA) theory [18]. Pore volume and pore-size distribution (PSD) were determined according to Adsorption/Desorption Barrett-Joyner-Halenda (BJH) method and to the method of non-local density functional theory (DFT), respectively.

2.3.5 Electron paramagnetic resonance spectroscopy

Electron paramagnetic resonance spectroscopy (EPR) is a non-destructive, non-invasive, highly sensitive and accurate analytical technique used to detect and to characterize paramagnetic chemical species, i.e. possessing unpaired electrons.

A conventional continuous wave spectrometer is composed of the source components, the magnet system, the detection system, and the modulation system (**Fig. 2.5**). The sample is placed in a cavity situated between the poles of two magnets. The electron, as a charged rotating particle, possesses a magnetic field which makes it appear as a minute magnet. In normal cases, for the unpaired electron, the spin energy levels are degenerate, and electrons spin randomly (**Fig. 2.6 a**). When an external magnetic field, B, is applied, spin energy levels split, and electrons spin either aligned to or opposite to the direction of the magnetic field (**Fig. 2.6 b**). Splitting of the spin energy levels results in the emergence of an energy difference (ΔE), expressed in **eq. 2.3**, where g_e=2.0023 is the electron's so-called g-factor, i.e. the spectroscopic splitting factor, for a free electron, B is the external magnetic field, M is the electron's magnetic aligns, i.e. antiparallel $M = -\frac{1}{2}$ or parallel $M = +\frac{1}{2}$ to the field, and μ_B is the Bohr magneton.

$$\Delta E = g_e B M \mu_B \quad eq. 2.3$$

Electrons aligned parallel to the external magnetic field and occupying the lower energy level are more than those aligned antiparallel to the external magnetic field and occupying the upper energy level.

At the same time, the microwave (MW) source controls and directs high frequency electromagnetic radiation (MW in the 9–10 GHz region). When incident photon energy ($h\nu$) matches the energy difference between the two spin energy levels, some electrons are excited in the upper energy level and flip their spin direction. After the relaxation time (T_1), excited electrons return to their original state emitting photons whose energy is equal to ΔE (**Fig. 2.6 c**).

EPR spectra can be generated by either varying the photon frequency incident on the sample while holding the magnetic field constant or doing the reverse. In practice, usually the paramagnetic sample is exposed to microwaves at a fixed frequency, while the external magnetic field is increased. When the gap ΔE is widened until the same energy of the

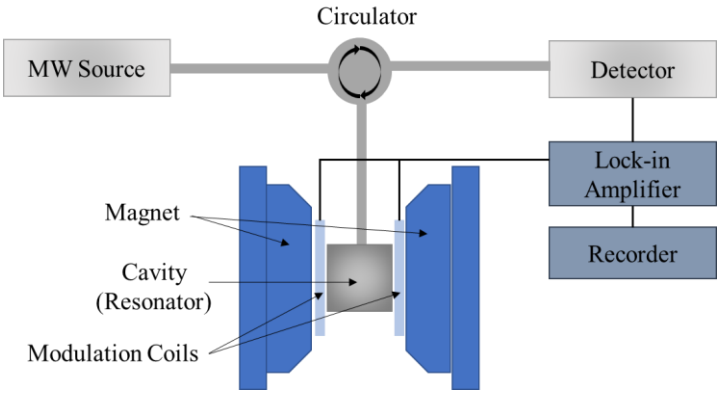

Fig. 2.5 Schematic diagram of an EPR spectrometer for conventional continuous wave measurements.

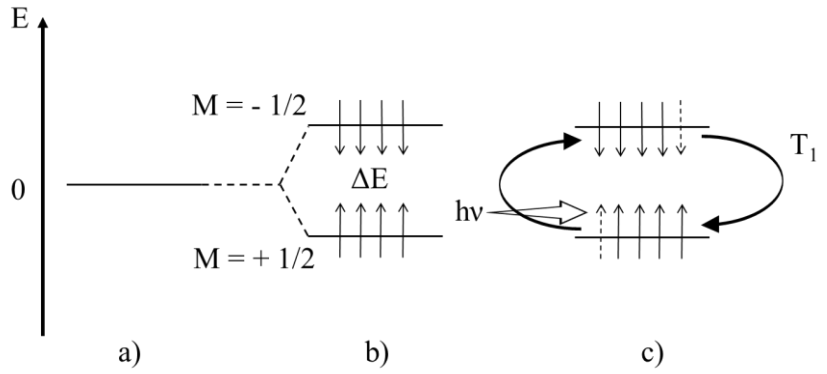

Fig. 2.6 a) Condition of absence of applied field and no spin levels splitting. **b)** Energy separation of unpaired electron spin under a magnetic field (Zeeman effect). **c)** Flipping of spins by microwave adsorption and flopping of spins within the spin lattice relaxation time, T_1 [214].

microwaves, the unpaired electrons absorb the photons to move from the lower state $M = +\frac{1}{2}$ to the upper state $M = -\frac{1}{2}$ and this absorption is monitored and converted into a spectrum. The most common wat to publish continuous wave EPR spectra is the first derivative of the absorption spectrum.

The samples, under the form of loose polycrystalline fine powders, were analysed without any pre-treatment or manipulation. An aliquot of the sample was inserted in amorphous silica tubes, through the use of Teflon bags. The tubes were chosen to avoid the presence, in the glassy matrix, of transition metal impurities (mainly Fe or Cr), whose characteristic lines likely interfere with the EPR spectra of the samples. The EPR spectral measurements were carried out using a conventional Bruker ER 200D-SRC instrumentation, operating at ~9.5 GHz (X-band), available at the Department of Chemistry of the University of Florence. Spectra were registered, at room temperature, 4 mT modulation amplitude, and 100 KHz modulation frequency. The post-amplification gain set up was optimised to maximise the signal-to-noise-ratio. The spectra of all samples were registered in a 0-1000 mT magnetic field range (panoramic scan), with a field step of 0.489 mT, and at a scan speed of 5 mT/s. For selected samples, where specific lines were identified during the panoramic scan, a detailed scan was also registered. The conditions were set up to 270-360 mT magnetic field range, 0.088 mT field step, and 0.9 mT/s scan speed.

2.3.6 UV-visible spectroscopy

UV-vis spectroscopy concerns absorption or reflectance spectroscopy in part of the ultraviolet (185-400 nm) and the full, adjacent visible (400-700 nm) regions of the electromagnetic spectrum. A schematic of a UV-vis spectrophotometer is shown in **Fig. 2.7**. It consists of a spectrometer, which generates the desired range of wavelengths, and a photometer, which measure the intensity of light after it has passed through a sample (I_t) and compares it to the intensity of light before it has passed through sample (I_0). Then, the transmittance T, i.e. the fraction of light that passes through the sample, can be calculated using the **eq. 2.4**.

$$T = \frac{I_t}{I_0} \quad eq.2.4$$

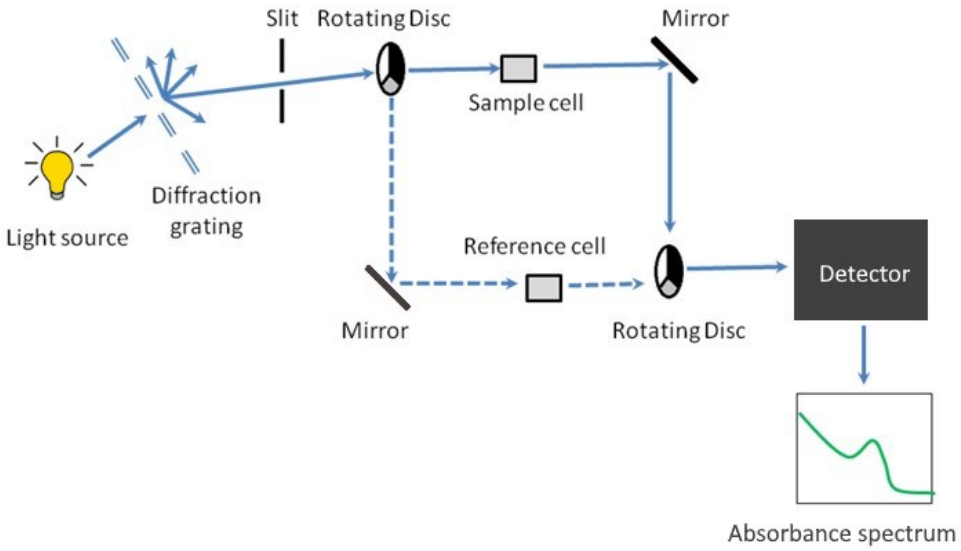

Fig. 2.7 Schematic of UV-visible spectrophotometer. The light source uses a combination of deuterium lamp for the UV region and tungsten or halogen lamp for the visible region. The beam of light is sent through the diffraction grating which separates its component wavelengths and a slit selects a monochromatic beam. A system of rotating disc and mirror directs the beam to the sample cell and to a reference cell and then to the detector which converts light into a current signal that a computer can read.

The transmittance is related to the number of photons that is absorbed, i.e. absorbance (A), by the expression:

$$A = -\log(T) \quad eq.2.5$$

Therefore, the spectrum provides information about the electronic transitions due to light absorption occurring in the material. This methodology is widely used in diverse applications because it is relatively inexpensive and easily implemented. In particular, the UV-vis optical characterization in combination with the Tauc method is the most widely applied procedure for optical band gap determination of semiconductors, which is often approximated to the electronic band gap because there are few convenient methods for measuring the latter.
The Tauc method assumes that the energy-dependent absorption coefficient α can be expressed by the following equation:

$$(\alpha \cdot h\nu)^{1/\gamma} = B\left(h\nu - E_g\right) \quad eq.2.6$$

where h is the Planck constant, ν is the photon's frequency, E_g is the band gap energy, and B is a constant. The γ factor depends on the nature of the electron transition and is equal to ½ or 2 for the indirect and indirect transition band gaps, respectively [97]. The optical gap energy is determined according to the Tauc method by simply fitting a straight line (Tauc line) to the linear (or steepest) region of the optical spectrum to intersect the photon energy (hv) axis.
The optical absorption analysis was performed by using a JASCO V-670 double beam spectrophotometer. The instrument was equipped with both a deuterium (190-350 nm) and a halogen (330-2700 nm) lamp. The measurement was carried out in the wavelength range 200-800 nm, with a sampling interval of 1 nm. The powder was dispersed in 2-propanol to carry out the measurement. The band gaps of the nanostructured semiconductor were calculated by using the Tauc's method.

2.4 PROCESSES FOR THICK FILM SENSORS PREPARATION

Gas sensors can be constructed by using both thick and thin film technology. Thick films (thickness more than 1 µm) are produced by firing a special paste (usually consisting of glass and metal oxides) onto a substrate. They have the advantage of more robust construction and ease of deposition by means of relatively cheap techniques (i.e., screen-printing), but the sensors generally presents longer stabilizing times and have high power consumption [98]. Thin films (thickness between 5 nm and 1 µm) are commonly sputtered (vacuum deposition) and require more expensive and complex systems for the deposition (i.e., sputtering, chemical vapor deposition) [98]. The layers are usually dense and uniform (low surface-to-volume ratio) and more unstable than the thick ones. On the other hand, sensors based on thin films feature lower power consumption.
Thick-film sensors studied in this work were produced from nanostructured semiconducting materials, synthesized in powder form, using the commercially attractive and low-cost screen-printing process.

2.4.1 Screen-printing deposition

The screen-printing method consisted in the production of pastes based on the nanostructured powders, which were then deposited on substrates. In addition to the active nanostructured materials, the pastes were composed of additives, i.e. alpha-terpineol, ethyl cellulose and fried, to provide the suitable viscosity for their deposition and to assist the temperature-induced film treatments. Alpha-terpineol is an organic vehicle and one of the most used solvents for electronic thick film paste. Ethyl cellulose is an organic binder which increases the shear-thinning pseudoplasticity and the thixotropy of the paste, to ensure its flow in the screen mesh and to maintain the shape of the printed pattern before the heating treatment [99]. The fried is

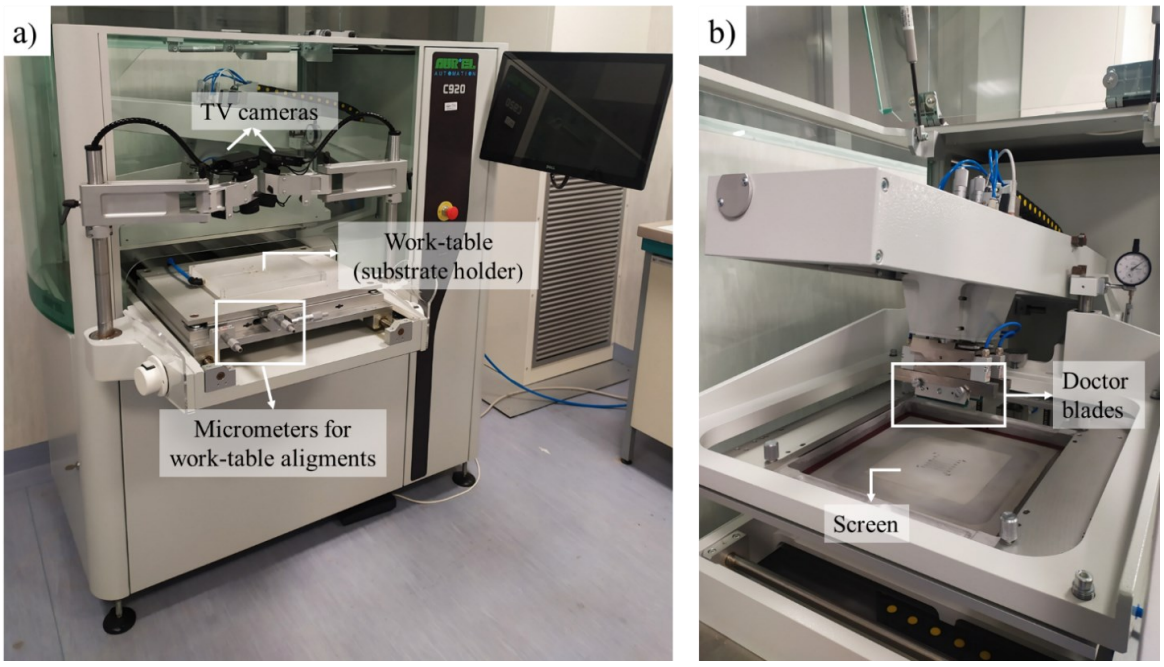

Fig. 2.8 a) AUREL C920 screen printing machine for thick film deposition. TV cameras allow accurate alignment of the work-table by manual micrometers. **b)** Two doctor blades force the sample paste through the screen, over the alumina substrate.

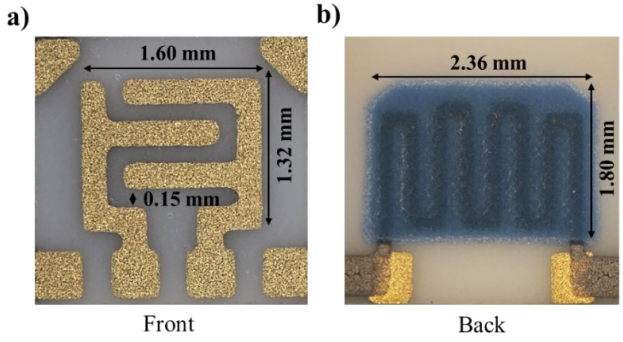

Fig. 2.9 Photo with dimensions of **a)** the interdigitated electrodes on the front and **b)** the heater on the back of a sensor working in thermo-activation mode.

a powder consisting of a mixture of glassy oxides based on silica (SiO_2) charged with alkaline-earth oxides or with oxides of the IV group. It has the function of improving the mechanical resistance of the film and its adhesion to the substrate.

The paste was then printed through the AUREL C920 screen printer (**Fig. 2.8 a**). The instrument consists of two plastic spatulas (called doctor blade) which force the paste through a screen to deposit it with a predefined shape onto alumina substrates (see **Fig. 2.8 b**). The machine is PC controlled and is equipped with a vision system and two TV cameras to simplify the alignment operation between screen and substrate. On the front side of the alumina substrate, two interdigitated gold electrodes supply the input voltage and extract the output signal (**Fig. 2.9 a**). Moreover, a platinum screen-printed heater on the backside allows the thermo-activation of the sensing film (**Fig. 2.9 b**). The heater resistance R_h increases with the temperature according to **eq. 2.7**, in which T is the working temperature, R_0 is the resistance at 0 °C and α and β are constants of the material. To operate the heater, a voltage V_h is applied to reach R_h according to Ohm's law (**eq. 2.8**).

$$R_h = R_0(1 + \alpha T + \beta T^2) \quad eq.\,2.7$$

$$R_h = \frac{V_h}{i} \quad eq.\,2.8$$

The film printed on the substrate undergoes two different heating treatments. The first is a low-temperature treatment at 100-180°C to dry the film and remove the volatile organic compounds. The second is a firing at high temperature, i.e. in the range of 500-650°C, in a muffle furnace to complete the decarbonation process of the film and to melt the fried. The two-step procedure is crucial to limit the formation of cracks and obtain a uniform and compact film.

All the processes took place in a laminar flow clean rooms for preparation of samples in an optimal environment.

2.4.2 Sensor final manufacture

The heater and the interdigitated gold electrodes were interfaced to the electronic system by connecting them to the pins of a commercially available TO39 support (see **Fig. 2.10 a** and **b**). Golden wires (99.99%) with a diameter of 0.06 mm were used for the connection between the elements on the substrate and the pins of the support. The wires were welded by thermo-compression through the wedge wire bonder in **Fig. 2.9 c**.

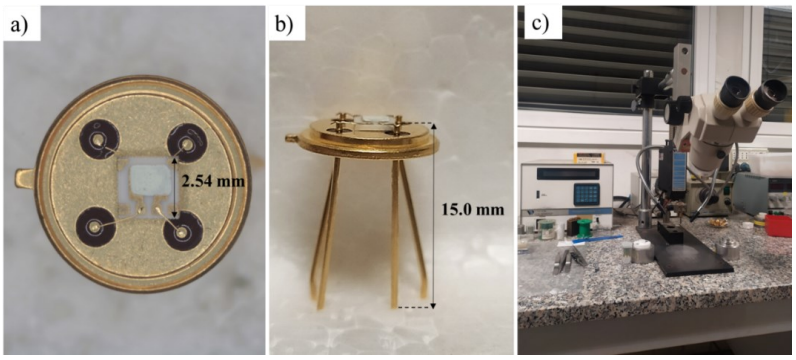

Fig. 2.10 Photo of the device composed by **a)** a screen-printed WO_3 film on alumina substrate (2.54x2.54 mm^2) packaged on **b)** a standard TO-39 support (15.0 mm high) by using thermo-compression bonding and a gold wire (0.06 mm of diameter) through **c)** a wedge wire bonder.

2.5 SENSORS ELECTRICAL CHARACTERIZATION

The sensors were electrically characterized in the apparatus showed in **Fig. 2.11**, which mainly consisted of:

- net of tubes and pneumatic system based on mass-flow controllers for preparation of gas mixtures precisely controlled in concentration from certified cylinders;
- sealed test chambers;
- data acquisition systems.

Synthetic air (20 %O_2 and 80 % N_2) and target gases from certified cylinders (N5.0 degree of purity) were mixed and fluxed in a hermetically sealed chamber with cylindrical shape (volume: 622 cm^3). A pneumatic system based on MKS mass-flow controllers was used to set the gas flow rate. Sensors were let stabilized at the beginning of each measurement under a continuous

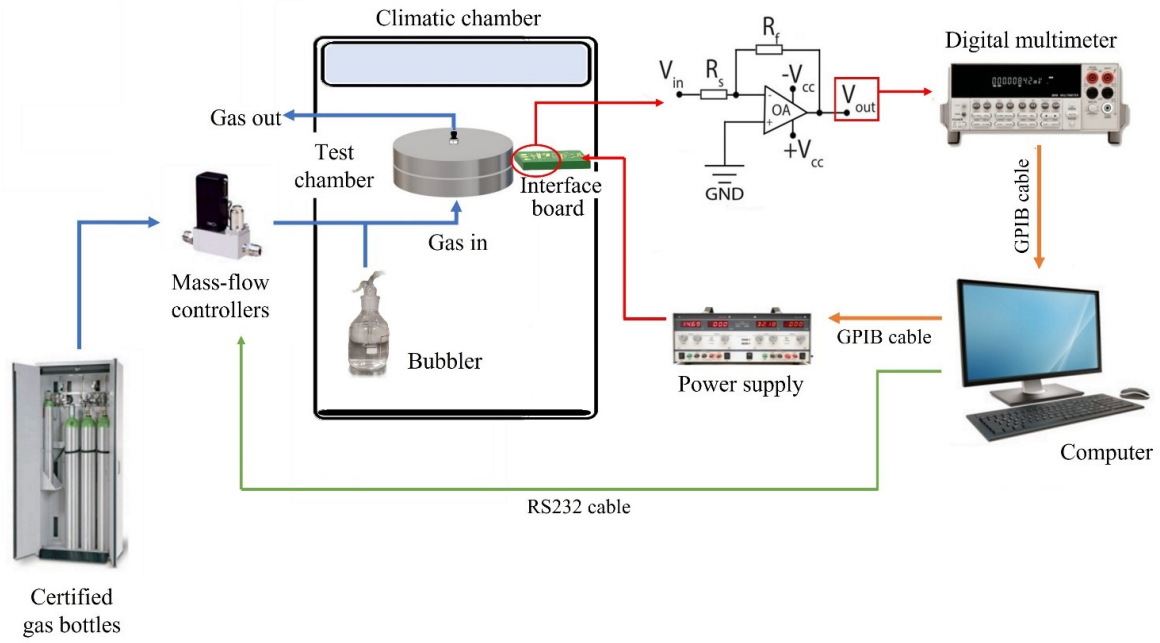

Fig. 2.11 Schematic representation of the gas flow control and the data acquisition system. Blue arrows are gas tubes while red, orange, and green arrows are different types of electrical cables.

flow of either synthetic dry or wet air. The sensors were positioned circularly around the gas diffuser. Moreover, a temperature and a humidity sensor (Honeywell HIH-4000) were set at the center of the chamber. The filling time, calculated as in **eq. 2.9**, was about 1 min 15 sec. Wet conditions were obtained by fluxing synthetic air through a bubbler filled with deionized water. The humidity sensor continuously measured the relative chamber humidity (RH – Relative Humidity) expressed as a percentage (0–100%). RH%, according to the definition, is the amount of water vapour present in a specific volume expressed as a percentage of the amount required for saturation at the same temperature. To flush the desired gas concentration C into the chamber, the gas concentration in the cylinder C_{cyl} (certified by the supplier) was diluted using synthetic air. Therefore, in all experiments the total flow rate was maintained at 500 sccm, partly consisting of the target gas flow rate, calculated as in **eq. 2.10**, and partly of the air flow rate.

$$\frac{Chamber\ volume}{sccm} = \frac{622cm^3}{500\frac{cm^3}{min}} \quad eq.\ 2.9$$

$$F = \frac{F_{tot} \times C}{C_{cyl}} \quad eq. 2.10$$

Power suppliers (Aim TTi) and a multimeter (K2000 (Keitheley)) were used to provide the electrical current to the sensor heater and to read the electrical conductance of the sensing film, respectively. The electronic system (**Fig. 2.11**) for the sensing material readout was based on an operational amplifier (OA) in inverting configuration. The other components are the sensors resistance R_S and the load feedback resistor R_f. Moreover, V_{in} is the bias voltage value, fixed at - 5 V and V_{out} is the output voltage. Being known the values of R_f, $V_{in}$and V_{out}, the R_S is $-V_{in}R_f/V_{out} = R_S$ and the expression for the sensor conductance was G_s:

$$G_s = \frac{1}{R_S} = \frac{V_{out}}{R_f \times V_{in}} \quad eq. 2.11$$

G_s were collected by using a data acquisition software developed in LabVIEW [29]. The sensor response of n-type SMOX was defined as in **eq. 2.12** and **2.13** for reducing and oxidizing gases, respectively, where $G_{baseline}$ is the steady state conductance before injection of the analyte and G_{gas} is the steady state conductance in presence of the target gas.

$$R = \begin{cases} \frac{(G_{gas} - G_{baseline})}{G_{baseline}} & eq. 2.12 \\ \frac{(G_{baseline} - G_{gas})}{G_{gas}} & eq. 2.13 \end{cases}$$

2.6 *OPERANDO* DRIFT CHARACTERIZATION SETUP

Infrared (IR) spectroscopy is a powerful tool for the identification of organic and inorganic compounds because all molecules absorb IR radiation, with the only exception of homonuclear compounds, i.e. N_2, O_2 and Cl_2. Therefore, the surface interaction between the most promising samples and the target gases was studied by operando Diffuse Reflectance Infrared Fourier Transform (DRIFT)-spectroscopy.

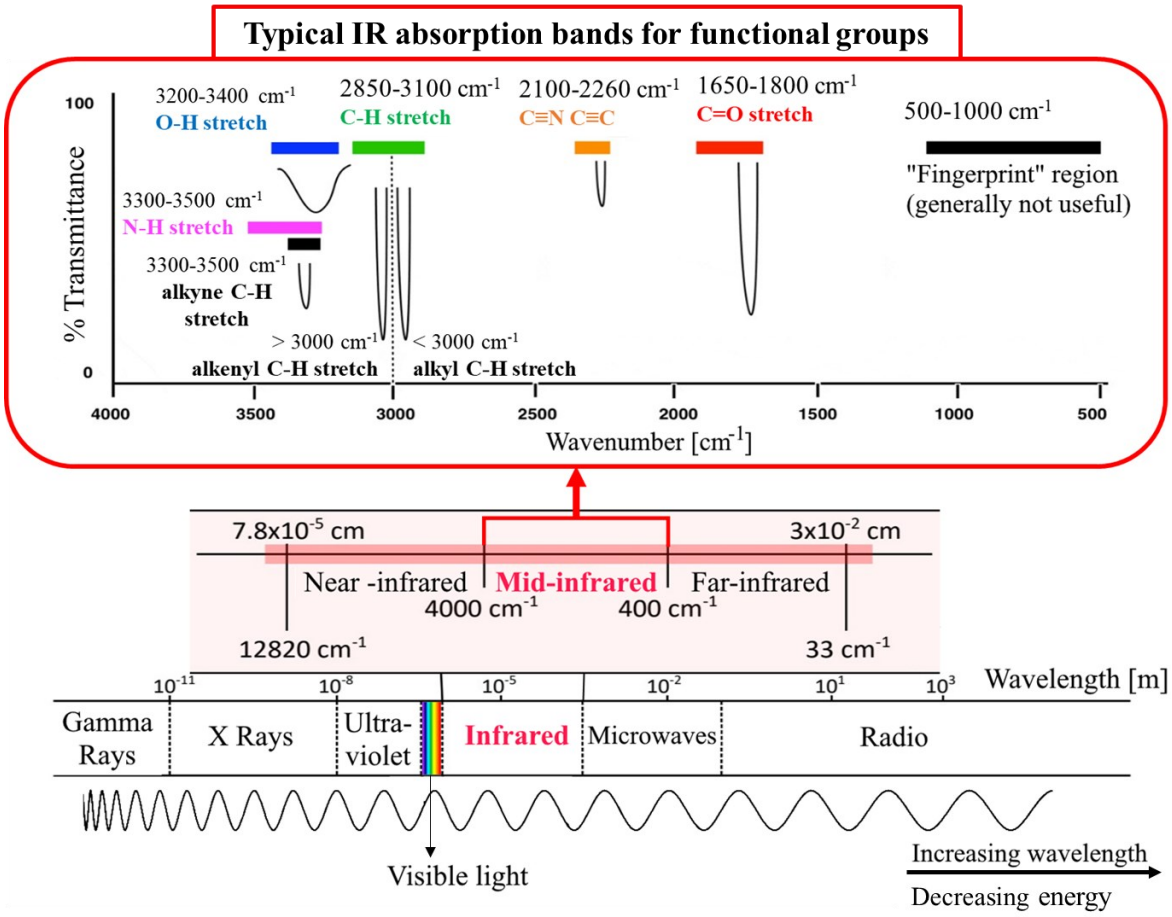

Fig. 2.12 Schematic representation of an IR spectra. The vertical axis is the % transmittance, which indicates how strongly light is absorbed at each frequency. The horizontal axis represents the position of an absorption band. Wavenumbers (in unit of cm^{-1}), i.e. $1/\lambda$, are used as a conventional way in IR spectra.

The technique investigates fundamental molecule vibrations by exploiting the mid-infrared (mid-IR) radiation, which is the portion of the electromagnetic radiation whose wavenumber is located between 4000 and 400 cm^{-1} (see **Fig. 2.12**). The energy of radiation in the mid-IR corresponds to the energy difference for transitions between the ground state (ν_i=0) and the first excited state (ν_i=1) of most vibrational modes. The degrees of vibrational modes for linear and non-linear molecules can be calculated using the formula 3N−5 and 3N−6, respectively, where N is equal to the number of atoms within the molecule of interest. Vibrational modes can be divided into stretching (symmetric and asymmetric) and bending vibrations (in-place and out-plane). According to the selection rule, vibrations are IR active only if they induce molecular dipole moment changes [100].

The frequency of vibrational modes of atoms is characteristic of specific functional groups, i.e. atoms mass and bond strength between them, and is minimally affected by the nature of other atoms in the molecule. In the classical description, if the two atoms in the molecule are considered as a system of two oscillating masses joined by a massless spring, then the wavenumber $\tilde{\nu}$ of this harmonic oscillator is given by the formula:

$$\tilde{\nu} = \frac{1}{2\pi c}\sqrt{\frac{k}{\mu}} \quad eq.\,2.14$$

where c is the speed of light, μ is the reduced mass and μ is the spring force constant. According to **eq. 2.14**, stronger bonds and light atoms vibrate at a high stretching frequency (wavenumber) [101]. Thus, the observation of distinctive spectral features in a certain region of the spectrum is often indicative of a specific chemical functional group in the molecule (see **Fig. 2.12**) [102]. IR methods can be divided into transmissions methods, that rely on the absorption of IR radiation as it passes through the sample, and reflectance methods, in which the IR radiation interacts with the surface of the material and is reflected [103]. **Fig. 2.13** schematically represents the most common methods, i.e. **a)** transmission Fourier transform IR (FTIR), **b)**

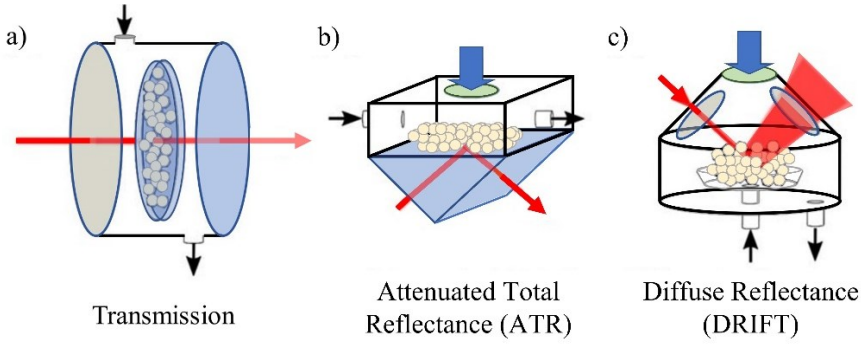

Fig. 2.13 Schematic representation of **a)** transmission FTIR, **b)** ATR FTIR and **c)** DRIFT measurements for the characterizations of nanoparticles. The figure has been adapted from [103]. IR and UV/Vis transparent materials are highlighted in blue and green, respectively. Red and blue arrows represent the beam path for IR and UV/vis light. Black arrows illustrate gas inlets and outlets.

attenuated total reflection (ATR) FTIR and **c)** DRIFT measurements. Between them, DRIFT is the most powerful method when it comes to examining rough-surfaced solid samples or powders [104], e.g. it is extensively used for in situ monitoring on nanoparticle surface of reactions with gaseous and adsorbed species [105–107] or to study solid oxide catalysis under operative conditions [108]. Moreover, it requires easy sample preparation. For these characteristics, it has been used for operando measurements on gas sensors based on SMOX-thick films [34,109–111].

The complete description of the experimental setup for operando DRIFT is reported in Ref. [109]. The setup uses a FTIR Vertex 70v spectrometer from Bruker equipped with a mercury-cadmium-telluride (MCT) narrow band detector with BaF windows. The system includes the DRIFT praying Mantis accessory by Harrick Scientific. The gas test chamber and mirror optics were placed inside the instrument sample compartment. Optical bench and sample compartment were evacuated during DRIFT measurements to avoid the interference of water vapour or CO_2 adsorption along the optical path from the source and the detector. The instrument can run the sensor in thermal or photo activation and read-out the electrical characteristics of the sensing film during the acquisition of DRIFT spectra.

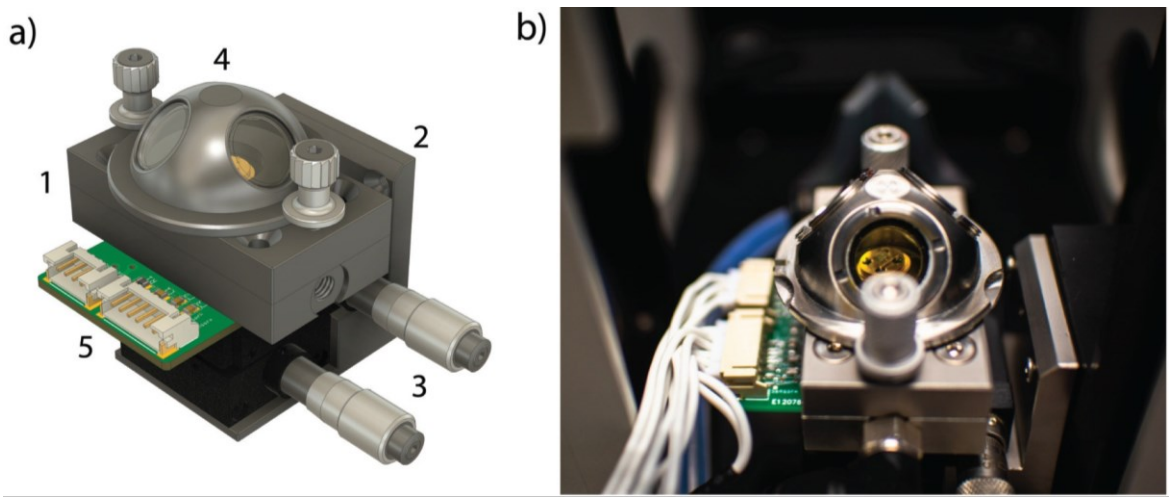

Fig. 2.14 a) 3D model and **b)** photo of the operando gas test chamber. In **a)** are represented the main cell body (1), the cell support (2), the vacuum compatible precision XY micro-stage (Standa) (3), the IR dome (4) and the connection for electrical measurements via JST connectors (5). Figure reprinted from [109].

The resistance of the sensor was calculated as the ratio of the applied voltage vs. the current. The gas sensor was located inside the gas test chamber, together with a commercially available Sensirion SHT3X sensor for temperature and relative humidity monitoring. The gas test chamber, represented in (**Fig. 2.14 a** and **b**), was composed of a main cell body and cell support in 316L stainless steel (SS), a vacuum compatible precision XY micro-stage (Standa), a dome with two monolithic ZnSe IR windows and a SiO_2 window for visual alignment (with NIR source), and a connection for electrical measurements via JST connectors. A pneumatic system based on Brooks SLA5800 mass-flow controllers was used to set the flow rate of the gases coming from the certified cylinders. Humid air was obtained by fluxing synthetic air through a bubbler filled with deionized water. A vacuum compatible precision XY micro-stage (Standa), coupled with the Z-axis control system present in the Harrick's Praying Mantis, allows the precise alignment of the SMOX film with the IR beam. Operando DRIFT spectra were recorded with a resolution of 1 cm^{-1} and as an average of 600 scans. Bruker's OPUS software was used to process the IR spectra. To determine the differences in the material resulting from changes in the environmental gaseous composition, absorbance spectra were calculated as apparent absorbance (AB) using **eq. 2.15**:

$$AB(\lambda) = -log_{10}\frac{I_{sample}(\lambda)}{I_{background}(\lambda)} \quad eq.\,2.15.$$

$I_{background}(\lambda)$ and $I_{sample}(\lambda)$ are the intensity of the spectrum (SC) of the sample recorded during exposure to synthetic air and that recorded during exposure to the analyte, respectively.

Chapter 3- CHARACTERIZATION OF THE SENSING MATERIALS

3.1 MORPHOLOGICAL, CHEMICAL, AND STRUCTURAL CHARACTERIZATION OF SMOX MATERIALS

3.1.1 WO_3

XRD analysis revealed that the powders were biphasic, composed (~98.6 wt%) by WO_3 in monoclinic phase (s.g. P21/n) and, as a minor constituent (~1.4 wt%), by WO_3 in hexagonal phase (s.g. P63/mcm). The main monoclinic phase (starting structural model from Woodward et al. [112], ICSD 80056) along with the associated hexagonal phase (starting structure model from Oi et al. [113], ICSD 80634) were modelled by carrying out a multiphase refinement in which only the scale factors and unit-cell parameters were varied. The refinement plot is shown

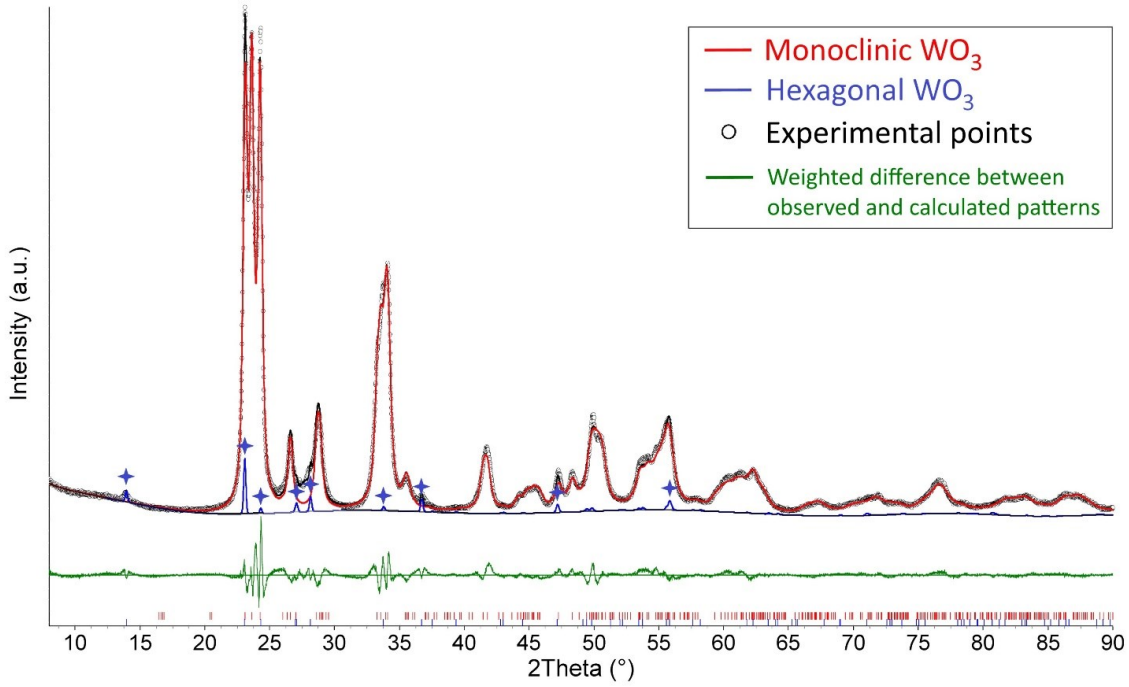

Fig. 3.1 Rietveld refinement plots of the powder diffraction pattern collected at RT. The experimental profile is represented by black dots, the best-fit refinement profile is the continuous black line, and the background fit is the grey curve. The lower green curve is the weighted difference between observed and calculated patterns. Phase contribution for the monoclinic and the hexagonal WO_3 phases are the red and blue curves. Vertical red (monoclinic) and blue (hexagonal) ticks mark the position of reflections for the two phases. Blue crosses mark the position of the most intense peaks for the WO_3 hexagonal phase. (For interpretation of the references to colour in this figure legend, the reader is referred to the web version of this article). Figure reprinted from [90].

Table 3.1 Quantitative phase analysis and unit-cell parameters with their standard deviations for the WO_3 sample collected at RT. The R-weighted pattern refinement agreement factor was RWP = 0.071, indicating the good quality of the fit [90]**.**

Phase	Weight %	space group	a(nm)	b(nm)	c(nm)	β(°)	Cell volume (nm^3)	Crystallite size (nm)
WO_3 monoclinic	98.55(5)	$P2_1/n$	0.73341(5)	0.75290(5)	0.76891(6)	90.631(8)	0.42455(5)	49(1)
WO_3 hexagonal	1.45(5)	$P6_3/mcm$	0.73159(14)	–	0.77014(13)	–	0.35697(15)	–

in **Fig. 3.1**, and quantitative phase analysis and unit-cell parameters are summarized in **Table 3.1**.

The morphology of the screen-printed film was observed by SEM (**Fig. 3.2 a** and **b**). The investigated sample was composed of nanoflakes (WO_3 NF) with a thickness of 20−30 nm and an elongation ranging from 200 nm to 1 μm. The elongation was larger than the crystallite size in **table 3.1**, meaning that an individual nanoflake was composed of several crystallites. The chemical composition was analyzed by EDX spectroscopy (**Fig. 3.2 c**). WO_3 NF were mainly composed of oxygen (73.94 atomic%), tungsten (22.68 atomic%) and with impurities of carbon (3.38 atomic %), confirming that the films after calcination were tungsten oxide with marginal atomic concentration of carbon due to the organic precursors used to prepare the paste screen-printed [90].

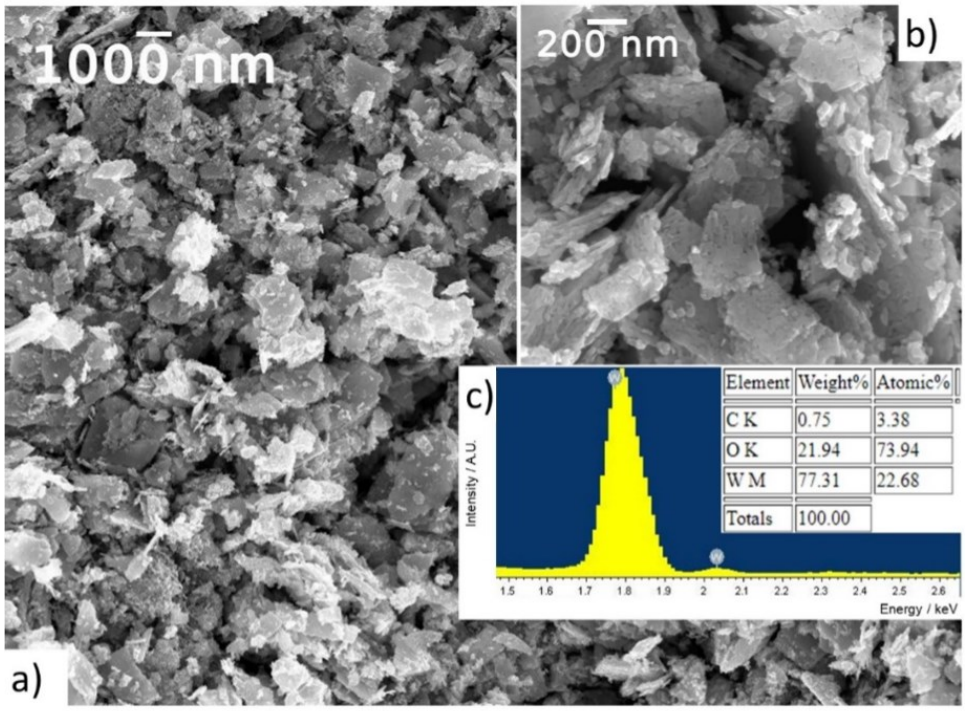

Fig. 3.2 a) SEM image of WO_3 NF film composed by nanoflakes and **b)** its magnification, highlighting the 20-30 nm thickness of the nanoflakes. **c)** EDX peaks with estimated chemical composition, showing it is tungsten oxide. Figure reprinted from [90].

The adsorption and desorption isotherms of WO_3 NF powder represented in **Fig. 3.3 a** should be classified as type-IV, with a small hysteresis loop in the range of 0.8–1.0 p/p_0, which indicated the presence of a porous structure according to IUPAC classification [18]. From the

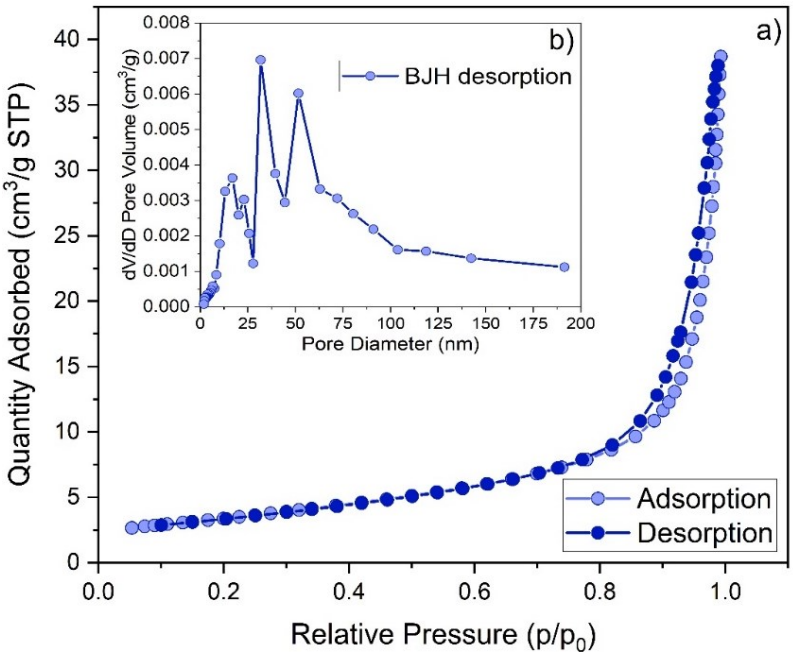

Fig. 3.3 a) N_2 isotherm profile, classified as type-IV, and **b)** the corresponding pore-size distribution curve, showing the meso-macroporous structure of the sample. Figure reprinted from [90].

calculated pore size distribution (**Fig. 3.3 b**) can be inferred that the sample exhibited a meso-macroporous structure, as most of the pores fell into the 10−90 nm range. The N_2-BET surface area was 12.11 m^2 /g, and the average pore size was 20.4 nm.

Both SEM and BET analysis highlighted that the film exhibited a porous morphology with a large specific area – an ideal feature for gas sensing – which will play a significant role for the interpretation of reaction mechanisms at surface.

Fig. 3.4 displays the optical absorption spectra of the WO_3 powders, collected by using a UV–vis spectrometer. The optical band gap energy (E_g) was estimated by using the Tauc's plot

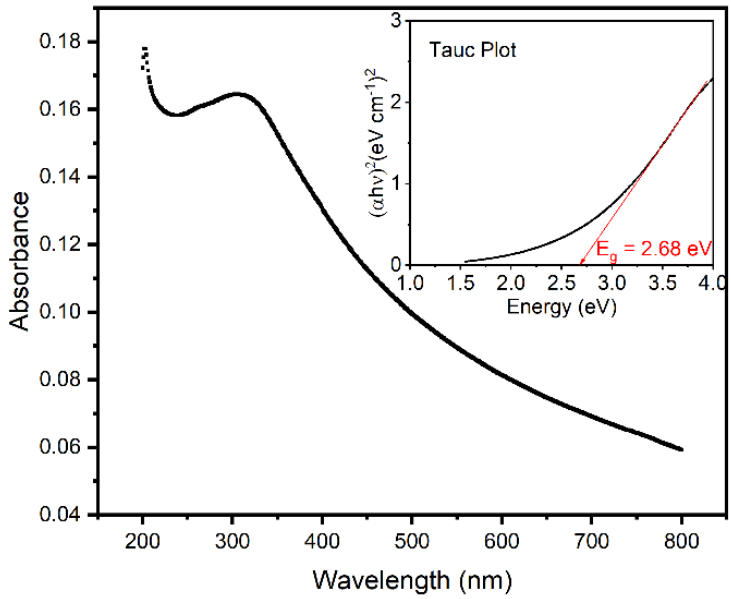

Fig. 3.4 Absorbance spectrum of the WO_3 NF powder within UV and visible ranges. The Tauc plot for the direct band-gap calculation is shown in the inset. Energy gap Eg = 2.68 eV is inferred. Figure reprinted from [90].

method (inset of **Fig. 3.4**) through **eq. 2.6** for direct bandgap (n=2) [90]. The calculated bandgap energy was 2.68 eV, in good agreement with the literature for monoclinic WO_3 [114–116].
The chemical composition of the powder at the surface was investigated by XPS. The wide scan spectra (**Fig. 3.5 a**) confirmed the presence of tungsten and oxygen. Traces of C belonged to the carbon tape used to hold the powders [117]. The binding energy values of W 4f and O 1s peaks are shown in **Fig. 3.5 b** and **c**, respectively. The W 4f core-level spectrum was fitted with two peaks centered at 35.6 and 37.7 eV and assigned to state $4f_{7/2}$ and $4f_{5/2}$ of W. The position and shape of these peaks are representative of W atoms with oxidation state of +6, as expected for stoichiometric WO_3 [118,119]. The fitting of the high-resolution scan of O 1s core level highlighted the presence of an intense peak at 530.5 eV, which is assigned to the typical W–O bond, and an extra peak at 531.7 eV, ascribed to the O–C bond probably due to carbon tape. Peaks attributed to reduced O–W were not distinguished, therefore the concentration of oxygen vacancies laid below the detection limit of the apparatus (0.1%) [120,121].

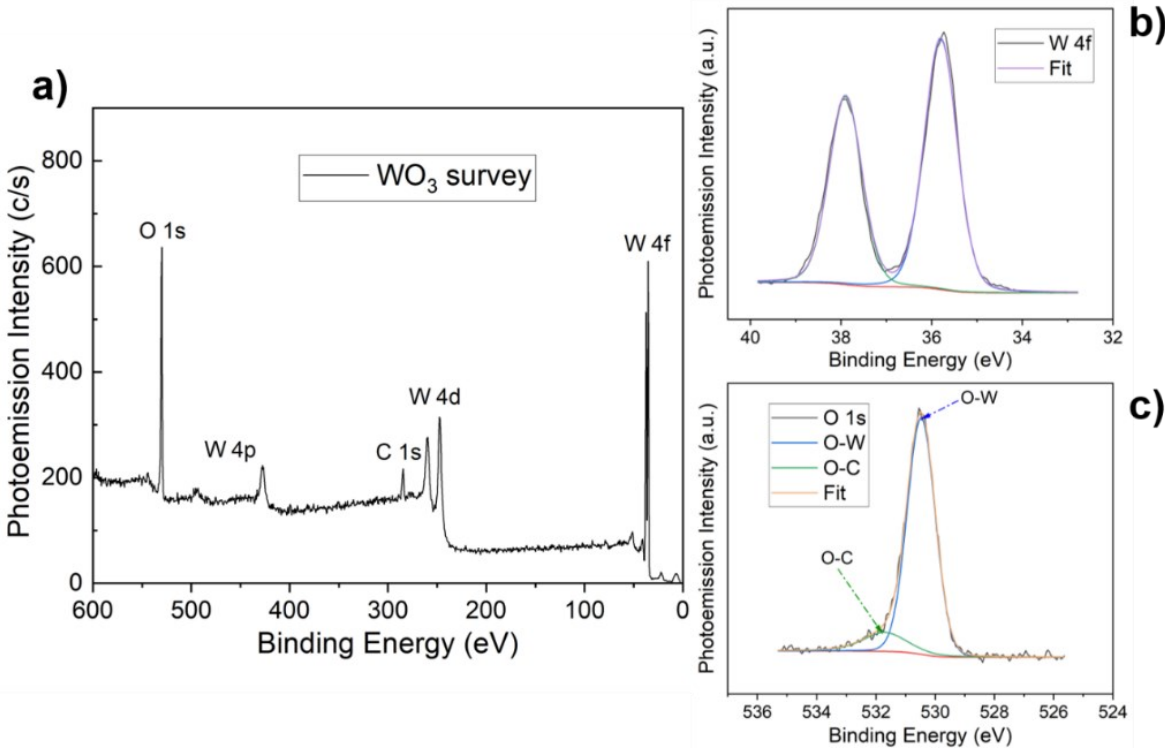

Fig. 3.5 XPS analysis of the WO_3 powder. **a)** The wide scan spectra with elements identification. **b)** The high-resolution scan of the W 4f core level (black line) and the curve fitting (purple line). The two fitted peaks at 35.6 eV and 37.7 eV were assigned to W^{6+} states $4f_{7/2}$ and $4f_{5/2}$, respectively. **c)** The high-resolution scan of the O 1s core level (black line) and the curve fitting (yellow line). The peak at 530.5 eV was assigned to O–W bonds, while that at 531.7 eV to O–C bonds. Figure reprinted from [90].

3.1.2 $(Sn,Ti,Nb)_xO_2$

SEM was used to examine the powder morphologies. The samples were all made up of spheroidal nanograins. **Fig. 3.6** depicts the particle-size distribution of powders with Nb concentrations of 1.5, 3.5 and 5% and calcination temperatures of 650 and 850 °C.

STN1.5_650 particle sizes varied within 10-20 nm, but STN5_650 had a wider distribution ranging within 5-60 nm. Similarly to STN1.5_650, the STN3.5_650 powder was mainly composed (80%) of particles with a diameter ranging within 5–15 nm, although a tail up to 65 nm was observed. The relative amount of Sn, Ti, and Nb played a critical role in particle development in solution since a higher concentration of Nb^{5+} resulted in a wider dispersion of the particle size distribution [29]. Simultaneously, a larger concentration of Nb^{5+} prevented grain coalescence at high temperatures. Indeed, the distribution of particle diameters remained nearly unchanged in STN5_850 compared to STN5_650. In contrast, the average particle size grew from 15.8 nm at 650 °C to around 27.8 nm at 850 °C for the STN1.5 samples and from 15 nm at 650 °C to around 28 nm at 850°C for the STN3.5 samples.

The influence of operation temperature on long-term recrystallisation of nanograins was also evaluated because the sensors ran at high temperatures. The powder SEM images were compared to those of the sensitive film of the sensors which were produced from the same powders and used for electrical characterizations at 400-450 °C for several months. Recrystallisation did not occur for any of the sensors studied, namely STN1.5_650, STN1.5_850, STN5_650, and STN5_850, as shown in **Fig. 3.7**.

To further investigate the influence of temperature on sample morphology, the adsorption and desorption isotherms of representative samples were measured and displayed in **Fig. 3.8**. The

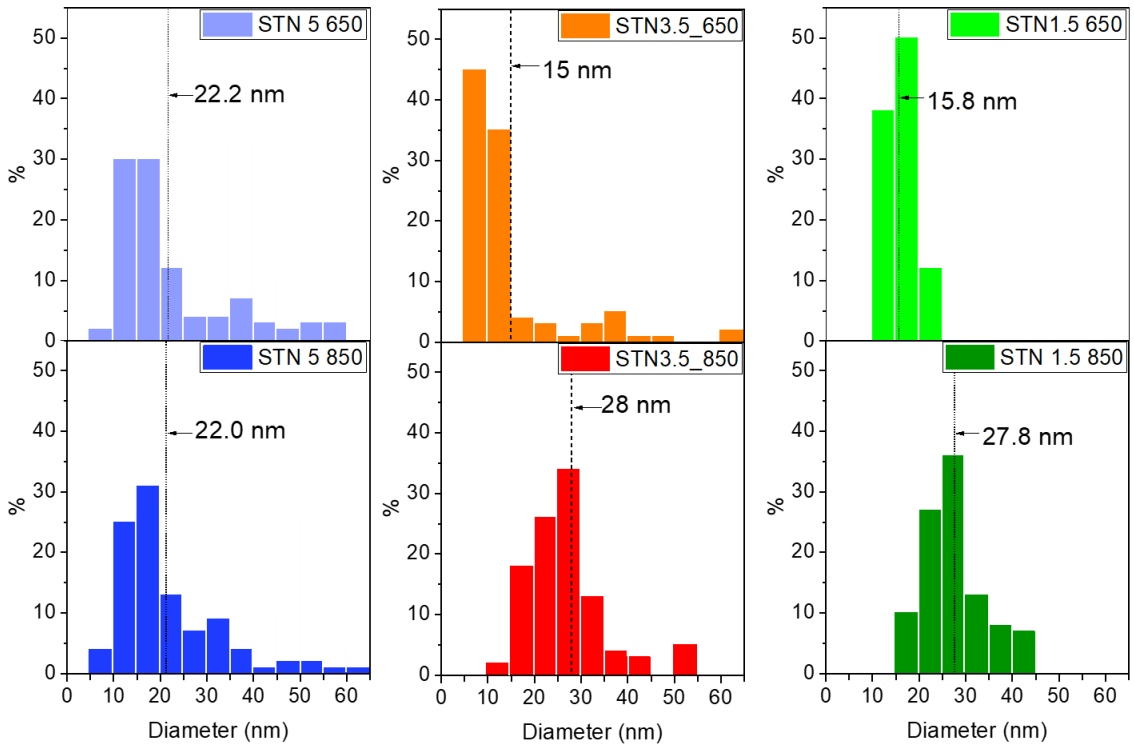

Fig. 3.6 Distribution of particles diameters (nm) in STN samples, revealing the influence of annealing temperature on grain coalescence. Black dot lines indicate the mean value of the distributions. Figure reprinted from [12,29] *.

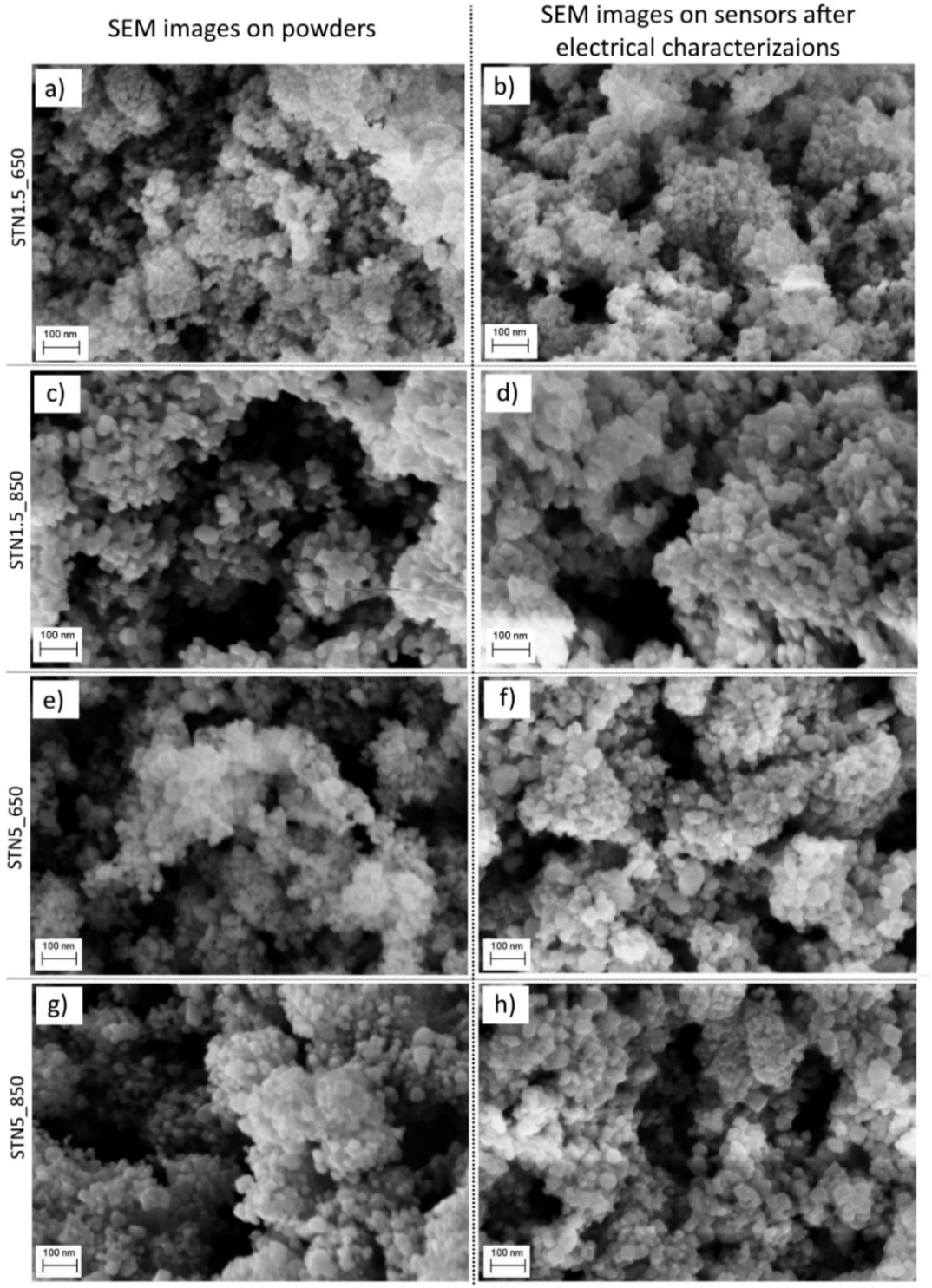

Fig. 3.7 SEM images of a) STN1.5 650, c) STN1.5 850, e) STN5 650, and g) STN5 850 powders highlighting the nanostructures' spheroidal form. SEM photos of the sensors' sensitive films b) STN1.5 650, d) STN1.5 850, f) STN5 650, and h) STN5 850 employed for electrical characterizations at high working temperatures, i.e. 400-450°C, over several months. The lack of grain coalescence is inferred by comparing the grain size of the powders and the sensitive films. Figure reprinted from [12,29].

corresponding N_2-Brunauer−Emmett−Teller (BET) surface area and the average pore size diameters are reported in **Table 3.2**. The average pore diameter and BET specific surface area of the powders treated at 650°C with and without Nb were comparable. While adding Nb to the

Table 3.2 BET specific surface areas and average pore diameter of representative solid solution powders, evidencing differences especially between the samples treated at 650 °C and that at 850 °C.

Sample	Specific Surface Area by BET method (m^2/g)	Pore size: D-H Desorption average pore diameter (4V/A) (nm)
ST30 650	50.4241	12.6562
STN 1.5 650	43.7231	16.7118
STN 5 650	48.3593	12.5190
STN 1.5 850	22.6258	23.9536

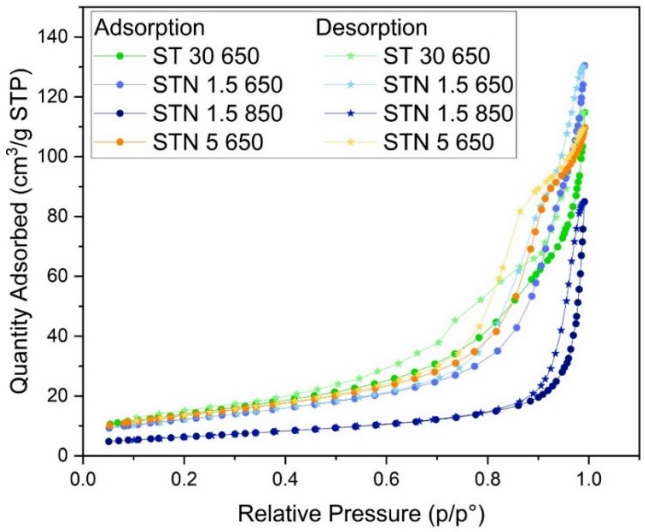

Fig. 3.8 N_2 isotherm profile of samples ST30_650, STN1.5_650, STN1.5_850 and STN5_650. Figure reprinted from [29] *.

Ti and Sn solid solution had no effect on the porous structure, heating the powder with 1.5% Nb at 850 °C reduced its BET specific surface area by half when compared to its counterpart heated at 650 °C. Moreover, the sample heated at 850 °C showed an average pore diameter remarkably higher than that of STN1.5_650. However, all samples were mesoporous, i.e., containing pores with diameters between 2 and 50 nm [18].

Fig. 3.9 a presents XRPD patterns collected at RT in the 2θ angular range of 20−60°.

Peak positions for ST30_650 and ST30_850 were shifted toward higher 2θ angles compared to those for STN samples, as a result of a smaller lattice. XRD analysis revealed that in all the investigated samples the main phase (ranging from 96.9 to 99.0 wt %, see **Table 3.3**) was a tetragonal rutile-type phase (space group, s.g. $P4_2/mnm$). Moreover, a tetragonal anatase-type phase (s.g. $I4_1/amd$) was also detected as

Table 3.3 Quantitative phase analysis and Rutile-type unit-cell parameters and crystal-size with their standard deviations for the STN samples collected at *RT*. The R-weighted pattern refinement agreement factors were $R_{WP\ (ST30\_650)}$ =0.094, $R_{WP\ (ST30\_850)}$ =0.097, $R_{WP\ (STN5\_650)}$ =0.117, $R_{WP\ (STN5\_850)}$ =0.118, $R_{WP\ (STN3.5\_650)}$ =0.129, $R_{WP\ (STN3.5\_850)}$ =0.117, $R_{WP\ (STN1.5\_650)}$ =0.110, and $R_{WP\ (STN1.5\_850)}$ =0.112, indicating the good quality of the fit [12,29] *.

	Quantitative phase analysis	*Rutile-type phase: unit-cell parameters*		
Sample	**rutile-/anatase-type wt%**	***a* (nm)**	***c* (nm)**	***V*(nm³)**
ST30_650	99.1(2)/0.9(2)	0.47040(3)	0.31488(3)	0.06968(1)
ST30_850	100/0	0.47041 (4)	0.31389 (3)	0.06946(1)
STN5_650	97.3(3)/2.7(3)	0.47070(3)	0.31460(3)	0.07044(1)
STN5_850	97.1(3)/2.9(3)	0.47190(3)	0.31619(3)	0.07014(1)
STN3.5_650	95.4(4)/4.6(4)	0.47133(4)	0.31565(5)	0.07012(1)
STN3.5_850	97.4(2)/2.6(2)	0.47116(3)	0.31484(4)	0.06989(1)
STN1.5_650	97.3(3)/2.7(3)	0.47077(3)	0.31463(4)	0.06973(1)
STN1.5_850	99.0(2)/1.0(2)	0.47148(2)	0.31576(3)	0.06973(1)

the remaining fraction. The main rutile-type phase along with the associated anatase phase (starting structure model from Hirata [84] and Howard et al. [122], respectively) were modelled by carrying out a multiphase Rietveld refinement, in which only the scale factors and unit-cell parameters were varied [29].

The unit-cell volume of the anatase-type phase was close to that of pure TiO_2 anatase reported in the literature, namely 0.1399 vs. 0.1362 nm^3 [122], respectively. The unit-cell parameters of the rutile-type phase are shown in **Table 3.3** and revealed that Nb and Ti both substituted for Sn at octahedral site to form the $(Sn,Ti,Nb)_xO_2$ solid solution. Indeed, by comparing in **Fig. 3.9 b** the unit-cell volume of SnO_2 (0.0716 nm^3 [123]) and TiO_2 (0.0624 nm^3 [122]) end-terms with those for the investigated samples, where $0.0695<V<0.0704$ nm^3, it can be deduced that the smaller $^{[6]}Ti^{4+}$ (ionic radius, i.r. = 0.605 [124]) and $^{[6]}Nb^{5+}$ (i.r. = 0.640 Å [124]) replaced

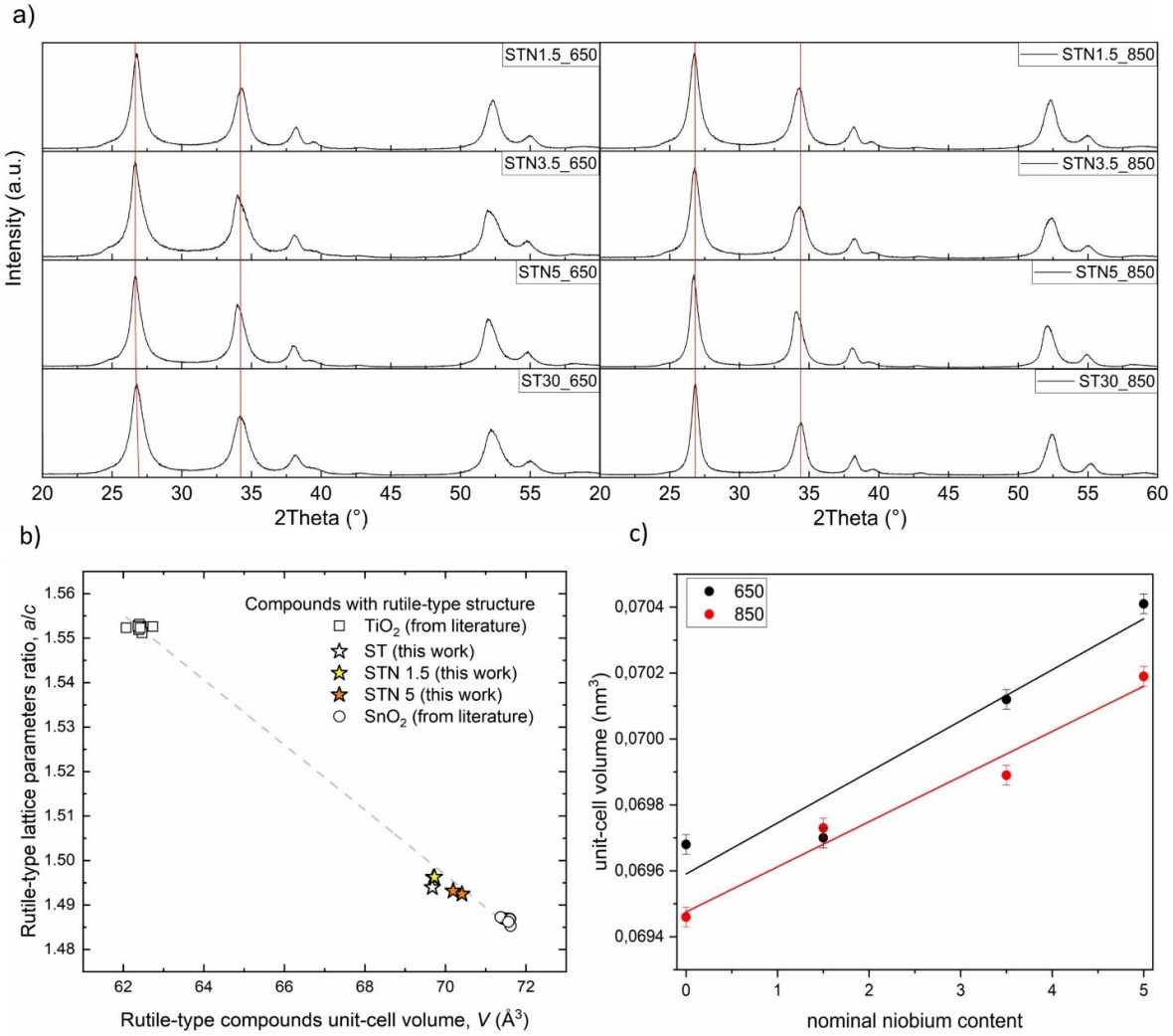

Fig. 3.9 a) X-ray powder diffraction patterns collected at RT on a Bruker D8 Advance Da Vinci diffractometer working in Bragg-Brentano geometry and equipped with a LynxEye XE silicon strip set to discriminate Cu $K\alpha_{1,2}$ radiation. Red lines parallel to the y-axis mark peak positions for ST30 to highlight the STN peaks shift [12]. **b)** Lattice parameters ratio (*a*/*c*) as a function of the unit-cell volume *V* for compounds having the rutile-type crystal structure along the TiO_2-SnO_2 join. Open squares and circles refer to data of TiO_2 rutile and SnO_2 cassiterite phases, respectively [122,215,224,225,216–223], while yellow stars refer to data of STN and ST30 samples investigated in this work [29]. **c)** Unit-cell dependence on both Nb content and calcination temperature. Figure reprinted from [12,29] *.

Table 3.4 Compositional proportion (%) of Sn, Ti and Nb in STN samples, obtained through EDX and XPS analyses. Table reprinted from [12,29] *.

EDX	STN1.5_650	STN3.5_650	STN5_650	STN1.5_850	STN3.5_850	STN5_850
Ti	22.0	25.0	22.7	26.7	23.5	21.2
Nb	1.7	4.9	5.3	1.4	4.1	5.0
Sn	76.3	70.1	72.0	71.9	72.4	73.8

XPS	STN1.5_650	STN3.5_650	STN5_650	STN1.5_850	STN3.5_850	STN5_850
Ti	29.3	31.0	30.2	29.4	26.6	25.2
Nb	3.8	10.9	9.8	3.4	14.9	12.4
Sn	66.9	58.1	60.0	67.2	58.5	62.4

approximately 17% of the bigger $^{[6]}Sn^{4+}$ (i.r. = 0.690 Å [124]), resulting in a unit-cell volume decrease. Moreover, the increase in the calcination temperature promoted the Ti for Sn substitution at the octahedral site of the SnO_2 structure. In fact, sample ST30_850 had a smaller unit-cell volume than that calcined at 650 °C (**Fig. 3.9 c**). Additionally, the increase in the nominal niobium content produced a unit-cell volume expansion in both samples treated at 650 and 850 °C, indicating that $^{[6]}Nb^{5+}$ preferentially replaced the smaller $^{[6]}Ti^{4+}$ into the oxide structure [29].

The composition of STN in the bulk and at the surface was estimated using EDX and XPS analyses (see **Table 3.4**).

The Sn/Ti/Nb atomic proportion obtained through EDX was slightly different from the synthesis starting stoichiometry, and a relative deficiency of Ti was observed. The existence of a minor amount of nano-anatase phase, primarily constituted of TiO_2, was found by XRPD phase analysis. EDX compositional analysis (**Fig. 3.10 a**) collected along profile traced on HAADF-STEM images (**Fig. 3.10 b**) also evidenced a small TiO_2 particle superimposed on a larger STN grain in the range of positions 40–60 nm. Such small nanoparticles can be partly lost during the supernatant filtration and powder washing, explaining the relative deficiency of Ti in the final samples compared to that in the batch of synthesis [29].

The proportion of Sn, Ti, and Nb determined by XPS analysis revealed higher Ti and Nb contents than those obtained by EDX analysis. This discrepancy can be explained by Ti and Nb

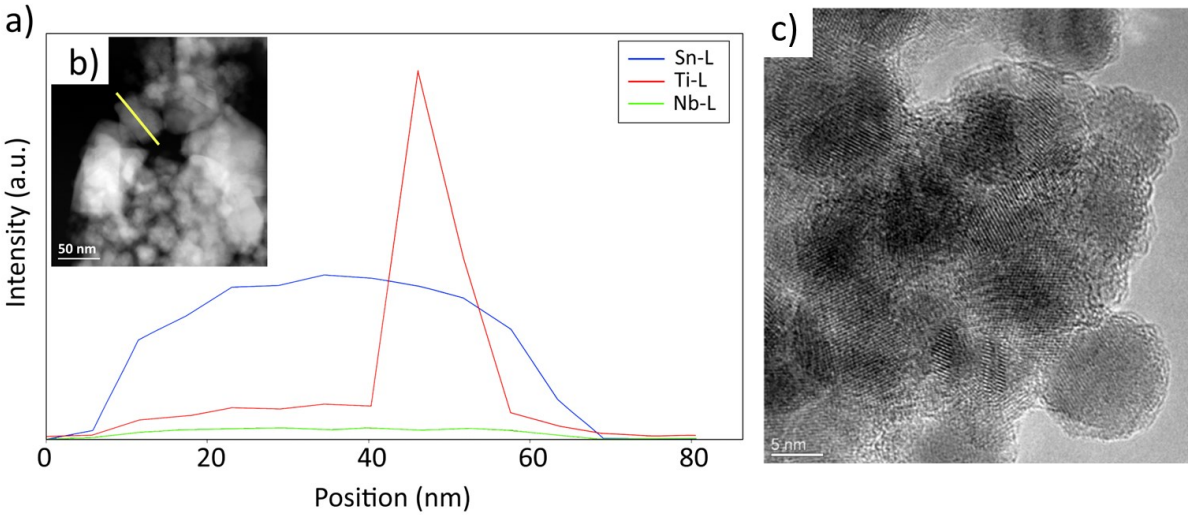

Fig. 3.10 a) EDX profiles collected on the yellow line of STN1.5_850 particles shown in the inset. **b)** HAADF-STEM image [12]. HREM image of sample STN3.5_650, highlighting that STN nanoparticles are surrounded by a thin (≈ 1 nm) amorphous layer. Figures reprinted from [12].

being partially segregated on the surface of STN nanograins, generating a thin layer of 1 nm, as shown in the High-Resolution Transmission Electron Microscopy (HREM) image in **Fig. 3.10 c** for STN3.5_650 sample. Moreover, Ti content was higher in STN3.5 and 5_650 while the Nb content was higher in STN3.5 and 5_850 samples, indicating that the different heat treatment favoured Ti rather than Nb surface segregation. A similar behavior was observed in the synthesis of other SMOX solid solutions and perovskites, where the driving force for surface segregation was a difference in cation mobility under an applied gradient, as well as a lower surface energy of the component that segregated at the surface [125,126].

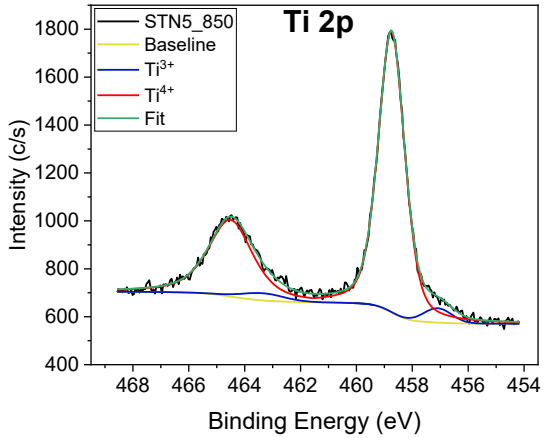

Fig. 3.11 Fits of the high-resolution scans of Ti 2p core levels for STN5_850, highlighting the presence of Ti^{3+}. Figure reprinted from [29] *.

Despite the scarcity of investigations on Sn, Ti, and Nb ternary solutions, it is known that the substitution of a tetravalent cation (M^{4+}) by a higher-valence cation, e.g. pentavalent Nb^{5+}, creates either M^{3+} or cation vacancies, or both [29,127,128]. XPS high-resolution spectra investigated the oxidation state of Sn, Ti and Nb inside the solid solution. The Sn 3d and Nb 3d regions showed peaks located at binding energies Sn $3d_{3/2}$ = 594.9 eV, Sn $3d_{5/2}$ = 486.5 eV and Nb $3d_{3/2}$ = 207.1 eV, Nb $3d_{5/2}$ = 209.7 eV, which are representative of Sn and Nb atoms with oxidation state of +4 and +5, respectively [129,130], as expected for stoichiometric SnO_2 and Nb_2O_5. The Ti 2p region showed peaks located at binding energy Ti $2p_{1/2}$ = 464.5 eV and Ti $2p_{3/2}$ = 458.7 eV, mostly attributed to the Ti^{4+} oxidation state [131], but also a shoulder due to a small content of Ti^{3+} (Ti $2p_{1/2}$ = 463.3 eV and Ti $2p_{3/2}$ = 457.0 eV) [131,132], see **Fig. 3.11**.

EPR measurements on STN and ST30 samples were carried out to reveal the presence of paramagnetic species, such as Ti^{3+}. The spectra in **Fig. 3.12 a** and **b** revealed the presence of one or, at most, two separate paramagnetic signals with g values systematically greater and lower than 2.0023, i.e. the g value for a free unpaired electron. By way of example, **Fig. 3.12 c** depicts the signals (labelled I and II) detected in the spectrum of STN5_650. **Table 3.5** collects the magnetic field values for EPR signals recorded in the spectra of samples ST30, STN1.5 and STN5 treated at 650 and 850 °C.

The line I was likely produced by superparamagnetic Fe(III) oxides, the resonant field of which can be observed at magnetic field values close to that of the free electron. The extreme sensitivity of the EPR technique allowed it to focus on Fe(III) superparamagnetic signals, even if this species can be considered negligible with most of the other investigation techniques [12]. The line II can be safely attributed to a transition metal ion with a number of electrons in the d shell lower than 5, which allowed the effective g value to be lower than the free electron value [12,133]. The g values were fully consistent with those of Ti(III) [12,133], in agreement also with the XPS high-resolution spectrum of the Ti 2p region carried out on the same samples. Ti(III) signal appeared only in Nb-bearing samples, while it was not detectable in the Nb-free materials. Therefore, Ti(III) defects can be addressed to charge compensation after substitution of tetravalent cations, i.e. Sn(IV) or Ti(IV), by pentavalent Nb(V).

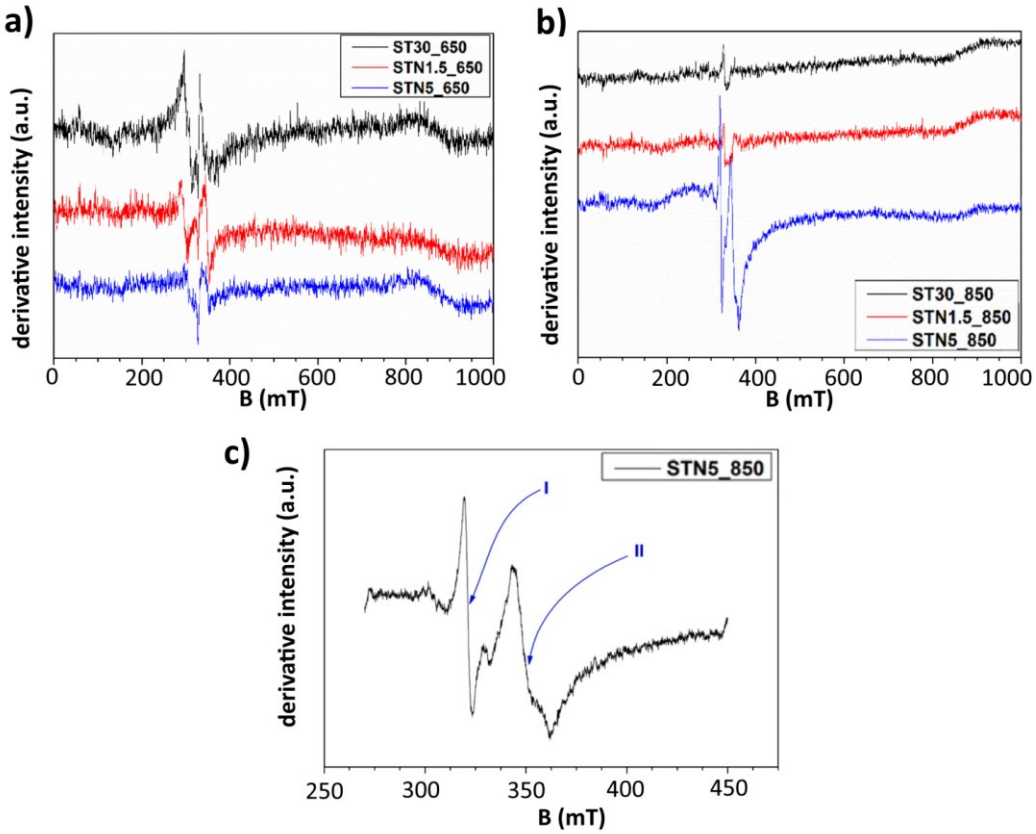

Fig. 3.12 Experimental spectra of **a)** samples treated at 650 °C and **b)** samples treated at 850 °C, showing the presence of one or, at most, two independent paramagnetic signals with g values systematically greater and lower than 2.0023 [12]. **c)** STN5_850 experimental EPR spectrum as an example of detailed scan, evidencing the two distinct signals at 321.3 and 350.8 mT. Magnetic field values in microtesla (mT). Figures reprinted from [12].

Table 3.5 EPR signals experimentally registered for ST30, STN1.5 and STN5 samples treated at 650 and 850°C. The line position is specified in mT for all signals. Under the experimental conditions, the free electron value (g=2.0023) occurs at 346.5 mT. Table reprinted from [12].

sample	**Line 1**		**Line 2 - Ti(III)**	
	B (mT)	***g***	***B (mT)***	***g***
ST30_650	309.6	2.241	-	-
STN1.5_650	295.1	2.351	348.4	1.991
STN5_650	304.4	2.279	351.0	1.977
ST30_850	-	-	-	-
STN1.5_850	325.7	2.130	349.2	1.987
STN5_850	321.3	2.159	350.8	1.978

The optical band gaps (E_g) were estimated using Tauc's plot method, as shown in **Fig. 3.13**. The band gap for ST30_650 was 3.65 eV and comparable to the values for solid solutions of $(Sn,Ti)_xO_2$ cited in [134]. However, the E_g obtained values for STN samples were lower than those found for ST30_650, and it became progressively narrower with increasing Nb concentration, experimentally demonstrating that Nb substitution in the solid solution's lattice favoured electronic band structure modifications. Indeed, the E_g decreased from 3.26 eV for STN1.5_650 to 2.92 eV for STN5_650 and from 3.20 eV for STN1.5_850 to 2.96 eV for STN5_850 [12]. Despite the absence of research on the band structures of the $(Sn,Ti,Nb)_xO_2$

three-component solid solutions, a decrease in the band gap of Nb-doped rutile TiO_2 has already been observed and described in [135,136].

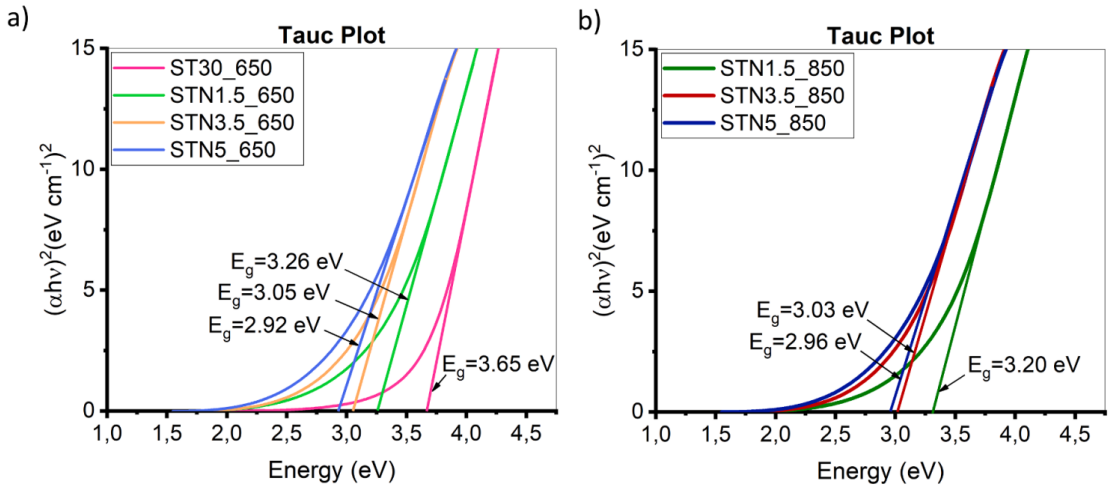

Fig 3.13 Tauc graphs demonstrating straight-line extrapolation to calculate the direct bandgap for **a)** ST30_650, STN_650, and **b)** STN_850 samples. The increase in Nb content decreased the E_g values). Figures reprinted from [12].

** "Reprinted with permission from [ACS Sens. 2022, 7, 573−583]. Copyright [2023] American Chemical Society."*

3.2 ELECTRICAL CHARACTERIZATION OF SMOX MATERIALS

3.2.1 WO_3-based film for ethanol detection

The conductance changes before and after injection of 5 ppm of ethanol at different working temperatures within 200–350 °C was measured to determine the optimal response of WO_3 NF-based film. The optimal operating temperature resulted to be 250 °C, as shown in **Fig. 3.14 a**. The "volcano" shape (increase-peak-decrease) relationship of the response with operating temperature is a common behaviour for SMOXs film [44,45,137] and has been previously explained in section 1.3.5.

The film conductance in dry air and under exposure to 5, 10, 25, and 50 ppm of ethanol is shown in **Fig. 3.14 b**. The value of film conductance in synthetic dry air, i.e. 3.1×10^{-7} S, was in agreement with those reported in the literature [138–140], despite a thicker sensing film used in this work. It means that WO_3 NF films have lower conductivity, which is consistent with the lack of oxygen vacancies found via XPS, which would otherwise enhance film conductivity. [90]. After injection of ethanol, the film conductance readily increased to 2.2×10^{-6} S at 5 ppm and keep increasing up to 6.7×10^{-6} S at 50 ppm, evidencing a suitable sensitivity of the film for the above-mentioned applications (section 1.1.4) within the concentration range of interest.

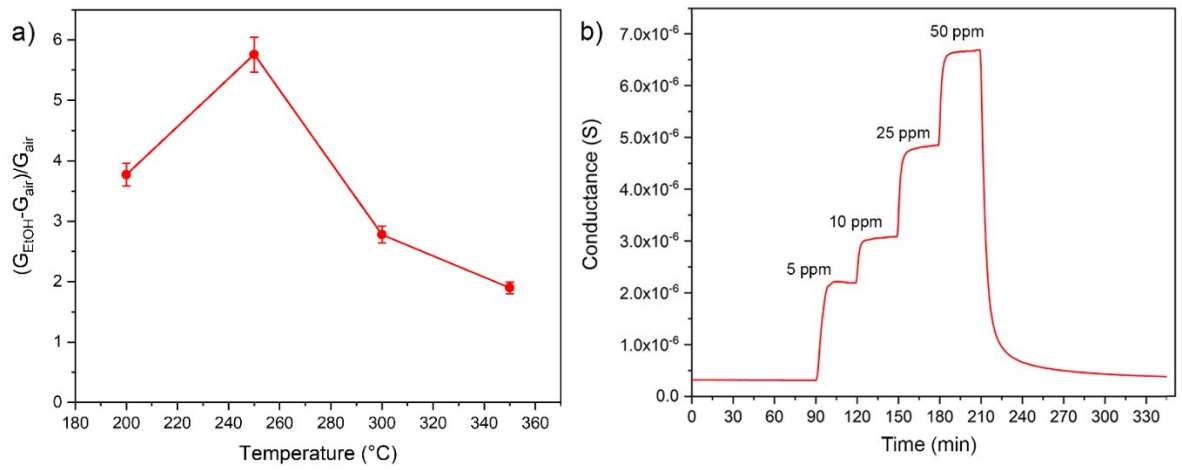

Fig. 3.14 Electrical properties of the WO_3 NF film. **a)** Response to 5 ppm of ethanol vs. temperature. **b)** Conductance vs. time when exposed to 5, 10, 25, and 50 ppm of ethanol. Figure reprinted from [90].

To investigate the stability of the film, it was kept at 250 °C under a flux of dry air and every two days it was exposed to 5 ppm of ethanol for two cycles of 30 min each. The measurements were carried out during a period of 14 days and the responses calculated at the second cycle vs. time are shown in **Fig. 3.15**. The response remained at approximately 5.7 with a mild increasing trend. In the inset of **Fig. 3.15** is exhibited the repeatability of the dynamical response by exposing the device to 5 ppm of ethanol in four cycles. The selectivity of WO_3 NF was thoroughly explored vs. potential interferents and especially vs. humidity. **Fig. 3.16** shows the sensor conductance in presence of ethanol and at different % of humidity. After a decrease from 2.3×10^{-6} S, in dry air, to 1.8×10^{-6} S, at 30 RH%, the film conductance kept rather constant until 70 RH%.

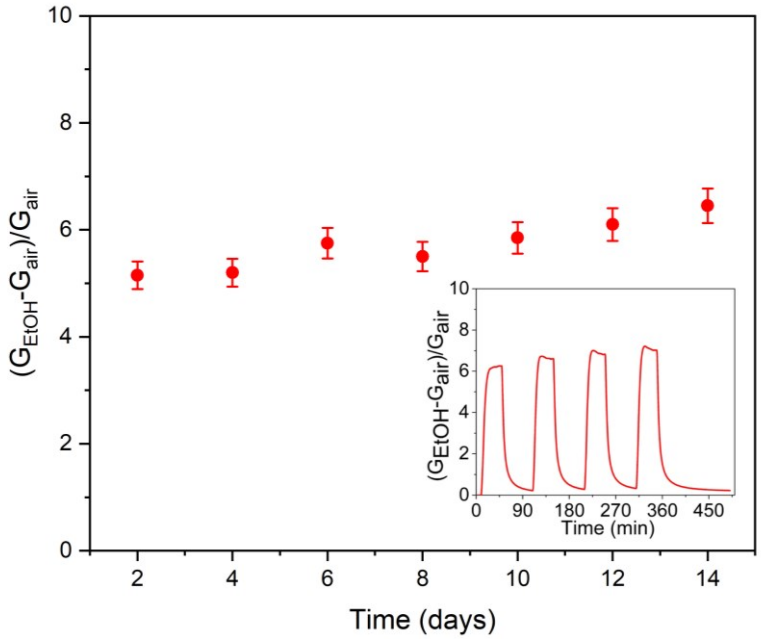

Fig. 3.15 WO_3 NF film response during 14 days. The 4-cycles repeatability test as a function of time is in the insert. For both experiments, an ethanol concentration of 5 ppm was chosen. Figure reprinted from [90].

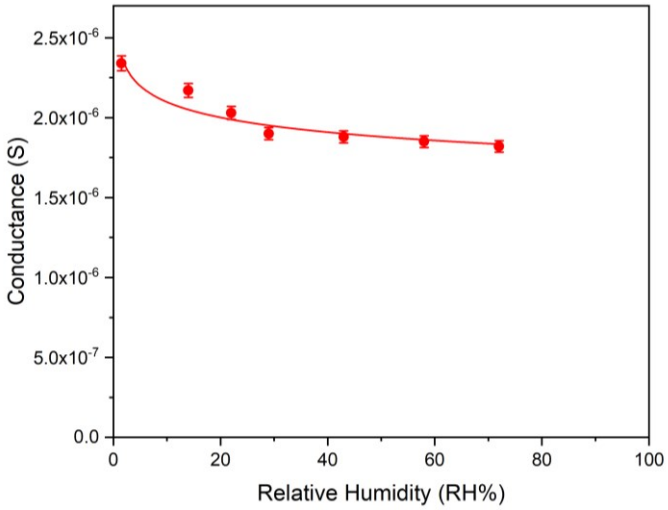

Fig. 3.16 Influence of humidity on the film conductance vs. 5 ppm ethanol. The temperature inside the chamber was 28.5 ◦C in the whole range of RH%. The line is drawn to guide the eye. Figure reprinted from [90].

The selectivity was further investigated by exposing the sensor to various gases, including, H_2, H_2S, NH_3, NO_2, CO, as well as different alcohols. The analytes were selected based on their potential presence in the gaseous environments under which ethanol sensors are required to function, such as ammonia, nitrogen monoxide, and hydrogen sulfide for the detection of alcohol in human breath [61] and hydrogen and carbon monoxide for the reaction monitoring of ethanol steam reforming reactors in the production of hydrogen [141]. The concentrations of the selected gases were chosen below their respective threshold limit values (TLV) [142] at the level reported in the literature for ease of comparison, i.e. 50 ppm of H_2 (no specific exposure limits), 10 ppm of H_2S (TLV = 10 ppm), 2 ppm of NH_3 (TLV = 25 ppm), 0.5 ppm of NO_2 (TLV = 3 ppm), 25 ppm of CO (TLV = 25 ppm), and 10 ppm of different alcohols, i.e. CH_3OH (TLV = 200 ppm), C_2H_5OH (TLV = 1000 ppm) and C_4H_9OH (TLV = 20 ppm). The responses, R, displayed in the radar plot (**Fig. 3.17**) and defined as in **eq. 2.12** and **2.13**, reveal that the film

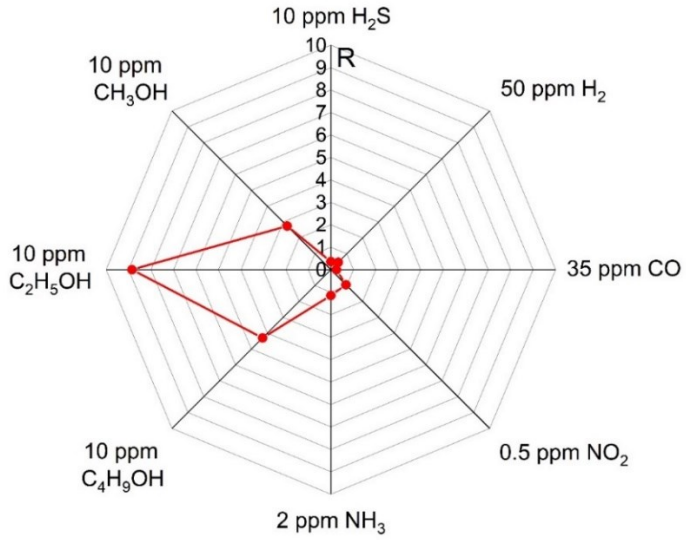

Fig. 3.17 Radar plot of WO_3 NF sensor responses (see Eq. 2.12 and 2.13) to potential interferents in applications of ethanol detection (see text) at 250 °C working temperature. Figure reprinted from [90].

was more reactive to ethanol than to the other gases. In general, a large concentration of surface oxygen vacancies can be used to explain a film's high reactivity to oxidizing gases, such as NO_2 [140,143,144]. In our situation, the low response to NO_2 could be explained by the absence of oxygen vacancies at the surface, as shown by XPS (**Fig. 3.5**).

Although not directly related to any specific applications, insights on the reaction mechanism of the WO_3 NF film may be driven by evaluating the response vs. other simple alcohols such as methanol and butanol at the same concentration as ethanol. According to **Fig. 3.17**, the response to 10 ppm was higher for ethanol than for the other alcohols. **Fig. 3.18** presents the calibration curves for all the alcohols under consideration, with ethanol performing best. Calibration curves were fitted with a power law function $R = ax^b$ where R represents the sensor response and x represents the gas concentration**.** A closer inspection into the dynamic response of the film to 5 ppm of gas (**Fig. 3.19**) reveals various kinetics, where dynamic responses vary depending on the type of alcohol present. Most notably, the dynamic responses to methanol and ethanol differed greatly in shape because the former abruptly peaked in the initial stage and subsequently stabilized, whilst the latter smoothly achieved saturation. The response times of ethanol (9 min 40 s) and methanol (6 min 30 s) were comparable while butanol showed a much slower kinetics. The recovery times for the three alcohols were comparable, with ethanol being slightly faster (21 min).

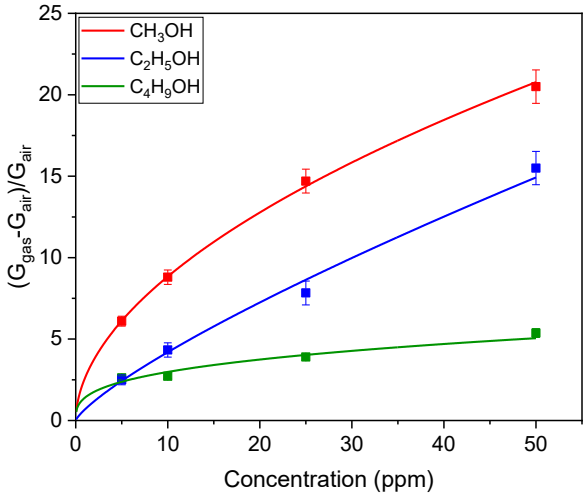

Fig. 3.18 Calibration curves of WO_3 NF film for methanol (green), ethanol (red) and butanol (blue). Data agree with a power law function with parameters a = (1.31 ± 0.24), b = (0.35 ± 0.05) for methanol, a = (2.68 ± 0.14), b = (0.52 ± 0.01) for ethanol and a = (0.57 ± 0.15), b = (0.84 ± 0.07) for butanol. Figure reprinted from [90].

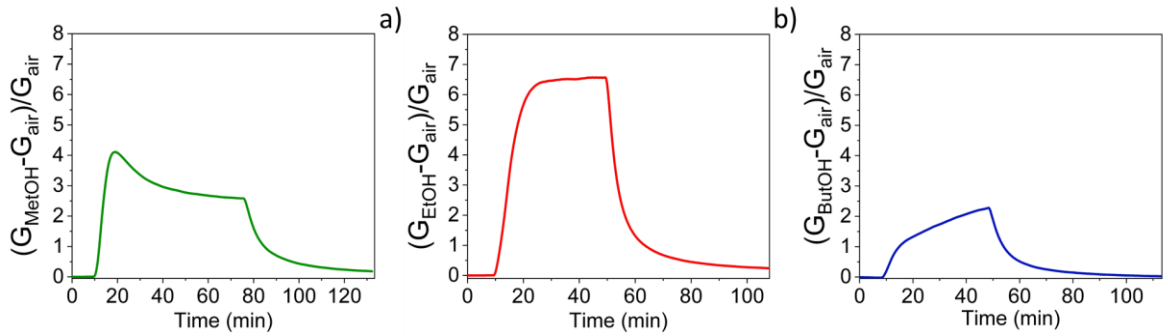

Fig. 3.19 The WO_3 NF film's dynamic response to 5 ppm of **a)** methanol, **b)** ethanol and **c)** butanol. Different kinetics are shown in the figures, with longer response times for longer alcohol chains. Figure reprinted from [90].

3.2.2 $(Sn,Ti,Nb)_xO_2$, $(Sn,Ti)_xO_2$, SnO_2-based film for hydrogen and ethanol detection

The effect of Nb addition on the film conductance of the solid solution vs. temperature is shown in **Fig. 3.20 a**, which displays the Arrhenius plot in synthetic air obtained by changing the temperature from 350 K up to 900 K at the heating rate of 6 K/min.
The conductance of all films increased with temperature because it increased the number of free electrons thermally excited from ionizable levels under the conduction band [29]. Additionally, STN films were more conductive than ST30_650 and the 3.5at% and 5at% Nb content resulted in the highest conductance of the films annealed at 650 °C. The increased conductance of STN films is explained by the substitution of Nb in the lattice, which resulted in extrinsic substitutional doping by introducing additional carriers [86,145]. This effect may be counteracted by increasing the energy barriers ΔE, which would reduce the conductance of the solid solution. **Fig. 3.20 b** illustrates the ΔE calculated from the Arrhenius plot through the method reported in [146]. At 450°C, for example, ΔE = 0.9 eV for STN1.5_650, STN3.5_650 and STN 5 650, whereas ΔE = 0.5 eV for ST30_650. Although the role of ΔE on film conductance could not be quantified, its change was a clear indication of bulk- and surface-defect modifications caused by the addition of Nb. On the other hand, annealing temperature of 850 °C resulted in a lower conductance of STN films with the respect to their counterpart treated at 650 °C. Even though annealing would provide the necessary mobility for Ti and Nb to enter the SnO_2 lattice, it can also induce their segregation because the excess of stress in the lattice is not thermodynamically supported [147,148]. This self-purification process would reduce the content of Nb^{5+}, lowering conductance. The energy barriers of STN1.5_850, STN3.5_850 and STN5_850 were lower than those of their annealed counterparts at 650 °C, i.e. E = 0.7 eV at 450 °C, indicating that annealing altered both bulk and surface properties.
Preliminary measurements on the sensors composed of STN nanostructures have revealed that the films varied considerably their conductance in the presence of hydrogen and ethanol. For this reason, numerous tests have been carried out to find the optimal conditions for STN sensor

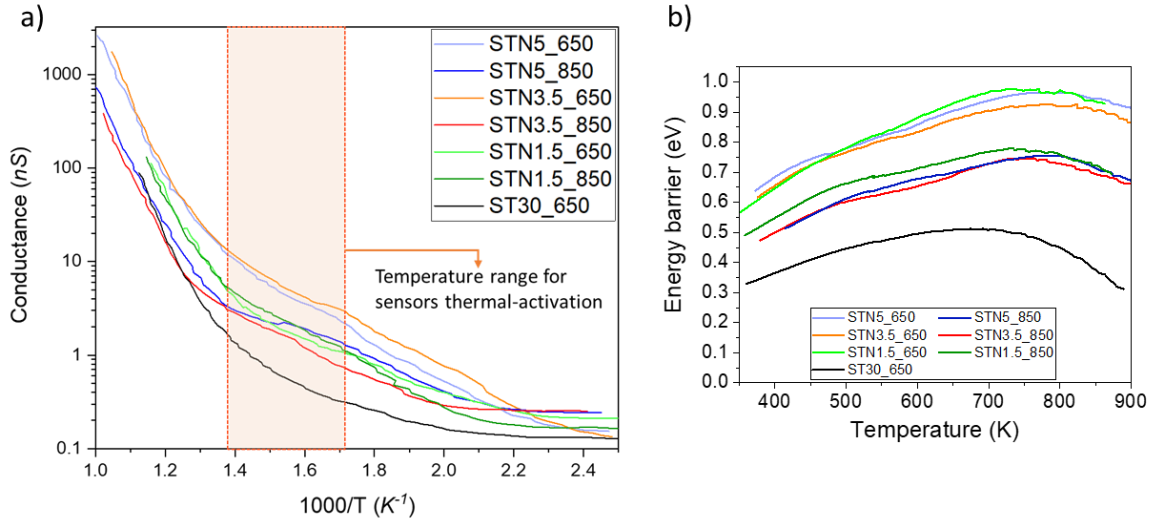

Fig. 3.20 a) Films conductance vs. temperature in dry air, showing that Nb increased the film conductance of the solid solution of Sn and Ti (ST30_650), especially in the temperature range for sensor thermal activation. **b)** Energy barrier dependence on temperature in dry air. The method used for the energy barrier measurements is reported in [146]. Figure reprinted from [29] *.

operation, i.e. operating temperature, as well as to investigate the sensitivity and selectivity to these two analytes.

The optimal response of STN films was determined by measuring the conductance change before and after injection of 50 ppm of H_2 and of 20 ppm of ethanol, at different working temperatures within 350-500 °C. The responses to H_2 in **Fig. 3.21 a** evidence two different trends. The operating temperature had a considerable impact on the response of STN sensors calcined at 650 °C. In fact, the response peaked at 450°C 2.5 times higher than at 400 °C and 500 °C. On the other hand, the responses of the STN sensors calcined at 850 °C moderately increased with working temperature. The ethanol response, shown in **Fig. 3.21 b**, appears to be generally less influenced on operating temperature than the hydrogen one and the optimal condition ranged within 400 and 450 °C. In fact, the performance at 400 °C was slightly higher than at 450 °C, but as will be discussed in more detail later, the response at such operating temperatures was only slightly influenced by humidity, so full characterization of the STN sensors was carried out at 450 °C.

The optimal working temperature for SnO_2_650 and ST30, e.g. 400 °C and 450 °C, respectively, was previously estimated [29,89].

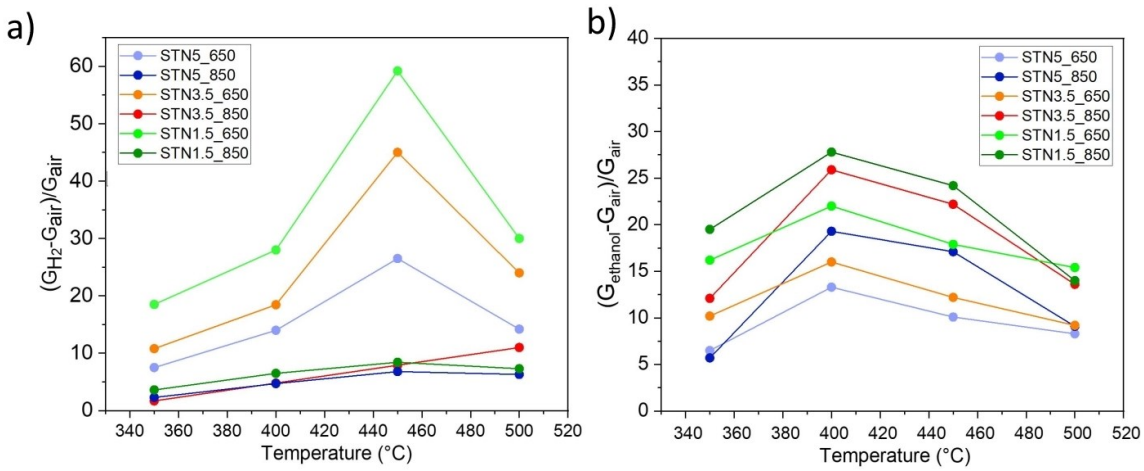

Fig 3.21 Response of STN films to **a)** 50 ppm of H_2 and **b)** 20 ppm of ethanol at different working temperatures, at which the STN 650 films reveal a greater dependence than the STN 850 ones, in particular for H_2 detection. Figure reprinted from [12,29] *.

The sensitivity to H_2 was investigated by exposing the sensors to 0.4, 1, 2, 10, 25, 50, 75 and 100 ppm. The dynamic response in **Fig. 3.22** highlighted that in all the concentration range the response of STN_650 films was higher than that of STN_850, with STN1.5_650 overperforming among the others. In **Fig. 3.23** the response level to concentration x in the range of 2-100 ppm were fitted with a power law function $R = ax^b$, R being the sensor response. STN1.5_650 exhibited a significant response even at the lowest concentration of H_2 injected in the chamber (R=5.55 at 0.4 ppm), implying a very low theoretical limit of detection. To better extrapolate sensor responses at lower concentrations and to determine the theoretical limit of detection (LOD) as in Ref. [149], a linear fit ($R = cx$) was used. The estimated theoretical LOD was 5 ppb, which is the lowest LOD obtained for SMOX gas sensors vs. H_2 to the best of our knowledge. Power law function parameters a and b and linear fit parameters c are listed in **Table 3.6**.

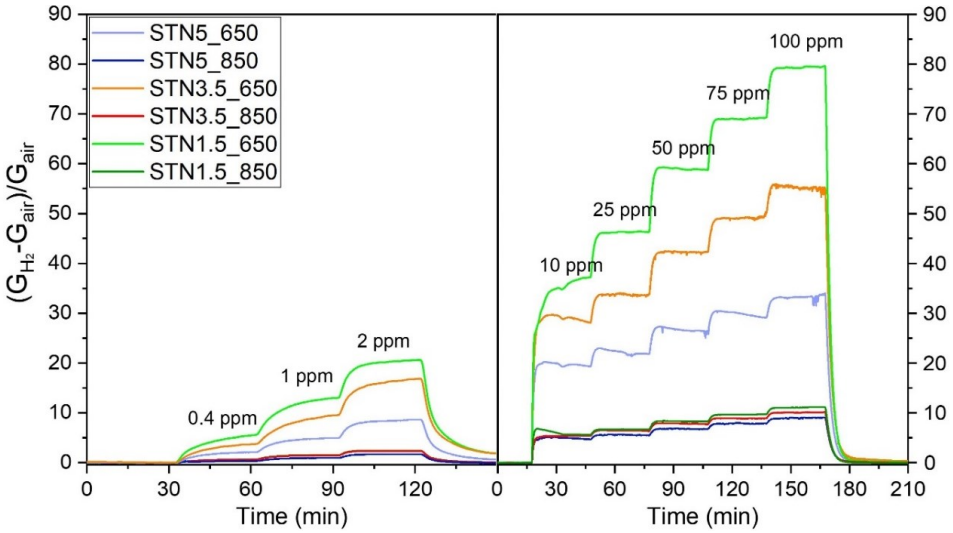

Fig. 3.22 STN film dynamical responses at 450°C to 0.4, 1, 2, 10, 25, 50, 75 and 100 ppm of H_2 in dry air, highlighting that the response of STN calcined at 650 °C is much higher than that of the counterpart treated at 850 °C. Figure reprinted from [29] *.

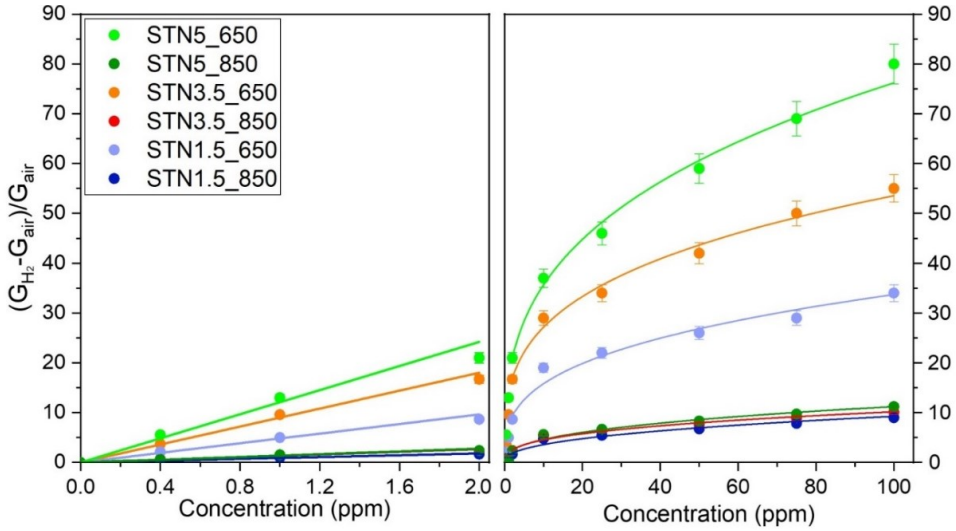

Fig. 3.23 STN calibration curves fitted with a power law function. The response level was taken from **Fig. 3.22**. A linear plot for concentrations lower than 2 ppm was used to estimate the theoretical LOD**.** Figure reprinted from [29] *.

Table 3.6. Function parameters for the calibration curves in **Fig. 3.23.** Power low function parameters a and b for the H_2 concentration range between 2 and 100 ppm and linear fit parameter c for H_2 concentration range between 0.4 and 2 ppm.

Model	Power law function					
Equation	$R = ax^b$					
Plot	**STN5_650**	**STN5_850**	**STN3.5_650**	**STN3.5_850**	**STN1.5_650**	**STN1.5_850**
a	7.42±0.74	1.39±0.20	13.77±0.68	2.02±0.19	16.67±0.72	1.91±0.19
b	0.33±0.03	0.41±0.04	0.295±0.014	0.35±0.03	0.330±0.013	0.38±0.03
Model	Liner fit					
Equation	$R = cx$					
c	4.82±0.31	0.91±0.05	9.01±0.38	1.35±0.13	12.10±1.05	1.38±0.12

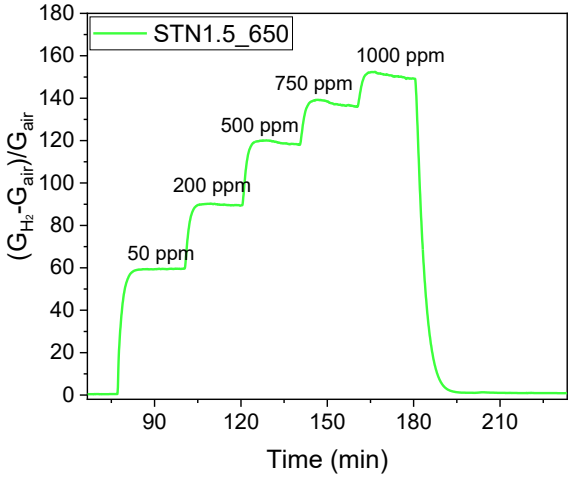

Fig 3.24 Response of the sensor STN1.5_650 to 50, 200, 500, 750 and 1000 ppm of H_2 as a function of time.

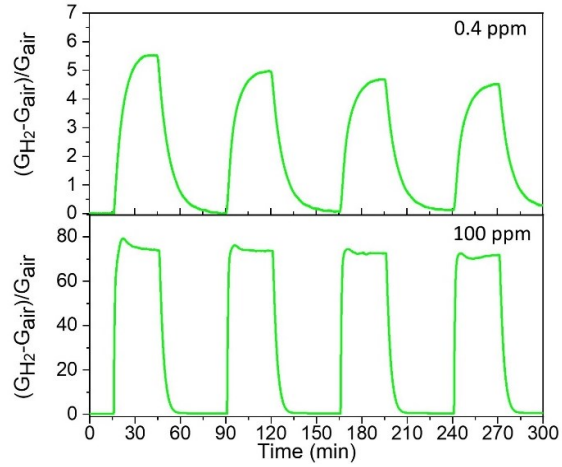

Fig 3.25 Response of the sensor STN1.5_650 to four-cycles injection of 0.4 and 100 ppm of H_2 as a function of time. Figure reprinted from [29]*.

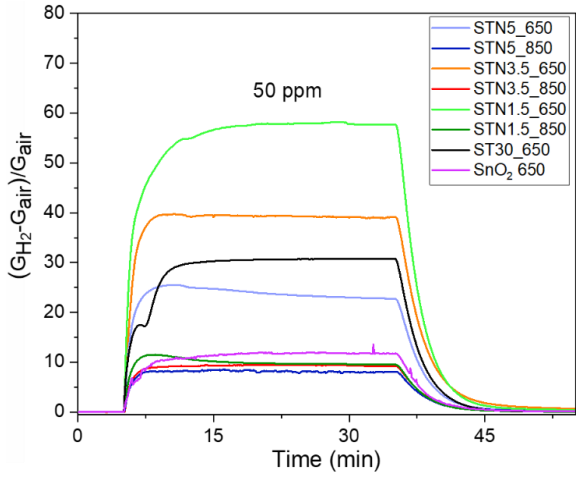

Fig. 3.26 Comparison between the responses of STN, ST30 650 and SnO_2 films to 50 ppm of H_2 (sensors performing at their optimal working temperature of 450 °C for STN and ST30_650 and 400 °C for SnO_2 650 [89]). [29]*.

For automotive and storage security applications, the sensitivity to a wider range of H_2 concentration up to 1000 ppm was investigated for the better performing sensor, i.e. the STN1.5_650. The sensor showed a good sensitivity also at high concentration of H_2 (**Fig. 3.24**). However, the response variation between 750 and 1000 ppm started to decrease, indicating that the sensor was likely saturating its active sites for H_2 detection. Therefore, STN1.5_650 should be used for H_2 concentration monitoring below 1000 ppm.

The repeatability of the dynamic response vs. H_2 was investigated for STN1.5_650. **Fig. 3.25 a** shows the dynamical responses in four cycles to 0.4 and 100 ppm of H_2, i.e. the concentrations extreme of the calibration curves (**Fig. 3.23**).

In **Fig. 3.26**, the response of STN films vs. 50 ppm H_2 was compared to that of SnO_2 650 and ST30_650 films. The response of pure SnO_2 was tripled when Ti was incorporated into the lattice. The Nb content of the solid solution and the calcination temperature both had a significant impact on the response. The response of the ST30_650 was increased with a Nb content of 3.5at% and, in particular, 1.5at%, which doubled it, while a Nb content of 5at% had the opposite effect. Furthermore, calcination at 850 °C severely suppressed the beneficial effect of Ti and Nb, resulting in films with a lower response than SnO_2 650.

The response and recovery times were calculated for 50 ppm from **Fig. 3.26**. Except for STN1.5_650, which had slower response and faster recovery kinetics (about 5 min 10 s and 5 min 50 s, respectively), all STN had similar response (about 2 min) and recovery (about 7 min) times. Response and recovery times of minutes have already been observed in previous works for traditional SnO_2 and other materials [90,117,150–152]. Response and recovery times were affected by the chamber's size and geometry, as well as the

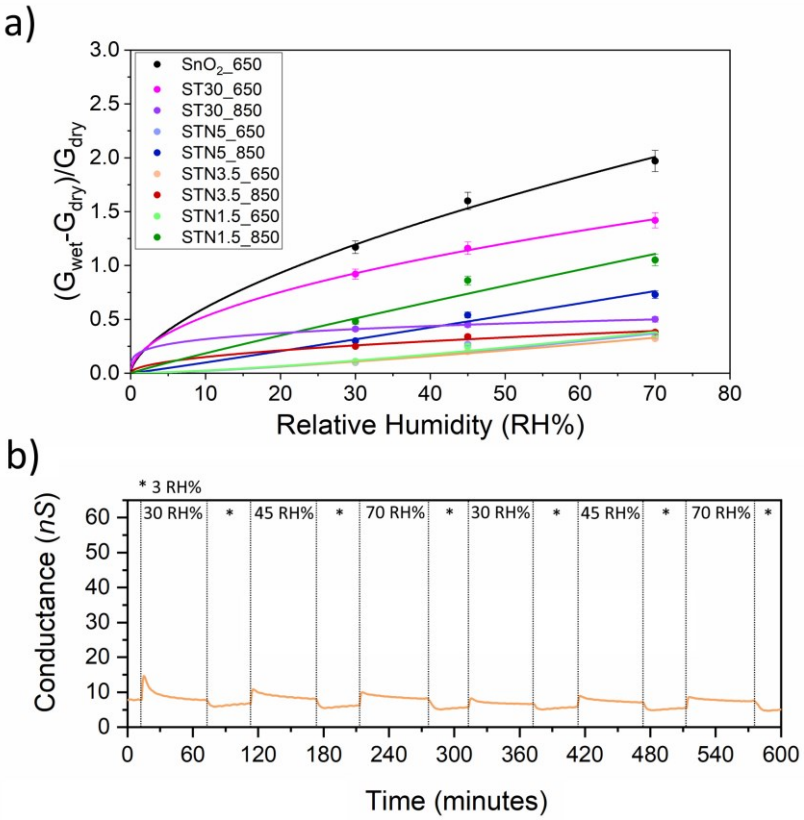

Fig. 3.27 a) Response of STN, ST30 and SnO_2_650 films to different RH% and **b)** influence of humidity on the conductance baseline of STN3.5_650. The temperature inside the chamber was 34 °C in the whole range of RH%. The operating temperature value was set at 400°C for SnO_2_650, and at 450 °C for ST30 and STN films. Figures reprinted from [12].

speed of the gas flow [151]. Because the chamber fills in about 1 minute 15 seconds, the response times of STN films should be rather fast.

The response level of the sensors to different relative humidity percentage (RH%) up to 70 RH% is shown in **Fig 3.27 a**. It highlighted that both Ti and Nb addition decreased SnO_2 film response to RH%. Moreover, STN treated at 650 °C achieved remarkable baseline stability, as shown in **Fig. 3.27 b** for STN3.5 650.

Commonly, a humid environment negatively impacts the response of SMOX-sensors because water molecules compete with the analyte for active surface sites. The effect of humidity on H_2 detection was investigated by injecting 50 ppm of H_2 into a gas chamber at various relative humidity ranging from 1.7% to 55% RH (see **Fig. 3.28**). Even though water vapor did not significantly change the sensor baselines, it did affect the sensor response vs. H_2 which decreased significantly up to 17 RH%. With increased RH%, the sensor signal to H_2 kept rather constant, with STN1.5_650 still sensing at high level. The response in **Fig 3.28 a** was estimated as in **eq. 2.12** considering $G_{baseline}$ equal to the conductance value reached at that specific RH%.

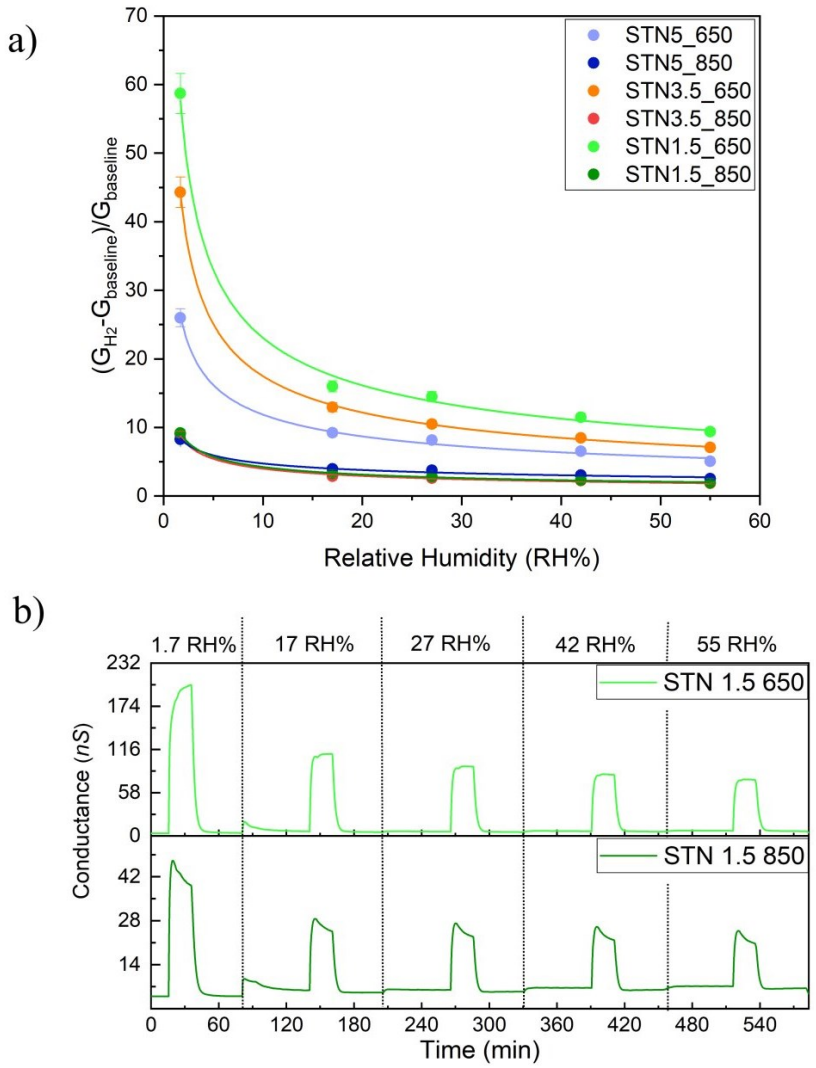

Fig. 3.28 a) Response of STN films to 50 ppm of hydrogen at 1.7, 17, 27, 42 and 55 RH% and **b)** conductance variation of STN3.5_650 after injection of 50 ppm of ethanol in different RH% conditions. The temperature inside the chamber was 29 °C in the whole range of RH%. Figures reprinted from [12].

The sensitivity was investigated also for ethanol by exposing STN films to 5, 10, 20, 35, 50, 75, and 100 ppm (dynamical responses are in **Fig. 3.29 a**. The samples calcined at 850 °C performed better than their counterparts treated at 650 °C. The response level decreased as the Nb content increased from 1.5 to 5. STN1.5_850 film overperformed among the others, reaching a response equal to 67 at 100 ppm. **Fig. 3.29 b** shows the calibration curves for all the sensors under study. Calibration curves were fitted with a power law function $R=ax^b$, a and b parameters are in **Table 3.7**.

Table 3.7. Power law function parameters for the calibration curves in **Fig. 3.29 b**. Figures reprinted from [12].

Model	Power law function					
Equation	$R=ax^b$					
Plot	**STN5_650**	**STN5_850**	**STN3.5_650**	**STN3.5_850**	**STN1.5_650**	**STN1.5_850**
a	2.64±0.11	4.37±0.56	2.41±0.07	4.21±0.08	2.95±0.16	3.62±0.11
b	0.45±0.01	0.47±0.04	0.55±0.01	0.55±0.01	0.60±0.02	0.63±0.01

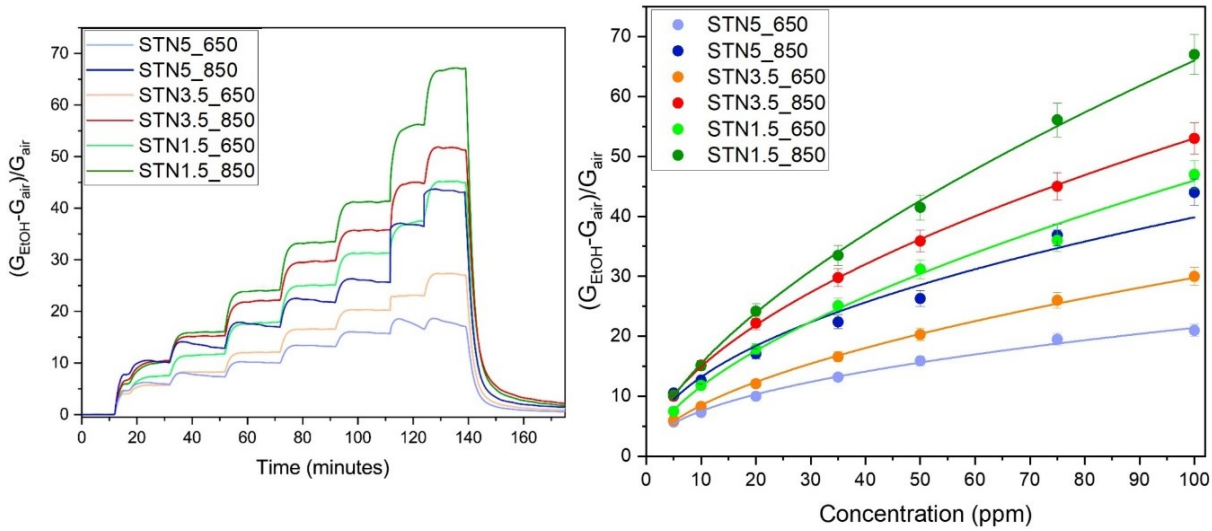

Fig. 3.29 a) STN sensors dynamical responses to 5, 10, 20, 35, 50, 75 and 100 ppm of ethanol in dry air and **b)** calibration curves. STN films performed at their optimal working temperature of 450 °C. Figures reprinted from [12].

Fig. 3.30 displays the repeatability of the dynamic response vs. 35 ppm of ethanol for STN1.5_650 and STN1.5_850, which were chosen as representatives of the two heat treatment groups because they responded better to ethanol than STN3.5 and STN5. Moreover, STN1.5_650 and STN1.5_850 had comparable mean response times calculated over four cycles, i.e. 3 min 40 s and 4 min 15 s, respectively. The mean recovery time for STN1.5_650 was slightly longer than for STN1.5_850, at 15 min 40 s and 13 min, respectively.

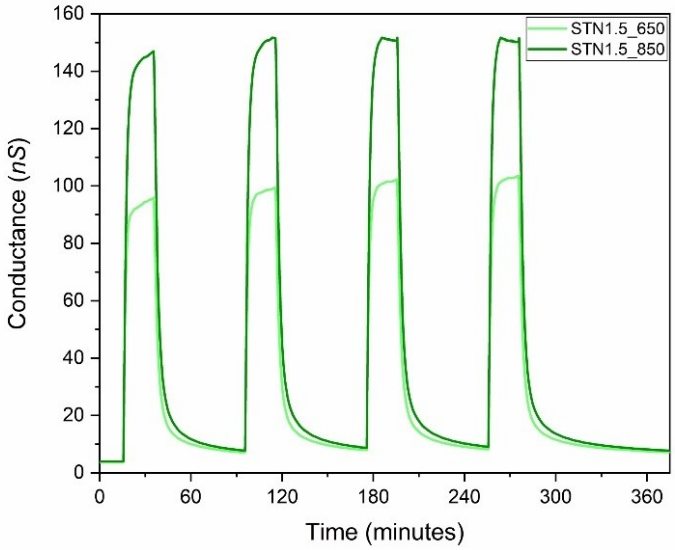

Fig. 3.30 Conductance variation of STN1.5_650 and STN1.5_850 during 4-cycles injection of 35 ppm of ethanol as a function of time. The sensors operating temperature value was set at 450°C. During the measurement, the temperature and humidity inside the chamber were 33°C and 1.7 RH%. Figures reprinted from [12].

The response levels of SnO_2_650 were compared to those of ST30 and STN films. Ti incorporation in the SnO_2 lattice more than doubled the response to 35 ppm of ethanol, as evidenced in **Fig. 3.31**. On the contrary, the addition of Nb had no noticeable effect on the performance of the films treated at 650 °C. The responses of STN3.5 650 and STN5 650 were, in fact, similar to those of ST30_650. Only STN1.5_650 response increased when compared to

ST30_650. Otherwise, the addition of Nb increased the response of all films treated at 850 °C, and STN1.5_850 doubled the response of ST30_850.

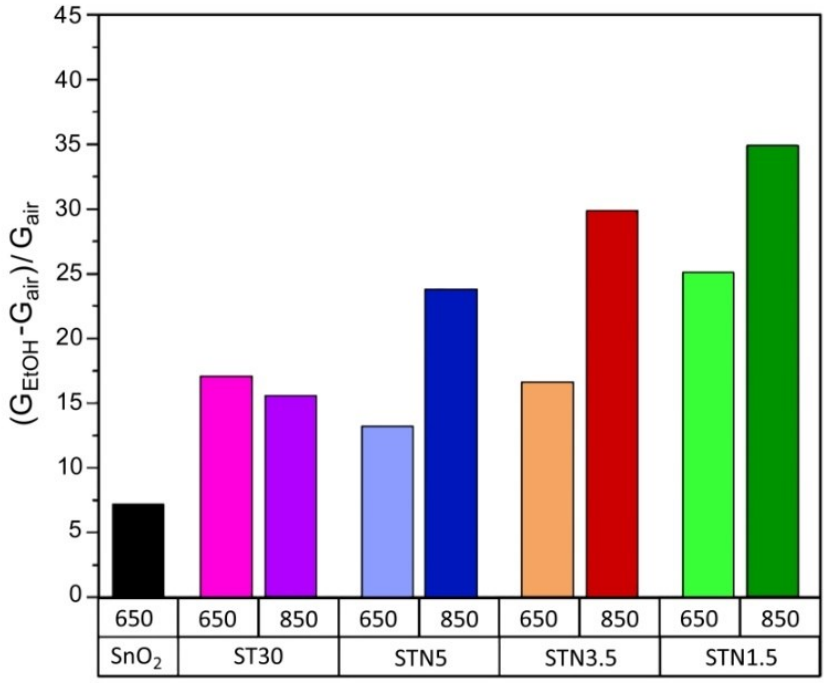

Fig. 3.31 Response to 35 ppm of ethanol. During the measurement, the temperature and humidity inside the chamber were 33 °C and 1.7 RH%. The films performed at their optimal working temperature of 450 °C for STN and ST30_650 and 400°C for SnO_2_650.

To study the effect of humidity on the response, 5 ppm of ethanol was fluxed in the gas chamber at a relative humidity up to 55 RH%. **Fig. 3.32** shows the response at operating temperature of 400 and 450 °C estimated as in **eq. 2.12** considering $G_{baseline}$ equal to the conductance value reached at that specific RH%. As an example, the conductance variation of STN3.5_650 after injection of 5 ppm of ethanol at different RH% conditions at operating temperatures of 400 and 450 °C is plotted in Fig. **3.32 b** and **d**, respectively. Despite having a higher response at operating temperature of 400 °C in dry conditions, the sensors were more influenced by humidity than at 450 °C. Indeed, the response of STN sensors operating at 400 °C decreased at 55 RH% in a range between a 55%, for STN3.5_850, and a 70%, for STN1.5_650. When the sensors were operated at 450 °C, instead, STN1.5_850 and STN5_850 reduced their response level of 40% and STN3.5_850 of 24% at 55 RH%, while the response level of STN5_650 and STN3.5_650 in dry condition was maintained in the whole RH% range investigated, with fluctuations of the order of the instrumental reading error (5%). Film selectivity in the working atmosphere for the applications in which STN-based sensors are expected to detect hydrogen and ethanol was explored by exposing the sensor to 50 ppm of ethanol (C_2H_5OH), 50 ppm of hydrogen (H_2), 9000 ppm of carbon dioxide (CO_2), 2 ppm of ammonia (NH_3), 1 ppm of acetone (C_3H_6O), 1 ppm of nitrogen dioxide (NO_2), 25 ppm of methane (CH_4) and 5 ppm of acetaldehyde (C_2H_4O). The concentrations of the selected gases were chosen below their respective threshold limit values (TLV). Moreover, CO_2, NH_3, C_3H_6O and their concentrations were chosen accordingly to those commonly detected in human breath [153,154]. The investigation of selectivity through CO and CH_4 is mandatory because they are both involved in steam reforming of methane (SRM), i.e., the predominant industrial process for manufacturing hydrogen and syngas. Here, steam endothermically reacts with methane to produce H_2 and CO [155,156].

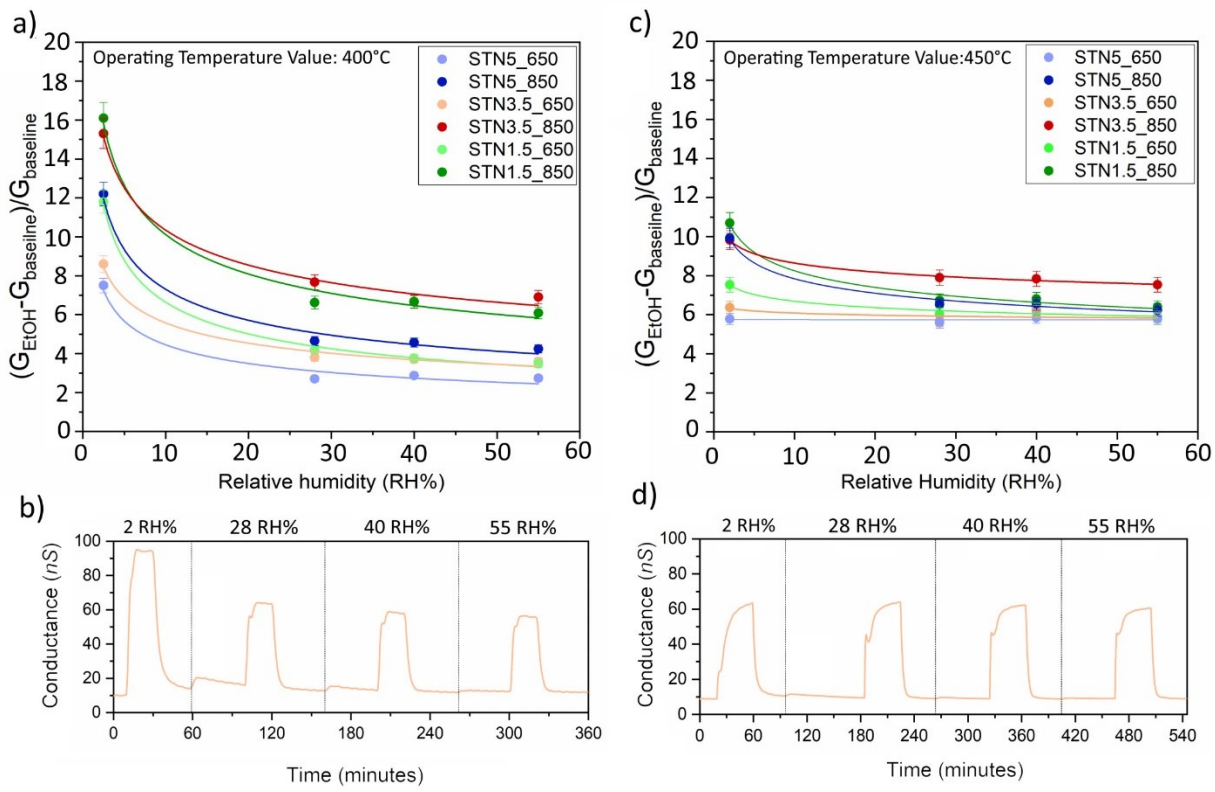

Fig. 3.32 a) Response of STN films and **b)** conductance variation of STN3.5_650 to 5 ppm of ethanol at 2, 28, 40 and 55 RH% and operating temperature value of 400 °C. **c)** Response of STN films and **d)** conductance variation of STN3.5_650 to 5 ppm of ethanol at 2, 28, 40 and 55 RH% and operating temperature value of 450 °C. The temperature inside the chamber was 34 °C in the whole range of RH%.

Hydrogen and ethanol can be present simultaneously in applications such as reaction monitoring of ethanol in steam reforming reactors for hydrogen production [157]. In addition, the films were probed vs. an aldehyde (C_2H_4O), and an oxidizing gas (NO_2), which are thought to be representative of chemical compounds with different functional groups.

Fig. 3.33 highlighted that the response of STN_650 vs. H_2 was much higher than vs. CO_2, NH_3, C_3H_6O, CO, CH_4 and NO_2, and approximately doubled that vs. C_2H_5OH at the same concentration. Despite STN_650 were more selective to H_2 than to C_2H_5OH, it is evident that applications where the concentration of C_2H_5OH is lower than that of H_2 are preferable to avoid cross-sensitivity problems. On the other hand, **Fig. 3.44** evidenced that STN_850 were more selective to C_2H_5OH than STN_650 films. Indeed, the response vs. H_2 of STN_850 films was much smaller than that vs. C_2H_5OH, and comparable to that of the other interferents tested.

Ethanol influence on carbon monoxide (CO) response was further investigated because of interest for air quality monitoring in domestic environments and workplaces [158]**.** CO exposure is common as a result of industrial accidents, faulty fuel-burning appliances, or charcoal burned in homes and other enclosed areas. It is particularly dangerous because it has high affinity to haemoglobin and causes tissue hypoxia [158]. Unfortunately, it is known as the silent killer because it is colourless, odourless, tasteless, and non-irritating. For these reasons CO alarms are used to provide warning as CO levels in the air approach dangerous levels, but the high number of interferent can cause false alarms. One of these interferents is ethanol, for example in the kitchens.

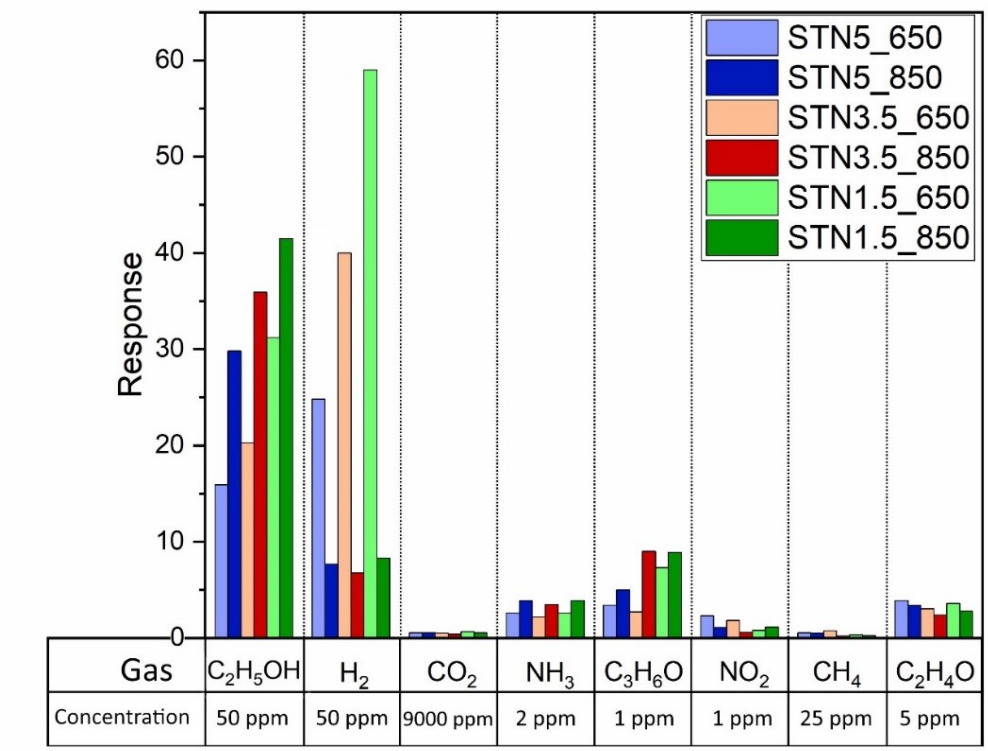

Fig. 3.33 Bar graph of STN film responses (see **Eqs. 2.12** and **2.13**) to 50 ppm of ethanol, 50 ppm of hydrogen, 9000 ppm of carbon dioxide, 2 ppm of ammonia and 1 ppm of acetone, 1 ppm of nitrogen dioxide, 25 ppm of methane and 5 ppm of acetaldehyde. The sensors operating temperature value was set at 450 °C.

Fig. 3.34 a shows the response of STN films to 5, 15 and 30 ppm of CO under flux of 5 or 20 ppm of ethanol. The best way to quantify CO response in presence of a background of 5 or 20 ppm of ethanol was to define the cross-response as:

$$R = \frac{G_{CO} - G_{EtOH}}{G_{EtOH}} \quad eq.3.1$$

where G_{EtOH} and G_{CO} were the steady-states conductance in ethanol and after addition of CO, respectively. STN_850 films did not respond to CO in the presence of ethanol. Conversely, STN_650 films can sense CO even in the presence of 20 ppm of ethanol. In summary, one can conclude remarkable selectivity to ethanol of STN_850 film, and the sensing of CO even in presence of ethanol for STN_650 layers. As an example, the dynamical responses of STN5 650 and STN5 850 films to 5, 10, and 30 ppm carbon monoxide in dry air and after injection of 5 and 20 ppm ethanol are plotted in **Fig. 3.34 b**.

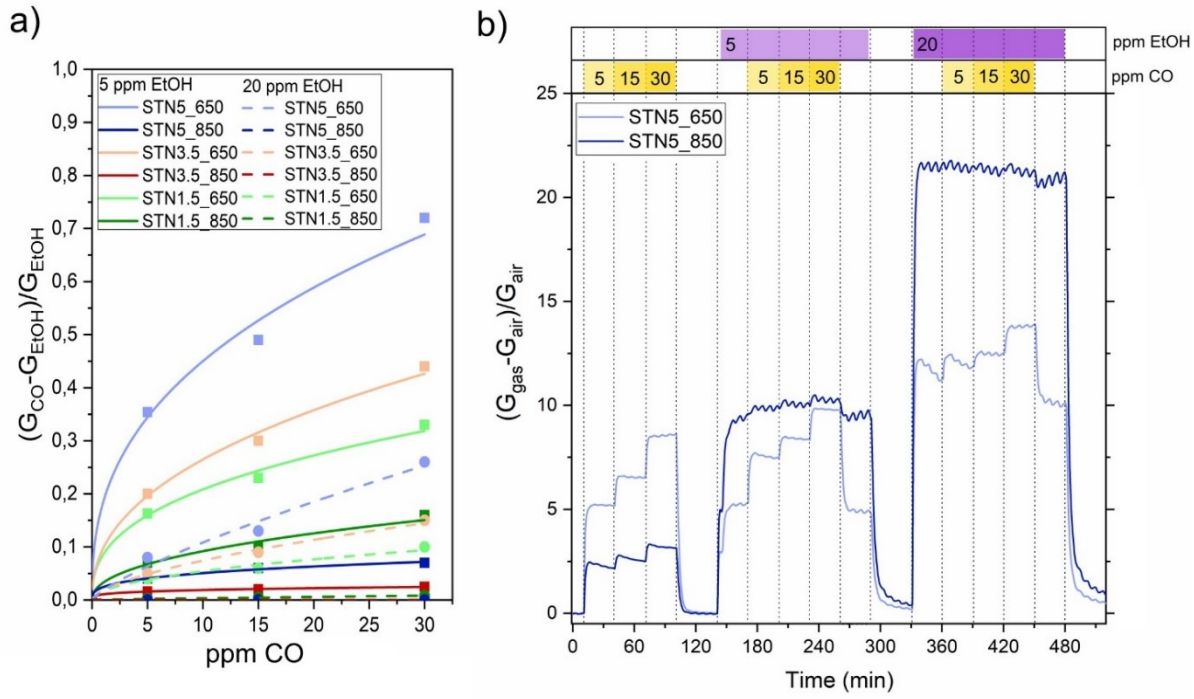

Fig. 3.34 a) The responses of STN films to CO in the presence of 5 and 20 ppm ethanol are displayed by square and round marks, respectively. To guide the eye, continuous and dashed lines are drawn. **b)** Dynamical ethanol and CO cross-responses of STN5 650 and STN5 850 sensors.

** "Reprinted with permission from [ACS Sens. 2022, 7, 573−583]. Copyright [2023] American Chemical Society."*

3.3 DRIFT STUDY ON THE GAS SENSING MECHANISM OF $(Sn,Ti,Nb)_xO_2$

Operando DRIFT spectroscopy was performed to deeply investigate the sensing mechanism of the new $(Sn,Ti,Nb)_xO_2$ solid solution. The apparent absorbance spectra were acquired on STN1.5_650 and STN1.5_850 under exposure to water vapour, 35 ppm of ethanol and 200 ppm of hydrogen. These two gases were chosen because they produced the highest sensor response. The spectra were compared to those obtained at the same working conditions for SnO_2. The reception mechanism vs. some reducing gases and the effect of water vapor on the surface states composition of this material have already been studied using operando DRIFT spectroscopy [32,34,159].

Firstly, the effect of water vapour on the surface sites composition was investigated because $(Sn,Ti,Nb)_xO_2$ sensors demonstrated a greater conductance-independence from variations of RH% than SnO_2_650.

In the experiments, wet conditions were obtained by fluxing synthetic air through a bubbler filled with deionized water. The total flow rate was maintained at 100 sccm, partly consisting of dry air and partly of humid air. To vary the RH%, the portion of the total flow passing through the bubbler was increased step by step to 3, 15, 30, 60 and 100 sccm. A commercially available Sensirion SHT3X sensor monitored the temperature and RH% inside the chamber. To determine the change in the material surface composition resulting from reaction with H_2O, absorbance spectra were calculated as apparent absorbance (AB) using **eq. 2.15**, in which $I_{background}(\lambda)$ and $I_{sample}(\lambda)$ were the spectrum (SC) intensity of the sample recorded during

exposure to synthetic air and that measured after exposure to humid air, respectively. When a high water vapour content was reached inside the test chamber, the gaseous H_2O molecules absorbed in large parts of the mid infrared spectrum (between 4000-3300 cm^{-1} and 2100-1300 cm^{-1}), resulting in narrow and intense peaks [160]. This may complicate the analysis of the species adsorbed on the sample. To avoid absorbance peaks of water vapour, AB spectra were obtained in dry conditions after the sensor conductance stabilization in humid air. The graphs in **Figs. 3.35**, **3.36** and **3.38** on the left (**a,c,e**) depict the RH% and temperature conditions inside the chamber. The coloured bars represent the time intervals during which the AB spectra shown in the graphs on the right (**b,d,f**) were acquired. The colour of each spectrum is the same as the colour of the bar representing the acquisition period.

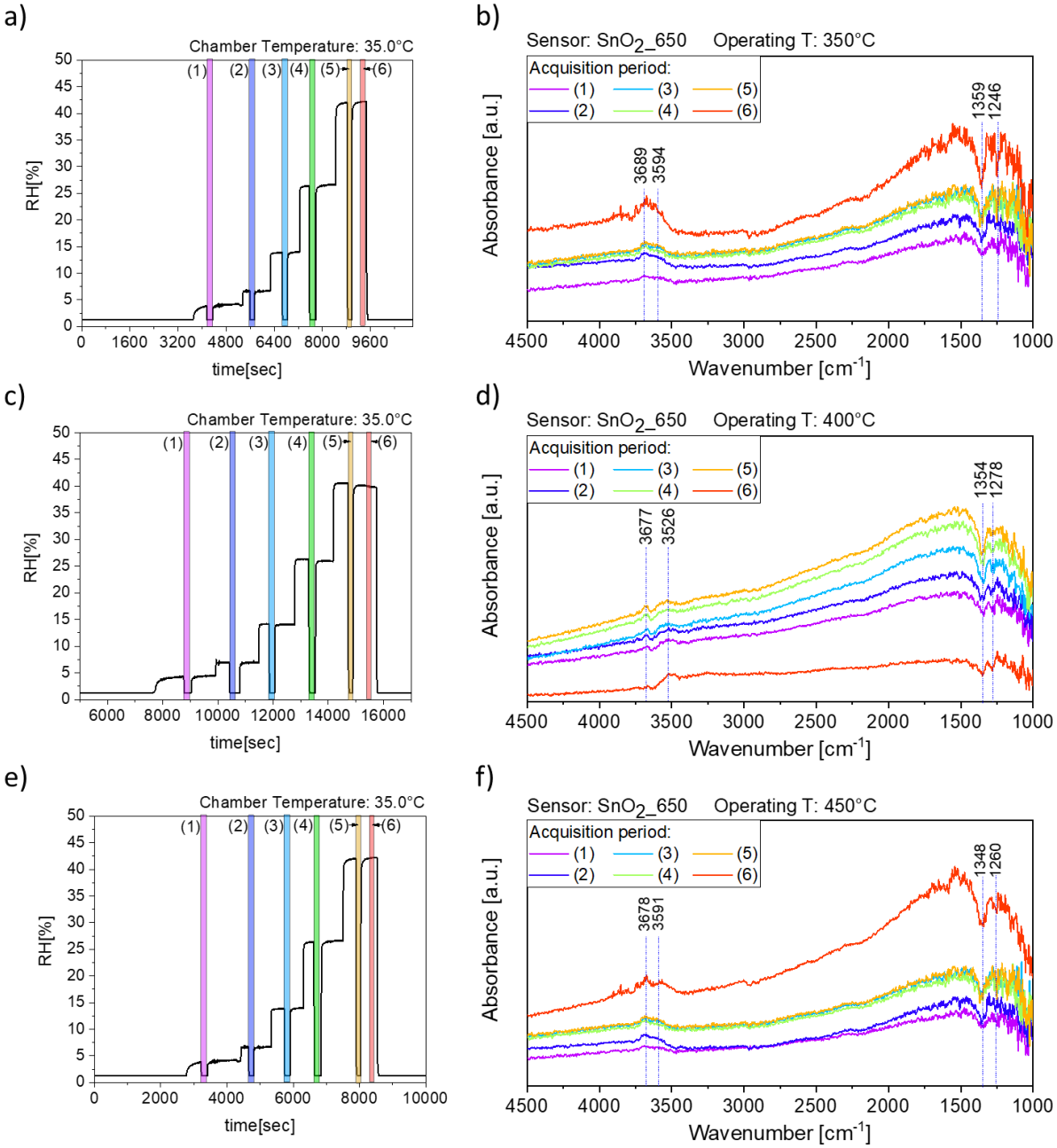

Fig. 3.35 The graphs **a)**, **c)** and **e)** show the RH% and temperature conditions inside the chamber. The coloured bars represent the time intervals during which the AB spectra were acquired. The graphs **b)**, **d)**, **f)** report the evolution of the DRIFT AB spectrum during the increase of RH% on a SnO_2_650 sensor. The sensor operating temperature in graphs (**a-b**), (**c-d**), (**e-f**) was 350 °C, 400 °C and 450 °C, respectively.

This method of investigation had the advantage of producing less noisy spectra, but it had the disadvantage of collecting data on a surface that was restarting the cleaning process from sites that had reacted with H_2O. Therefore, the AB spectrum acquired during exposure to 100 sccm of humid air is also shown in the graphs on the right.

DRIFT spectra on SnO_2_650 in humid air were measured with the sensor working at 350, 400 and 450 °C, as operating temperature was observed to have a significant impact on water vapour chemisorption on the surfaces of SMOX.

The AB spectra of SnO_2_650 operated at 350 °C in humid conditions (**Fig. 3.35 b**) displayed two upward peaks at 3689 cm^{-1}, 3594 cm^{-1} and two downward peaks at 1359 cm^{-1} and 1246 cm^{-1}. The bands in the wavenumber region between 3000 and 4000 cm^{-1} indicate the formation of new surface hydroxyl groups after exposure to humid air. The band at ~3700 cm^{-1} can be ascribed to isolated terminal hydroxyl groups while that at ~3600 cm^{-1} was in the region of interacting terminal and rooted hydroxyl groups (between 3600 and 3100 cm^{-1}) [32–34]. **Fig. 1.10** illustrates a two-dimensional representation of the SnO_2 surface with isolated and interacting hydroxyl groups. In addition to the increasing signal of hydroxyl groups, the absorbance of the band associated with Sn−O overtone [34] at 1359 cm^{-1} decreased, indicating that the formation of hydroxyl groups was accompanied by a decrease in the content of surface metal-oxygen (M−O) bonds. The intensities of the signals enhanced as RH% increased. Two reaction mechanisms have been described in the literature to explain such observed changes in surface sites [34]. The first mechanism in **eq. 4.1** involves the homolytic dissociation of H_2O and its reaction with one lattice oxygen, O_O, to form one terminal hydroxyl group, $\left(M_M^{\delta+} - OH^{\delta-}\right)$, at a M site, M_M, and one rooted hydroxyl group, $(OH)_O^+$, which acts as a surface donor, freeing one electron, e^-, to the conduction band and increasing sensor conductance. The second mechanism in **eq. 4.2** entails the interaction of H_2O with lattice oxygen forming two terminal hydroxyl groups, $M_M^{\delta+} - OH^{\delta-}$, and one oxygen vacancy, V_O^{++}. The formation of V_O^{++} introduces two electrons into the conduction band, resulting in a relatively larger increase in sensor conductance.

$$H_2O_{gas} + O_O + M_M \leftrightarrows \left(M_M^{\delta+} - OH^{\delta-}\right)_M + (OH)_O^+ + e^- \quad \text{eq. 4.1}$$

$$H_2O_{gas} + O_O + 2M_M \leftrightarrows 2\left(M_M^{\delta+} - OH^{\delta-}\right)_M + V_O^{++} + 2e^- \quad \text{eq. 4.2}$$

The presence of both terminal and rooted hydroxyl groups would exclude **eq. 4.2** as preferential reaction for H_2O chemisorption. This could improve the stability of the film in presence of water vapor because if **eq. 4.1** is preferred over **eq. 4.2** only one e^- is released to the CB after dissociation of each H_2O molecule instead of two.

The peak at 1246 cm^{-1} was assigned to a Sn−OH deformation mode by Degler et al. [32]. However, in their observations the absorption peak increased in humid conditions. On the contrary, in **Fig. 3.35 b** the peak was downwards, indicating a decrease of Sn−OH bonds. This interpretation appears to contradict the increase in hydroxyl groups demonstrated by the bands growth in the 3000-4000 cm^{-1} region. Therefore, further investigation is required to define the chemistry of such bond. In particular, the use of isotopically labeled water (D_2O) could provide additional insights into the identification of water-related and other surface species [32]. This experiment will be the next step for a deeper understanding of pre-existing and new surface groups in presence of water vapour.

Even when operating temperature was raised to 400°C, the AB spectra after exposure to humid air highlighted an increase in hydroxyl groups and a Sn−O overtone band decrease (**Fig. 3.35 d**). Interestingly, the band at ~3677 cm^{-1} was less intense than that at 3526 cm^{-1}, indicating a preference for rooted hydroxyl groups formation.

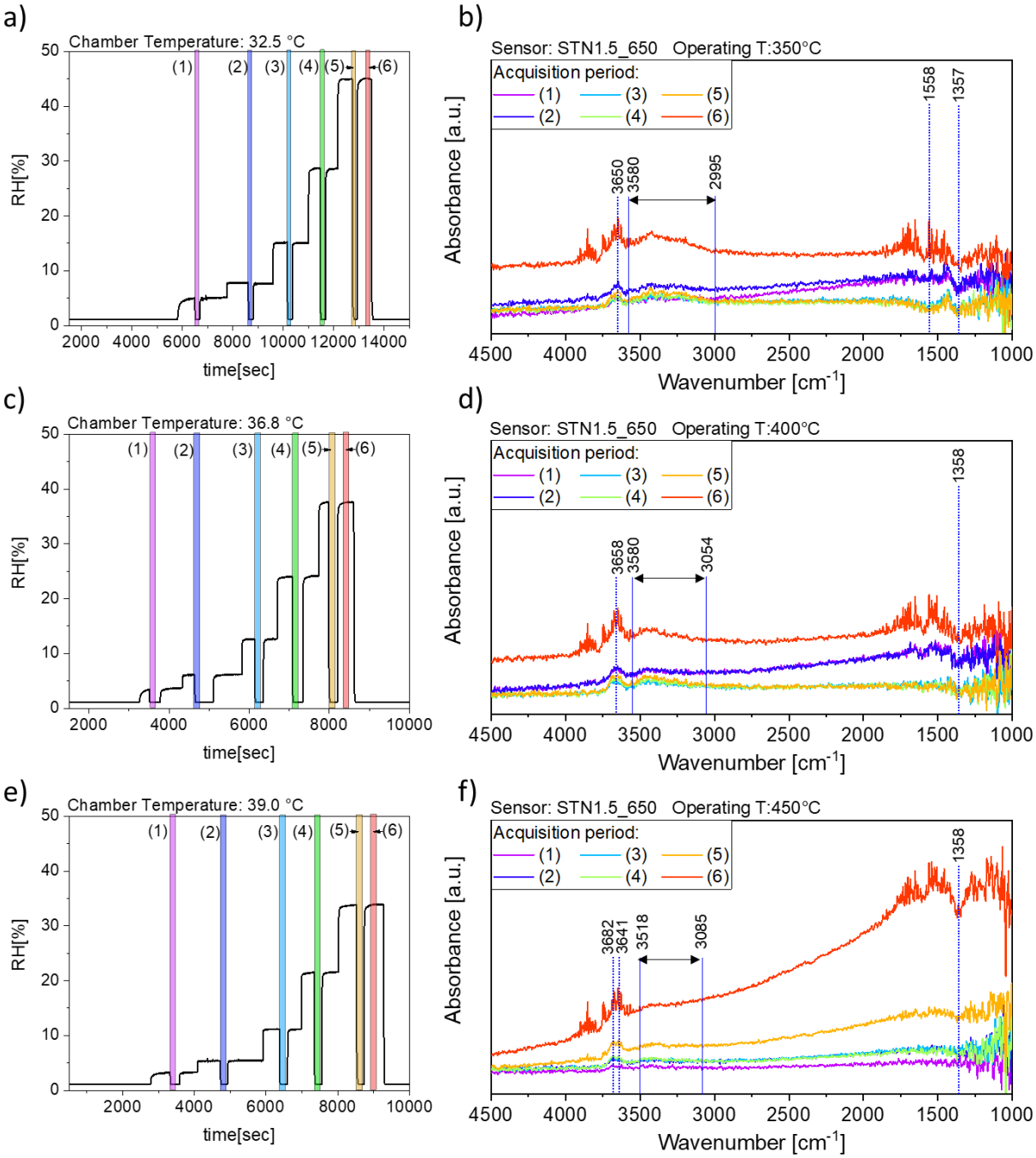

Fig. 3.36 The graphs **a)**, **c)** and **e)** show the RH% and temperature conditions inside the chamber. The coloured bars represent the time intervals during which the AB spectra were acquired. The graphs **b)**, **d)**, **f)** report the evolution of the DRIFT AB spectrum during the increase of RH% on a STN1.5_650 sensor. The sensor operating temperature in graphs (**a-b**), (**c-d**), (**e-f**) was 350 °C, 400 °C and 450 °C, respectively.

On the other hand, a similar intensity of the bands at 3678 cm^{-1} and 3591 cm^{-1} was observed for SnO_2_650 operated at 450 °C (**Fig. 3.35 f**), which suggests that still at high temperature different reaction paths were available for H_2O adsorption.

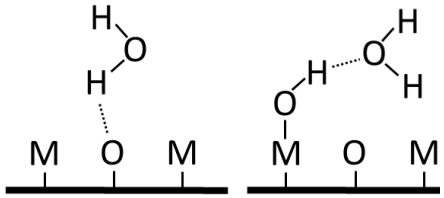

Fig. 3.37 Schematic representation as an example of H_2O molecules involved in hydrogen bonds (dotted line) with oxygens and hydroxyl groups over a metal oxide surface.

The AB spectra in **Fig. 3.36 b** acquired in humid air on STN1.5_650 operated at 350 °C showed an upward peak at 3650 cm^{-1}, a broad increasing band between 3523 cm^{-1} and 3034 cm^{-1} and two downward peaks at 1558 and 1357 cm^{-1}. The peak at 3650 cm^{-1} was attributed to isolated terminal hydroxyl groups. The broad band in the range 3500-3000 cm^{-1} was assigned to water molecules forming a hydrogen-bonded network on the surface [161,162]. This indicates that H_2O dissociated on $(Sn,Ti,Nb)_xO_2$ surface to produce OH groups while also adsorbing non-dissociatively [163] like in **Fig. 3.37**. As already observed for SnO_2_650, the interaction between water vapour and surface oxygen decreased the number of M−O bonds, leading to a decreasing band at 1357 cm^{-1}. In addition, the AB spectra show a downward band centered at 1558 cm^{-1}. Degler et al. [32] observed decreasing peaks in the H_2O spectra at 1543, 1520 and 1427 cm^{-1} which were assigned to Sn−O−Sn overtone.

At increasing operating temperatures of 400 °C and 450 °C (**Fig. 3.36 d** and **f**, respectively), the changes in the fingerprint region show a lower decrease in surface oxygen species. Indeed, the peaks at 1358 cm^{-1} and 1558 cm^{-1} were far less intense and could not be distinguished from background noise at low humidity.

The addition of Nb and Ti in the structure of SnO_2 slightly changed the chemistry of the newly formed surface sites under wet conditions in STN1.5_650. Indeed, in all AB spectra (**Fig. 3.35** and **3.36**) the signals of bands associated with M−O bonds (~ 1355 and 1555 cm^{-1}) decreased. Moreover, in both SnO_2_650 and STN1.5_650 was observed a peak at ~3700 cm^{-1} characteristic of isolated terminal OH groups. Otherwise, in SnO_2_650 raised a signal assigned to rooted hydroxyl while in STN1.5_650 increased a broad band which contains contributions from both hydrogen bonded surface M−OH species and hydrogen-bonded molecular H_2O.

Moreover, useful consideration can be provided from the peaks intensities in the spectra of the two sensors. However, when comparing absorption spectra measured on different samples, caution is required in drawing conclusions about peak intensities. Although DRIFT measurements are extensively used to achieve qualitative insights on surface species, quantitative analyses are rather complicated because there is no linear relation between band intensity and concentration. Furthermore, the reproducibility of DRIFT signal intensities is sensitive to nanoparticle size, compactness, and distribution within the sample [164]. Therefore, the intensities of the bands in the AB spectra cannot be used to quantify the formation of hydroxyl groups or the decrease in the content of surface M−O bonds. However, the intensity of each peak can be compared to that of the other peaks within the same spectrum. Then, qualitative considerations can be drawn from the relative intensities of peaks in spectra from different samples. For example, the intensity of the peak assigned to M−O bonds in absorbance spectra of **Fig. 3.35 (**SnO_2_650 sensor) was equal to or greater than that of the peaks characteristic of O−H bonds. On the contrary, the intensity of the peak assigned to M−O bonds in absorbance spectra of **Fig. 3.36 (**STN1.5_650 sensor) was smaller or, in the limit case of high operating temperature, not clearly visible compared to the peak and band characteristic of O−H bonds. If the chemisorption mechanism in **eq. 4.1** and **4.2** were the only reactions, an increase in O−H peaks should be always followed by a decrease in M−O peak, as in the case of

SnO_2_650. This was not observed for STN1.5_650 and much fewer oxygens were involved in the reaction with water. Indeed, most species were molecular water attached to surface oxygens through hydrogen bonds, whereas the hydroxyls were observed in lesser amounts. This beneficially impacted the electrical stability of STN1.5_650 films in humid atmosphere, promoting H_2O non-redox reactions.

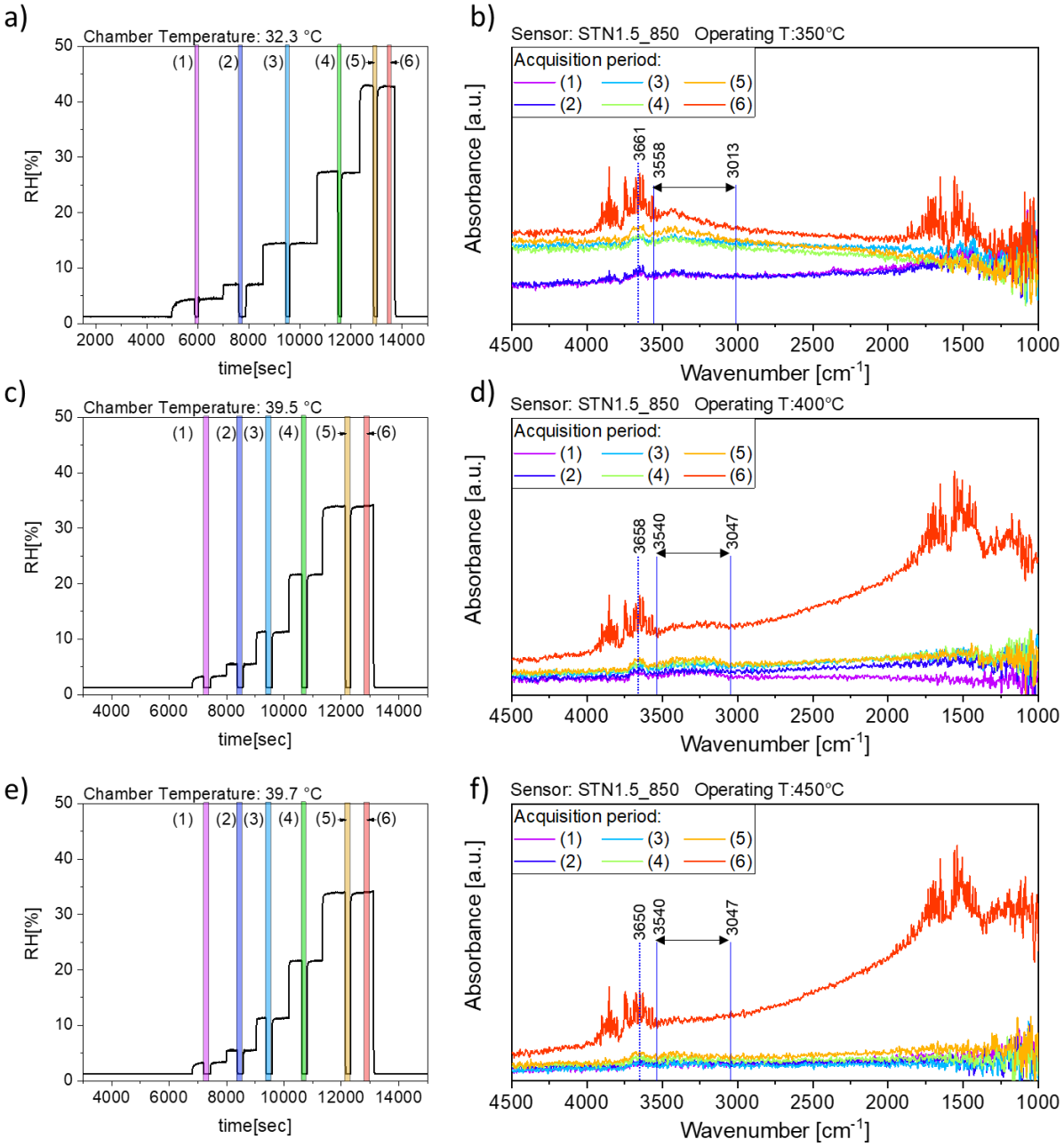

Fig. 3.38 The graphs **a)**, **c)** and **e)** show the RH% and temperature conditions inside the chamber. The coloured bars represent the time intervals during which the AB spectra were acquired. The graphs **b)**, **d)**, **f)** report the evolution of the DRIFT AB spectrum during the increase of RH% on a STN1.5_850 sensor. The sensor operating temperature in graphs (**a-b**), (**c-d**), (**e-f**) was 350 °C, 400 °C and 450 °C, respectively.

DRIFT measurements were conducted also on STN1.5_850 under exposure to humid air to investigate the effect of sintering temperature at 850°C on the surface reactivity. At a working temperature of 350 °C the spectra in **Fig. 3.38 b** show an upward peak at 3661 cm^{-1} and a broad increasing band between 3558 cm^{-1} and 3013 cm^{-1}. The same signals were also present in

STN1.5_650 (**Fig. 3.36 b**) and attributed to terminal and hydrogen bonded OH. Unlike the spectra in **Fig. 3.36 b**, already at this temperature no peaks characteristic of M−O bonds were visible. The same was observed in the spectra measured at 400 °C and 450 °C in **Fig. 3.38 d** and **f**, respectively. Likewise to STN1.5_650, the conductance of STN1.5_850 was almost completely independent from RH% and the spectra suggested water interaction through non-redox adsorption.

Finally, DRIFT spectra were acquired on SnO_2_650, STN1.5_650 and STN1.5_850 under exposure to 35 ppm of ethanol and 200 ppm of hydrogen (**Fig. 3.40**). To determine the change in the material surface composition resulting from reaction with the analytes, AB spectra were calculated as in **eq. 2.15**, in which $I_{background}(\lambda)$ was the spectrum (SC) intensity of the sample recorded during exposure to dry synthetic air. Three AB spectra were collected for each measurement during response time, steady state condition and recovery time, i.e., the periods of time shown in **Fig.3.39**, taken as explicative example. DRIFT spectra on SnO_2_650 during exposure to ethanol presented upwards peaks at 3677 cm^{-1}, 3526 cm^{-1}, 1533 cm^{-1} and 1469 cm^{-1} and downwards peaks at 2970 cm^{-1}, 1354 cm^{-1} and 1159 cm^{-1} (**Fig. 3.51 a**). Therefore, the reaction produced terminal and rooted hydroxyl groups (3677 cm^{-1}, 3526 cm^{-1}) while decreased the content of Sn−O bonds (1354 cm^{-1}). The signal at 1159 cm^{-1} was also assigned to Sn−O overtones in [32]. Furthermore, increasing peaks at 1533 cm^{-1} and 1469 cm^{-1} were observed due to symmetric and asymmetric COO stretch, which corresponded to acetate species formed as intermediates from ethanol reaction [34]. The signal at 2970 cm^{-1} was in the region of CH stretching [165] and interacting OH [32]. More research is needed to determine the chemical species which correspond to this peak. During recovery time all the bands disappeared, demonstrating complete reversibility of the SnO_2_650 surface.

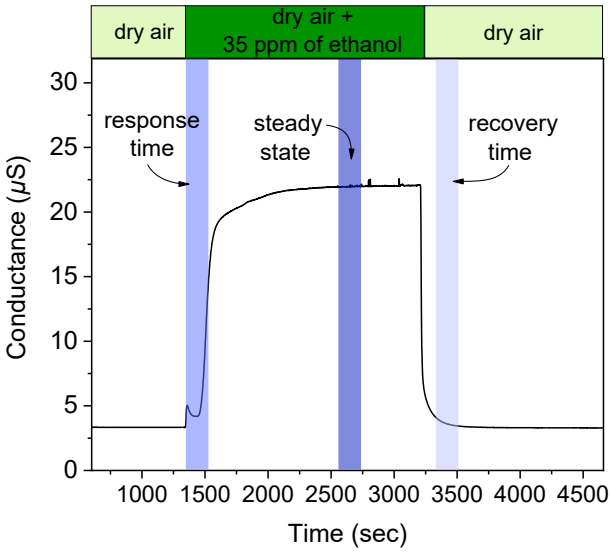

Fig. 3.39 Conductance of SnO_2_650 operated at 400°C before and after exposure to 35 ppm of ethanol. The green bar shows the gaseous composition of the flow passing through the chamber. The blue bars evidence the periods of time during which the spectra in **Fig. 3.40 a** were acquired.

The AB spectra in **Fig. 3.40 b** acquired in presence of H_2 show characteristic signals of hydroxyl groups increase (3677 cm^{-1} and 3580 cm^{-1}) and Sn−O bons decrease (1352 cm^{-1} and 1159 cm^{-1}). Moreover, a weak band at 1533 cm^{-1} was observed, probably due to residual carbonic species at the surface.

The spectra in **Fig. 3.40 c** revealed that ethanol interaction with the surface of STN1.5_650 resulted in the formation of the species also present on SnO_2_650, namely hydroxyl (3682 cm^{-1} and 3583 cm^{-1}) and COO (1534 cm^{-1}) groups. Meanwhile, the decrease in M−O bonds was indicated by the downward peak at 1349 cm^{-1}. The M−O peak at 1366 cm^{-1} decreased and the O−H peak at 3660 cm^{-1} increased also in the presence of hydrogen (**Fig. 3.40 d**). In this case, however, a single band was observed in the region of the OH groups that, in terms of position

and shape, resembled that observed in the presence of H_2O (**Fig. 3.36 f**) more closely than that observed in the presence of ethanol. This would suggest that different sites were exploited for the reaction of hydrogen and ethanol, mainly generating terminal OH groups in the first case and both terminal and rooted OH groups in the second.

The reaction mechanism of ethanol and hydrogen on the surface of STN1.5_850 only decreased M−O bonds content. Indeed, a single downwards peak was observed at 1358 cm^{-1} in **Fig. 3.40 e** and at 1352 cm^{-1} in **Fig. 3.40 f**.

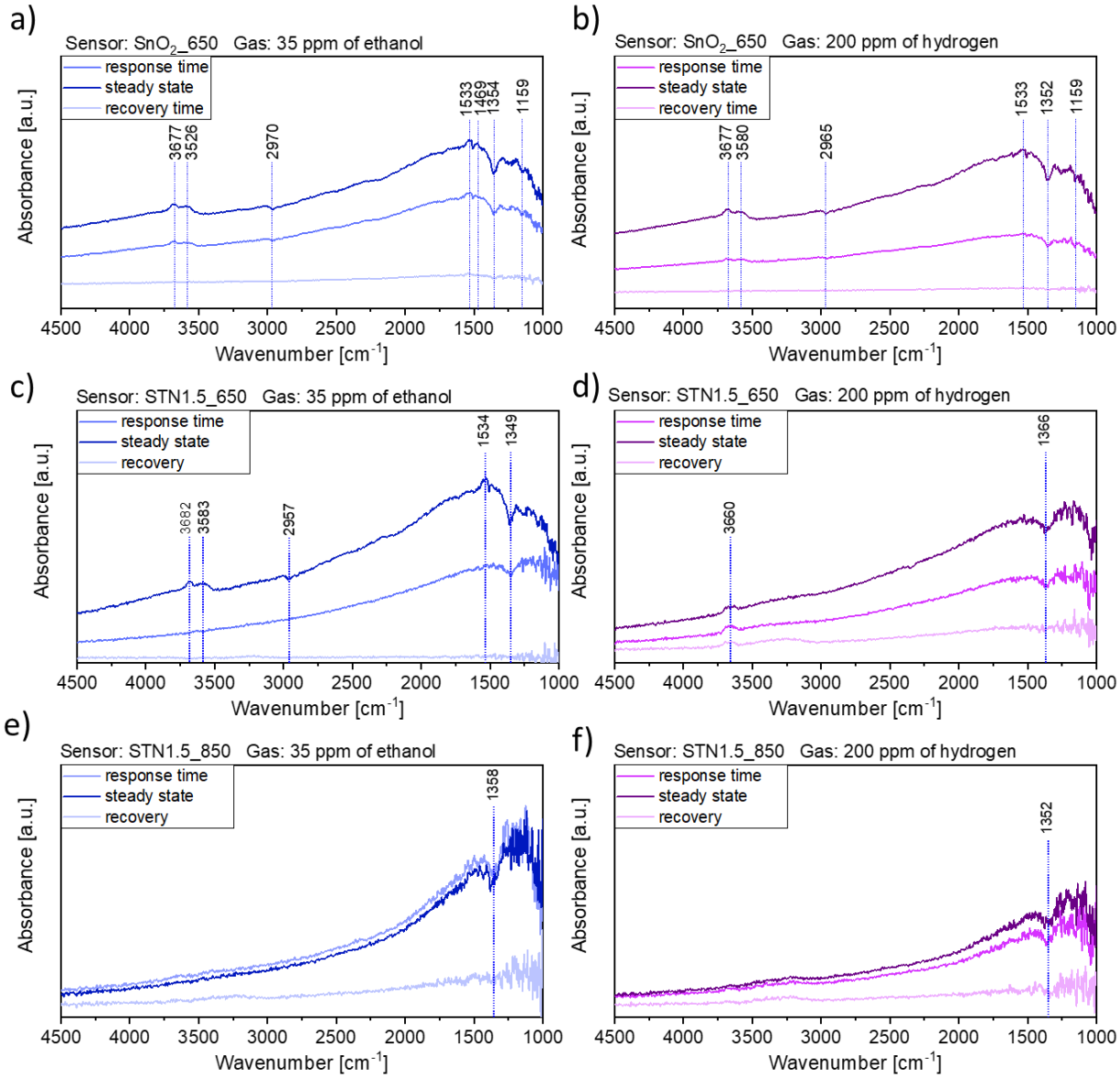

Fig. 3.40 AB spectra taken on SnO_2_650, STN1.5_650 and STN1.5_850 during (response time and steady state) and after (recovery time) exposure to **a),c),e)** 35 ppm of ethanol and **b),d),f)** 200 ppm of hydrogen. The operating temperatures were 400°C for SnO_2_650 and 450 °C for STN1.5_650 and STN1.5_850. The temperature inside the chamber was in the range of 36-38 °C and RH was around 1.5%.

In conclusion, DRIFT measurements evidenced that exposure to water vapor, ethanol and hydrogen modified the surface chemistry differently on SnO_2_650, STN1.5_650 and STN1.5_850. This implies that different reaction mechanisms occur in the presence of these gases, influencing the electrical behavior of the sensor.

3.4 WO_3 NF AND $(Sn,Ti,Nb)_xO_2$-BASED SENSORS COMPARED TO OTHER SMOX MATERIALS FROM THE LITERATURE

This chapter compares the sensors developed during the thesis work and characterized in sections 3.1 and 3.2 with sensors previously studied in the literature. The purpose is to see if the changes to the structural parameters chosen for the reasons stated in section 2.1 improved the materials based on WO_3 and SnO_2 enough to make them competitive with other gas sensors based on metal oxides. This evaluation is limited to sensors that have the same selectivity for ethanol, as WO_3 NF and STN_850, and for H_2, as STN_650. All the SMOX materials in **Table 3.8** and **3.9** employ one or more techniques for structural parameter engineering, such as morphology control, chemical composition, and surface structure modification.

In **Table 3.8**, the WO_3 in nanoflake morphology (WO_3 NF) and the solid solution of tin, titanium and niobium oxides (STN) are compared to other SMOX-based sensor for ethanol detection. The sensors are evaluated for their level of response to the analyte, best operating temperature, and percentage of response decrease at 60% RH. Indeed, even though the response level is an important criterion for evaluating the sensor's performance, additional relevant factors must be considered. In particular, the low operating temperature is a desirable feature that can have a favourable impact on heating power consumption, convenient characteristic especially for portable applications of SMOXs-based gas sensors [166]. Moreover, humidity can be adverse to film performance, causing the sensor response to decrease when operating under environmental conditions. Low or no dependence of sensor baseline and response to significant relative humidity changes is a strong selling point for making the device more robust and easier to calibrate.

Firstly, the response of the WO_3 NF film to ethanol is compared to other sensing films based on WO_3 with different morphologies. WO_3 NF outperformed WO_3 films in Refs [138,167,168], whereas it had a slightly lower response than WO_3 films in Refs [139,169,170]. It is worthy to note that the 3D flower-like WO_3 film in Ref. [171] demonstrated an exceptionally high response due to surface effect magnification. In this respect, the WO_3 NF films were worked at 250 °C, while the others were operated at higher temperatures. The material that comes closest to WO_3 NF in terms of performance is the WO_3 nanolamella [44], with a high response at a low operating temperature. Nevertheless, the low number of interferents tested and the poor control of the environment in the chamber (T and RH%) make comparing the two sensors for practical uses difficult. However, Tie Liu et. al. [44], contributed to demonstrating that 2D morphology is likely the most promising for the development of ethanol sensors. WO_3 NF film is also competitive with sensors based on various n-type (SnO_2 [172,173], ZnO [174]) and p-type (CuO [175]) metal oxides synthetized in different shapes, as it had a better response or worked at a lower temperature, or both. Furthermore, despite the scarcity of data in the literature, the WO_3 NF films proved to be less affected by humidity.

Secondly, the response of the STN1.5_650 and 850 films is compared to WO_3-based films, other n-type (SnO_2 [172,173], ZnO [174]) and p-type (CuO [175]) metal oxides as well as composite materials based on SnO_2 [176–180] Most devices have a lower response level than STN-based sensors. However, STN operated at a higher temperature than all of the sensors listed in **Table 3.8**. Despite the higher energy consumption, STN materials may be preferred over others in humid environments due to their low dependence of sensor baseline and response on the presence of water vapour.

Table 3.8. The ethanol-sensing performance of the WO_3 NF film in this work is compared to that of other WO_3 sensors with different morphologies, as well as several commonly used metal oxide sensors in the literature [138,139,175,181,167–174].

Material	Concentration		Response	Optimal operating temp. (°C)	Response% decrease at 60% RH	Reference
WO_3 nanoflakes	**50 ppm**		**20.5** [a]	**250**	**25 %**	**This work**
STN1.5_850 nanoparticles	**50 ppm**		**41.5** [a]	**450**	**33%**	**This work**
STN1.5_650 nanoparticles	**50 ppm**		**31.1** [a]	**450**	**15%**	**This work**
WO_3 nanolamella	10 ppm		11.3 [b]	200	–	[44]
Flower-like WO_3	100 ppm		7.6 [b]	320	–	[167]
WO_3 nanotube	300 ppm		16.9 [b]	350	–	[138]
Urchinlike WO_3 microspheres	400 ppm		~17 [c]	300	–	[168]
WO_3•H_2O nanoplates	50 ppm		23.1 [b]	300	–	[169]
flower-like WO_3	50 ppm		29.7 [b]	300	–	[139]
h-WO_3 nanowires	50 ppm		~ 22 [b]	300	–	[170]
3D flower-like WO_3	35 ppm		96 [b]	350	57%	[171]
SnO_2 nanowires	100 ppm		17 [b]	380	–	[172]
SnO_2 microspheres	100 ppm		24.9 [b]	230	30%	[173]
ZnO nanorods	100 ppm		44.9 [b]	300	25%	[174]
CuO nanowires	100 ppm		4.4 [b]	190	–	[175]
Au/SnO_2 hierarchical hollow microspheres	100 ppm		23.9 [b]	240	–	[176]
2%Ce-SnO_2 nanoparticles	50 ppm		69.5 [b]	265	–	[177]
SnO_2/Zn_2SnO_4 porous sphere	100 ppm		30.5 [b]	250	–	[178]
ZnO/SnO_2 hollow spheres	30 ppm		34.8 [b]	225	–	[179]
hierarchical nano Pt/SnO_2	100 ppm		27 [b]	240	–	[180]

[a] Gas response $S = \frac{G_{gas} - G_{air}}{G_{air}}$, [b] Gas response $S = \frac{R_{air}}{R_{gas}}$, [c] Gas response $S = \frac{V_{gas}}{V_{air}}$, [d] Gas response $S = \frac{[(R_{air} - R_{gas}) \times 100]}{R_{air}}$, where G is the conductance, R is the resistance and V is the voltage. Hyphen " – " is used when data are not available from the reference.

The response of STN1.5_650 to H_2 and that of other sensing films based on different metal-oxide semiconductors from literature are reported in **Table 3.9**.

STN 1.5 650 performed better than several semiconductors, including SnO_2 and Pd-decorated and Co-doped SnO_2 [182–184], WO_3 [185], CuO [186], WO_3 and CuO junction [185], ZnO and Ag doped ZnO [187]. Moreover, its experimental LOD of 0.4 ppm was far lower than that reported in some recently accredited works [186,187]. On the other hand, the best experimental result about H_2 sensing was performed by Wang et al. [183], recording a LOD of 0.25 ppm at R_{air}/R_{gas}= 3. However, the LOD for STN1.5_650 was 0.4 ppm, but with a response of 5.6. Based on this experimental result, it is concluded that STN1.5_650 highlights remarkable, still experimentally unexplored, potential for detecting extra-low concentrations of H_2. The method described by Huang and Wan [174] was used to assess such a limit. The theoretical LOD turned

out to be as low as 5 ppb, i.e. the lowest theoretical LOD obtained so far by metal-oxide gas sensors.

Table 3.9. Comparison of the hydrogen-sensing performance of STN1.5_650 films to recently achieved frequently used metal-oxide sensors in the literature [29,182–187].

Material	Concentration	Response	Optimal operating temperature (°C)	LOD	Reference
STN 1.5 650	**100 ppm**	**80** [a]	**450**	**0.4 ppm/5 ppb***	**This work**
SnO_2	100 ppm	15 [c]	400	-	[182]
Pd/SnO_2	100 ppm	28.5 [c]	160	0.25 ppm	[183]
Co/SnO_2	100 ppm	23 [c]	330	-	[184]
WO_3	100 ppm	4.8	250	0.25 ppm *	[185]
WO_3-CuO	100 ppm	39	250	0.31 ppm *	[185]
CuO	100 ppm	1.7 [d]	200	2 ppm	[186]
ZnO	100 ppm	0.95 [e]	250	-	[187]
Ag/ZnO	300 ppm	4.79 [e]	250	5 ppm	[187]

[a] Gas response $S = \frac{G_{gas}-G_{air}}{G_{air}}$, [b] Gas response $S = \frac{G_{gas}}{G_{air}}$, [c] Gas response $S = \frac{R_{air}}{R_{gas}}$, [d] Gas response $S = \frac{R_{air}-R_{gas}}{R_{air}}$, [e] Gas response $S = \frac{R_{gas}-R_{air}}{R_{gas}}$, where G is the conductance, R is the resistance and V is the voltage. The symbol "*" indicates theoretical LOD.

Chapter 4- GAS SENSING MECHANISM

4.1 WO_3 NF- BASED SENSORS

The reaction mechanisms that occur at the surface of WO_3-based films as a result of interaction with the gaseous environment are here reviewed. When exposed to air, oxygen molecules chemisorbed at the surface, and active oxygen ions (such as O_2^-, O^-, and O^{2-}) are formed at various temperatures by trapping electrons from the CB. According to the literature [17], O^- should be preferentially formed at the best working temperature for WO_3 NF operation, which is 250 °C.

Under exposure to reducing gases (such as alcohols) at a temperature that provides enough thermal energy for surface reactions, oxygen ions oxidize the gas and the trapped electrons are released to the conduction band, resulting in a decrease in film resistivity. Since WO_3 is an acidic oxide [188,189] the sensing mechanism for ethanol detection would proceed through its chemisorption (**eq.4.1**), dehydration (**eq. 4.2**) [190,191] and decomposition to form H_2O and CO_2 (**eq. 4.3**) [192].

$$C_2H_5OH \rightarrow (C_2H_5OH)_{ads} \text{ eq. 4.1}$$
$$(C_2H_5OH)_{ads} \rightarrow C_2H_4 + H_2O \text{ eq. 4.2}$$
$$(C_2H_4)_{ads} + 6O^-_{ads} \rightarrow 2CO_2 + 2H_2O + 6e^- \text{ eq. 4.3}$$

Methanol and butanol react very similarly [193–195]:

$$(CH_3OH)_{ads} + 3O^-_{ads} \rightarrow CO_2 + 2H_2O + 3e^- \text{ eq. 4.4}$$
$$(C_4H_9OH)_{ads} + 12O^-_{ads} \rightarrow 4CO_2 + 5H_2O + 12e^- \text{ eq. 4.5}$$

A deeper examination at the responses vs. alcohols reveals different response levels (**Fig. 3.18**) and kinetics (**Fig. 3.19**) for methanol, ethanol and butanol.

Similar evidence has previously been reported in the literature [192,193,196], and various hypotheses have been proposed to shed light on it. In [90] a hypothesis correlating the film response to two counteracting effects bound up to the length of the alkyl was presented.

Firstly, the complete decomposition of an alcohol with a longer alkyl chain to CO_2 and H_2O involves a higher number of adsorbed O^- surface sites, e.g., $3O^-_{ads}$ for methanol (**eq. 4.4**), $6O^-_{ads}$ for ethanol (**eq. 4.3**) and $12O^-_{ads}$ for butanol (**eq. 4.5**). Consequently, the number of electrons e^- which can be released to the CB increases from methanol to butanol, resulting in a higher response vs. ethanol than that vs. methanol. This effect, however, does not explain why the response to butanol is lower than that to ethanol.

Secondly, according to the pore-size distribution curve in **Fig. 3.3 b**, the sample shows a meso-macroporous structure which influences the diffusion of the analyte through the sensing layer. At constant operation conditions, physical quantities d (pore diameter) and T (temperature) are constant, whereas m (molecular mass) and d_g (molecular diameter) depend on the analyte. Both of these latter decrease the diffusion through the pore (D_{pore}) according to **eq.1.18** by increasing the alkyl length from methanol to butanol. Sakintuna et al. [197] reached a similar conclusion for the diffusion of volatile organic compounds in porous media. Then, a lower diffusion would reduce the response to butanol by limiting its interactions with the active surface area of the WO_3 NF film and would increase the time to attain equilibrium [197].

In summary, the greater response to ethanol can be explained satisfactorily as a trade-off between the number of electrons released after its decomposition on the WO_3 NF surface and molecule diffusivity in the pores of the sensing material.

4.2 $(Sn,Ti,Nb)_XO_2$-BASED SENSORS

As its parent oxides, the solid solution of $(Sn,Ti,Nb)_xO_2$ behaves like an n-type semiconductor material and the film conductance increases when the sensor is exposed to reducing gases such as ethanol and hydrogen. Operando DRIFT measurements demonstrated that the sensing mechanism always involves surface oxygens consumption. According to the literature [17], oxygen active sites should be mainly O^- and O^{2-} over the surface of SMOX films operated between 350 and 450 °C. Under exposure to H_2, adsorbed oxygen species oxidize the reactive gas generating water and free electrons as in **eq. 4.6** and **4.7** [198]. Then, water vapor may interact with the surface as hydroxyl ions.

$$H_2 + O^- \rightarrow H_2O + e^- \quad \text{eq. 4.6}$$
$$H_2 + O^{2-} \rightarrow H_2O + 2e^- \quad \text{eq. 4.7}$$

Ethanol decomposition undergoes through dehydration (**eq. 4.2**) or dehydrogenation (**eq. 4.8**) routes depending on the acid-basic properties of the solid solution, followed by consecutive reactions of the intermediate states which consume the adsorbed oxygens and release free electrons as in **eq. 4.3** and **4.9** [191].

$$(C_2H_5OH)_{ads} \rightarrow CH_3CHO + H_2 \text{ eq. 4.8}$$
$$(CH_3CHO)_{ads} + 5O^-_{ads} \rightarrow 2CO_2 + 2H_2O + 5e^- \text{ eq. 4.9}$$

By increasing the concentration of free charge carriers and decreasing the Schottky barrier height at the inter-crystallite boundary, the reactions between the analytes and the active sites on the $(Sn,Ti,Nb)_xO_2$ surface increase the overall conductance of the nanostructured film.
The response of $(Sn,Ti,Nb)_xO_2$ films, as well as their sensitivity and selectivity, were clearly influenced by the Nb content and sintering temperature.
First, STN 650 films responded better to H_2 than STN 850 films. This can be interpreted in terms of a larger surface area of the former compared to the latter, as highlighted by BET measurements in **Table 3.2**. Furthermore, operando DRIFT spectra revealed that H_2 increased the content of OH groups in STN1.5_650 but not in STN1.5_850. The second step reaction of H_2O (coming from **eq. 4.6** or **4.7**) to form hydroxyl groups may contribute to the conductance increase, thereby further enhancing the response.
Second, it was demonstrated that STN1.5_650 and STN3.5_650 improved the response vs. H_2 of ST30_650 while STN5_650 had the opposite effect. All the samples treated at 650 °C had similar textural properties, therefore a larger surface-to-volume ratio in contact with the gases cannot be called forward. However, XPS analyses revealed that the films' surface relative composition of Sn, Ti, and Nb differed, namely, the Nb content in STN1.5_650 was lower than that in STN3.5_650 and STN5_650. Because Nb_2O_5 do not have qualified properties for H_2 detection [199], the presence of Nb evidently increases the reactivity of neighbouring sites by creation of cation vacancies and trivalent cations. This would explain the improved sensitivity of STN1.5_650 than that of ST30_650. On the contrary, a high superficial proportion of Nb would produce an excess of low reactive sites, resulting in a reduced response of STN3.5_650

and STN5_650. Further measurements on samples containing different Nb concentrations may help to confirm this hypothesis.
Third, STN_650 and STN_850 films had different selectivity, namely the former for hydrogen and the latter for ethanol. The main differences between the STN 850 films and STN 650 ones were the specific surface area and the pore size. The specific surface area would only affect the magnitude of the response and not influence the selectivity. Instead, the pore size may play a significant role as the main free path of the molecules is comparable to the length of the pores [21,29,90]. Indeed, the pore size may affect the selectivity as it is small enough to make the diffusion properties of the gases in the film dependent on their molecular diameter and mass [29]. The mean pore size of the STN_650 samples was smaller than that of the STN_850 ones, e.g., 16.7 nm for STN1.5_650 and 24.0 nm for STN1.5_850. In this way, the STN_650 films would become more selective to hydrogen because H_2 molecules diffuse deeper into the films than much larger molecules such as C_2H_5OH, thereby enabling a relatively wide surface for its sensing. On the other hand, STN_850 films were better suited for ethanol detection because of a more advantageous trade-off between mesoporous structure and specific surface area [12]. Moreover, the cross-response of the sensors in the presence of ethanol and carbon monoxide (CO) provided additional evidence for the influence of pore size distribution on the selectivity of the films (see **Fig. 3.45**). Because CO, due to its smaller size, can diffuse through smaller pores and reach unreacted active sites without competing with ethanol, only the STN 650 films detected CO in the presence of ethanol.
Finally, the effect of humidity on the electrical properties of the films was taken into account because adsorption/desorption processes of H_2O molecules on the surface may affect the conductance of the sensor as a result of redox reactions and may compete with the analyte for surface-active sites. In particular, it should be explained the negligible influence of water to the baseline conductance of $(Sn,Ti,Nb)_xO_2$ films. Operando DRIFT apparent absorbance spectra demonstrated that most species were molecular water attached to the surface through hydrogen bonds, whereas the hydroxyls were observed in lesser amounts. This beneficially impacted the electrical stability of the films in the humid atmosphere, promoting H_2O non-redox reactions. The different adsorption properties of the solid solution were promoted by substitution of Ti in Sn sites. Already in 1981, Egashira et al. studied the difference of water adsorption properties between SnO_2 and TiO_2 [200]. They disclosed that most of the surface oxygens were hydroxylated upon water adsorption on SnO_2 while on the TiO_2 surface most species were molecular water attached to surface oxygens. The reasons behind this experimental evidence were the greater difectivity of SnO_2, which made its surface more reactive than that of TiO_2. Density Functional Theory calculations by Bandura et al. also concluded that monolayers of water prefer to be in molecular form on the TiO_2 surface while the fraction of the dissociated molecules on the SnO_2 surface is larger [201]. Although the humidity-independent conductance of TiO_2 is a significant advantage for gas sensors, the material poor surface reactivity reduces the device's sensitivity to most analytes. Then, the substitutional solid solution $(Sn,Ti)_xO_2$ exploits the good sensitivity of SnO_2 towards most analytes and low cross-sensitivity of TiO_2 to humidity. On the other hand, the film conductance decreased significantly with the increase of the Ti concentration, going from μS for SnO_2 to nS for $Sn_{70}Ti_{30}O_2$ in synthetic air under termo-activation. This forces the ST30_650 sensor to operate only at high working temperatures up to 450 °C. Unfortunately, at these operating temperatures, the nanostructured film may suffer from grains coalescence and anatase-to-rutile phase transition [81,83,93]. Then, addition of Nb improved the structural stability of the material, thereby enabling long term operation at 450 °C

(as suggested by **Fig.3.7**) , i.e. the best operating temperature for low influence of humidity and better sensing performance for STN_650 and STN_850.

Chapter 5- CONCLUSIONS AND FUTURE PROSPECTIVES

The results presented in this work demonstrated the potential of morphological control and chemical composition and structure modifications for the optimization of well-known metal oxides (WO_3 and SnO_2) for the detection of ethanol and hydrogen. Metal oxide semiconductor gas sensors have been extensively researched since in the late 1980s. Then, the vast literature in this field finally allows us to rely on consolidated methodologies and take the next step in controlled optimization of nanomaterials for specific gas sensing applications.

The first strategy aimed to control the size and shape of WO_3 to obtain 2D nanostructured powders and optimize the semiconducting film active surface area and porosity. WO_3 nanoflakes powders have been synthetized through a simple and time effective solvothermal method and then used to produce thick films. The sensors exhibited a higher response to ethanol than they did to gaseous molecules belonging to different chemical species, as well as to alcohols with different alkyl lengths, namely methanol and butanol. The sensor selectivity for ethanol was driven by its peculiar surface reactivity, probably induced by low concentrations of oxygen vacancies, as well as its meso-macro porosity, which influenced the diffusion of the analytes through the sensing layer. Currently, the proposed mechanism for ethanol detection is based mostly on a jigsaw of comprehensive literature searches that demonstrated chemisorption on WO_3 via dehydration to form H_2O and CO_2 and modeled gas diffusion in transition regimes along well-defined, mesoporous films. However, WO_3 NF can also promote different reaction paths, such as dehydrogenation, and be poorly reactive with specific functional groups or reaction intermediates. Therefore, operando DRIFT spectroscopy should confirm the hypotheses based on the literature. While surface composition can be experimentally investigated, it is more challenging to make precise consideration on gas diffusion in films with inhomogeneous pore size. On the other hand, the porosity of the layer could be varied by changing the thickness and elongation of the 2D nanostructures. By setting up several experiments to vary the pore size it might be possible to define a trend between diffusion of molecules with different mass and dimension and sensor response. This study would be interesting but requires several attempts, then being time-consuming.

The second approach tuned the chemical composition and structure of SnO_2 through substitution of Sn sites with Ti and Nb in different contents. Three sol-gel syntheses with Nb concentration of 1.5, 3.5 and 5 % and Sn-Ti ratio constant to 70:30 mol/mol resulted in nanogranular powders with different composition. A further variability was given by two thermal treatments at 650 °C or 850 °C. The samples were characterized with several methods to retrieve the morphology, structure and bulk and surface chemistry of these new materials. The syntheses did not account for complete transfer of the atomic proportion of the starting stoichiometry into the powders, although a dependence between precursor concentrations and Sn/Ti/Nb content in the final sample was evident. Moreover, the nanograins were characterized by a thin (≈ 1 nm) amorphous layer with a higher Ti and Nb content than the bulk. Ti and Sn were reported to be totally miscible at any ratio, resulting in a substitutional solid solution. Then, the addition of Nb destabilizes the lattice making Ti and Nb segregated over the surface. It is still unclear if the amorphous shell and the inhomogeneous bulk-surface composition benefits or limits the sensing capabilities of $(Sn,Ti,Nb)_xO_2$ nanoparticles. To reduce the

difference in Sn/Ti/Nb proportion between the bulk and the surface of the nanograins, the concentration of Ti and Nb precursors in the synthesis batch should be decreased. In this way, lowering the Ti content is probably the most effective strategy to optimize the solid solution because Nb is already in low concentrations and reducing its content could nullify its beneficial effects.

Indeed, what emerges from this work is that the incorporation of Nb offers a number of advantages. Firstly, addition of a low concentration of Nb (e.g. 1.5%) enhances the surface reactivity by creation of cation vacancies and trivalent cations (Ti^{3+}) which improved the sensitivity to some gases, such as hydrogen and ethanol. Secondly, Nb avoided grain coalescence up to 650 °C, namely well above the operating temperature of the films. On the other hand, while grain coalescence has always been considered to adverse the gas response since the specific surface area scales as the inverse of the grain radius, it must also be stated that an increase in grain size affects porosity too. A change in porosity would then have an effect on the nature of the molecules that can be sensed, i.e. it might modify the selectivity. Indeed, the films obtained from the powders treated at 650 °C have smaller pores and a higher surface area. This makes them ideal for sensing small molecules, such as H_2 or CO. The films obtained from the powders treated at 850 °C, instead, have larger pores and a smaller surface area. As a result, they are well suited for sensing highly reactive and large molecules, such as ethanol. Finally, in humid environments, Ti promoted non-dissociative adsorption of H_2O through hydrogen bonds rather than redox reactions and consequently hydroxyl groups formation. The negligible influence of water vapour on the conductance of the $(Sn,Ti,Nb)_xO_2$ films is a significant advantage because the effect of ambient humidity on the baseline and sensitivity often reduces sensor accuracy and complicates calibrations. Unfortunately, with the increase in Ti concentration, the conductance of the film decreased significantly, forcing to operate the sensor at high working temperature. Then, addition of Nb both increased the conductance of the film based on $(Sn,Ti)_xO_2$ and improved the structural stability of the material, thereby enabling long-term operation at 450 °C, i.e. the best operating temperature for low influence of humidity and better sensing performance for STN_650 and STN_850.

Future perspectives on optimization of WO_3 and SnO_2 will involve their engineering through different combinations of strategies for structural parameter control. For example, the sensitivity of WO_3 nanoflakes can be further enhanced through functionalization of its specific surface area with metal particles, foreign metal oxides or ions. On the other hand, the solid solution of $(Sn,Ti,Nb)_xO_2$ could be synthetized in different shapes (1D or 2D) by solvothermal technique.

Bibliography

[1] K.H. C Wagner, The stationary state of catalysts in homogeneous reactions, Elektrochem. 33 (1938) 172.

[2] W.H. Brattain, J. Bardeen, Surface Properties of Germanium, Bell Syst. Tech. J. 32 (1953) 1–41. https://doi.org/10.1002/j.1538-7305.1953.tb01420.x.

[3] Adam Bielański and Jerzy Dereń and Jerzy Haber, Electric Conductivity and Catalytic Activity of Semiconducting Oxide Catalysts, Nature. 179 (1957) 668-669}.

[4] T. Seiyama, A. Kato, K. Fujiishi, M. Nagatani, A New Detector for Gaseous Components Using Semiconductive Thin Films., Anal. Chem. 34 (1962) 1502–1503. https://doi.org/10.1021/ac60191a001.

[5] M. Seiyama, T., Kato, A., Fujiishi, K., & Nagatani, A new detector for gaseous components using semiconductive thin films, Anal. Chem. 34 (1962) 1502–1503.

[6] Naoyoshi Taguchi, Gas-detecting device, US3631436A, 1971.

[7] G. Sakai, N. Matsunaga, K. Shimanoe, N. Yamazoe, Theory of gas-diffusion controlled sensitivity for thin film semiconductor gas sensor, Sensors Actuators B Chem. 80 (2001) 125–131. https://doi.org/10.1016/S0925-4005(01)00890-5.

[8] G. Neri, First Fifty Years of Chemoresistive Gas Sensors, Chemosensors. 3 (2015) 1–20. https://doi.org/10.3390/chemosensors3010001.

[9] EH40/96 Occupational Exposure Limits., in: Heal. Saf. Exec., London, 1996.

[10] D. Briand, J. Courbat, Micromachined semiconductor gas sensors, in: Semicond. Gas Sensors, Elsevier, 2013: pp. 220–260. https://doi.org/10.1533/9780857098665.2.220.

[11] N. BARSAN, D. KOZIEJ, U. WEIMAR, Metal oxide-based gas sensor research: How to?, Sensors Actuators B Chem. 121 (2007) 18–35. https://doi.org/10.1016/j.snb.2006.09.047.

[12] E. Spagnoli, B. Fabbri, A. Gaiardo, M. Valt, M. Ardit, S. Krik, G. Cruciani, M. Della Ciana, L. Vanzetti, G. Vola, F. Di Benedetto, A. Migliori, C. Malagù, V. Guidi, Design of a metal-oxide solid solution for selective detection of ethanol with marginal influence by humidity, Sensors Actuators B Chem. 370 (2022) 132426. https://doi.org/10.1016/j.snb.2022.132426.

[13] A. Hulanicki, S. Glab, F. Ingman, Chemical sensors definitions and classification, Pure Appl. Chem. 63 (1991) 1247–1250. https://doi.org/10.1351/pac199163091247.

[14] E. Fazio, S. Spadaro, C. Corsaro, G. Neri, S.G. Leonardi, F. Neri, N. Lavanya, C. Sekar, N. Donato, G. Neri, Metal-oxide based nanomaterials: Synthesis, characterization and their applications in electrical and electrochemical sensors, Sensors. 21 (2021) 1–33. https://doi.org/10.3390/s21072494.

[15] N. Sato, Electrochemistry at Metal and Semiconductor Electrodes, 1st ed., Elsevier, 1998. https://doi.org/10.1016/B978-0-444-82806-4.X5000-4.

[16] M.J. Madou, S.R. Morrison, Chemical Sensing with Solid State Devices, Elsevier, 1989. https://doi.org/10.1016/C2009-0-22258-6.

[17] W. U. Barsan, N., Conduction model of metal oxide gas sensors, J. Electroceramics, J. Electroceramics. 7 (2001) 143–167. https://doi.org/10.1023/A:1014405811371.

[18] ISO [International Organization for Standardization], Determination of the specific surface area of solids by gas adsorption - BET method (ISO 9277:2010(E)), Ref. Number ISO. 9277 (2010) 30 pp. www.iso.org.

[19] M. Tiemann, Porous Metal Oxides as Gas Sensors, Chem. - A Eur. J. 13 (2007) 8376–8388. https://doi.org/10.1002/chem.200700927.

[20] T. Wagner, S. Haffer, C. Weinberger, D. Klaus, M. Tiemann, Mesoporous materials as gas sensors, Chem. Soc. Rev. 42 (2013) 4036–4053. https://doi.org/10.1039/c2cs35379b.

[21] Y. Guo, X. He, W. Huang, M. Wang, Microstructure Effects on Effective Gas Diffusion Coefficient of Nanoporous Materials, Transp. Porous Media. 126 (2019) 431–453. https://doi.org/10.1007/s11242-018-1165-4.

[22] W.G. Pollard, R.D. Present, On Gaseous Self-Diffusion in Long Capillary Tubes, Phys. Rev. 73 (1948) 762–774. https://doi.org/10.1103/PhysRev.73.762.

[23] R. Krishna, J.M. van Baten, Investigating the validity of the Bosanquet formula for estimation of diffusivities in mesopores, Chem. Eng. Sci. 69 (2012) 684–688. https://doi.org/10.1016/j.ces.2011.11.026.

[24] S.J. Blundell, K.M. Blundell, Concepts in Thermal Physics, Oxford University PressOxford, 2009. https://doi.org/10.1093/acprof:oso/9780199562091.001.0001.

[25] C.O. Park, S.A. Akbar, Ceramics for chemical sensing, J. Mater. Sci. 38 (2003) 4611–4637. https://doi.org/10.1023/A:1027402430153.

[26] N. Barsan, J. Rebholz, U. Weimar, Conduction mechanism switch for SnO_2 based sensors during operation in application relevant conditions; implications for modeling of sensing, Sensors Actuators B Chem. 207 (2015) 455–459. https://doi.org/10.1016/j.snb.2014.10.016.

[27] D. Kohl, Surface processes in the detection of reducing gases with SnO_2-based devices, Sensors and Actuators. 18 (1989) 71–113. https://doi.org/10.1016/0250-6874(89)87026-X.

[28] A. Gurlo, Interplay between O_2 and SnO_2: Oxygen Ionosorption and Spectroscopic Evidence for Adsorbed Oxygen, ChemPhysChem. 7 (2006) 2041–2052. https://doi.org/10.1002/cphc.200600292.

[29] E. Spagnoli, A. Gaiardo, B. Fabbri, M. Valt, S. Krik, M. Ardit, G. Cruciani, M. Della Ciana, L. Vanzetti, G. Vola, S. Gherardi, P. Bellutti, C. Malagù, V. Guidi, Design of a Metal-Oxide Solid Solution for Sub-ppm H_2 Detection, ACS Sensors. 7 (2022) 573–583. https://doi.org/10.1021/acssensors.1c02481.

[30] A. Staerz, U. Weimar, N. Barsan, Current state of knowledge on the metal oxide based gas sensing mechanism, Sensors Actuators B Chem. 358 (2022) 131531. https://doi.org/10.1016/j.snb.2022.131531.

[31] S.R. Morrison, The Chemical Physics of Surfaces, Springer US, Boston, MA, 1977. https://doi.org/10.1007/978-1-4615-8007-2.

[32] D. Degler, B. Junker, F. Allmendinger, U. Weimar, N. Barsan, Investigations on the temperature-dependent interaction of water vapor with tin dioxide and its implications on gas sensing, ACS Sensors. 5 (2020) 3207–3216. https://doi.org/10.1021/acssensors.0c01493.

[33] I. Boehme, U. Weimar, N. Barsan, Unraveling the Surface Chemistry of CO Sensing with In_2O_3 Based Gas Sensors, Sensors Actuators, B Chem. 326 (2021) 129004. https://doi.org/10.1016/j.snb.2020.129004.

[34] K. Khamfoo, A. Staerz, M. Boepple, A. Wisitsoraat, C. Liewhiran, U. Weimar, N. Barsan, Operando DRIFT measurements on flame-spray-made Zn_2SnO_4 nanoparticles based environmental sensors, Sensors Actuators B Chem. 371 (2022) 132495. https://doi.org/10.1016/j.snb.2022.132495.

[35] G. Korotcenkov, The role of morphology and crystallographic structure of metal oxides in response of conductometric-type gas sensors, Mater. Sci. Eng. R Reports. 61 (2008) 1–39. https://doi.org/10.1016/j.mser.2008.02.001.

[36] G. Korotcenkov, V. Brinzari, J.R. Stetter, I. Blinov, V. Blaja, The nature of processes controlling the kinetics of indium oxide-based thin film gas sensor response, Sensors Actuators B Chem. 128 (2007) 51–63. https://doi.org/10.1016/j.snb.2007.05.028.

[37] S.R. Morrison, Selectivity in semiconductor gas sensors, Sensors and Actuators. 12 (1987) 425–440. https://doi.org/10.1016/0250-6874(87)80061-6.

[38] N. Yamazoe, New approaches for improving semiconductor gas sensors, Sensors Actuators B Chem. 5 (1991) 7–19. https://doi.org/10.1016/0925-4005(91)80213-4.

[39] N. Yamazoe, Y. Kurokawa, T. Seiyama, Effects of additives on semiconductor gas sensors, Sensors and Actuators. 4 (1983) 283–289. https://doi.org/10.1016/0250-6874(83)85034-3.

[40] M. Hübner, D. Koziej, J.-D. Grunwaldt, U. Weimar, N. Barsan, An Au clusters related spill-over sensitization mechanism in SnO_2-based gas sensors identified by operando HERFD-XAS, work function changes, DC resistance and catalytic conversion studies, Phys. Chem. Chem. Phys. 14 (2012) 13249. https://doi.org/10.1039/c2cp41349c.

[41] A. Dey, Semiconductor metal oxide gas sensors: A review, Mater. Sci. Eng. B. 229 (2018) 206–217. https://doi.org/10.1016/j.mseb.2017.12.036.

[42] T. Lin, X. Lv, S. Li, Q. Wang, The Morphologies of the Semiconductor Oxides and Their Gas-Sensing Properties, Sensors. 17 (2017) 2779. https://doi.org/10.3390/s17122779.

[43] A. Oprea, D. Degler, N. Barsan, A. Hemeryck, J. Rebholz, Basics of semiconducting metal oxide–based gas sensors, in: Gas Sensors Based Conduct. Met. Oxides, Elsevier, 2019: pp. 61–165. https://doi.org/10.1016/B978-0-12-811224-3.00003-2.

[44] T. Liu, J. Liu, Q. Hao, Q. Liu, X. Jing, H. Zhang, G. Huang, J. Wang, Porous tungsten trioxide nanolamellae with uniform structures for high-performance ethanol sensing, CrystEngComm. 18 (2016) 8411–8418. https://doi.org/10.1039/c6ce01587e.

[45] S. Wei, S. Wang, Y. Zhang, M. Zhou, Different morphologies of ZnO and their ethanol sensing property, Sensors Actuators B Chem. 192 (2014) 480–487. https://doi.org/10.1016/j.snb.2013.11.034.

[46] A. Ponzoni, C. Baratto, N. Cattabiani, M. Falasconi, V. Galstyan, E. Nunez-Carmona, F. Rigoni, V. Sberveglieri, G. Zambotti, D. Zappa, Metal Oxide Gas Sensors, a Survey of Selectivity Issues Addressed at the SENSOR Lab, Brescia (Italy), Sensors. 17 (2017) 714. https://doi.org/10.3390/s17040714.

[47] Gas Sensor Market worth $2.1 Billion by 2027, (2023). https://www.marketsandmarkets.com/PressReleases/gas-sensor.asp.

[48] C. Liewhiran, A. Camenzind, A. Teleki, S.E. Pratsinis, S. Phanichphant, High Performance Ethanol Sensor for Control Drunken Driving Based on Flame-made ZnO Nanoparticles, in: 2007 2nd IEEE Int. Conf. Nano/Micro Eng. Mol. Syst., IEEE, 2007: pp. 672–677. https://doi.org/10.1109/NEMS.2007.352108.

[49] Y. Xia, A. Pan, D.W. Gardner, S. Zhao, A.K. Davey, Z. Li, L. Zhao, C. Carraro, R. Maboudian, Well-connected ZnO nanoparticle network fabricated by in-situ annealing of ZIF-8 for enhanced sensitivity in gas sensing application, Sensors Actuators B Chem. 344 (2021) 130180. https://doi.org/10.1016/j.snb.2021.130180.

[50] M. Peris, L. Escuder-Gilabert, On-line monitoring of food fermentation processes using electronic noses and electronic tongues: A review, Anal. Chim. Acta. 804 (2013) 29–36. https://doi.org/10.1016/j.aca.2013.09.048.

[51] M.O. Petinrin, M.B. Adebayo, A.T. Adelowokan, A Review on Hydrogen as a Fuel for Automotive Application, Int. J. Energy Eng. 4 (2014) 75–80. https://doi.org/10.5923/j.ijee.20140404.02.

[52] A. Zappi, R. Hernandez, W.E. Holmes, A review of hydrogen production from anaerobic digestion, Int. J. Environ. Sci. Technol. 18 (2021) 4075–4090. https://doi.org/10.1007/s13762-020-03117-w.

[53] P.S. Chauhan, S. Bhattacharya, Hydrogen gas sensing methods, materials, and approach to achieve parts per billion level detection: A review, Int. J. Hydrogen Energy. 44 (2019) 26076–26099. https://doi.org/10.1016/j.ijhydene.2019.08.052.

[54] N. Lavanya, C. Sekar, E. Fazio, F. Neri, S.G. Leonardi, G. Neri, Development of a selective hydrogen leak sensor based on chemically doped SnO_2 for automotive applications, Int. J. Hydrogen Energy. 42 (2017) 10645–10655. https://doi.org/10.1016/j.ijhydene.2017.03.027.

[55] Z. Wang, L. Zhu, J. Liu, J. Wang, W. Yan, Gas Sensing Technology for the Detection and Early Warning of Battery Thermal Runaway: A Review, Energy and Fuels. 36 (2022) 6038–6057. https://doi.org/10.1021/acs.energyfuels.2c01121.

[56] C. Essl, L. Seifert, M. Rabe, A. Fuchs, Early Detection of Failing Automotive Batteries Using Gas Sensors, Batteries. 7 (2021) 25. https://doi.org/10.3390/batteries7020025.

[57] O. Lupan, N. Ababii, A.K. Mishra, M.T. Bodduluri, N. Magariu, A. Vahl, H. Krüger, B. Wagner, F. Faupel, R. Adelung, N.H. de Leeuw, S. Hansen, Heterostructure-based devices with enhanced humidity stability for H_2 gas sensing applications in breath tests and portable batteries, Sensors Actuators, A Phys. 329 (2021). https://doi.org/10.1016/j.sna.2021.112804.

[58] S.V. Rana, A. Malik, Hydrogen breath tests in gastrointestinal diseases, Indian J. Clin. Biochem. 29 (2014) 398–405. https://doi.org/10.1007/s12291-014-0426-4.

[59] R. Khoshini, S.C. Dai, S. Lezcano, M. Pimentel, A systematic review of diagnostic tests for small intestinal bacterial overgrowth, Dig. Dis. Sci. 53 (2008) 1443–1454. https://doi.org/10.1007/s10620-007-0065-1.

[60] B.T. Massey, A. Wald, Small Intestinal Bacterial Overgrowth Syndrome: A Guide for the Appropriate Use of Breath Testing, Dig. Dis. Sci. 66 (2021) 338–347. https://doi.org/10.1007/s10620-020-06623-6.

[61] A. Staerz, U. Weimar, N. Barsan, Understanding the Potential of WO_3 Based Sensors for Breath Analysis, Sensors. 16 (2016) 1815. https://doi.org/10.3390/s16111815.

[62] T. Vogt, P.M. Woodward, B.A. Hunter, The High-Temperature Phases of WO_3, J. Solid State Chem. 144 (1999) 209–215. https://doi.org/10.1006/jssc.1999.8173.

[63] B. Gerand, G. Nowogrocki, J. Guenot, M. Figlarz, Structural study of a new hexagonal form of tungsten trioxide, J. Solid State Chem. 29 (1979) 429–434. https://doi.org/10.1016/0022-4596(79)90199-3.

[64] X. Han, X. Han, L. Li, C. Wang, Controlling the morphologies of WO_3 particles and tuning the gas sensing properties, New J. Chem. 36 (2012) 2205–2208. https://doi.org/10.1039/c2nj40600d.

[65] J. Su, X. Feng, J.D. Sloppy, L. Guo, C.A. Grimes, Vertically aligned WO_3 nanowire arrays grown directly on transparent conducting oxide coated glass: Synthesis and photoelectrochemical properties, Nano Lett. 11 (2011) 203–208. https://doi.org/10.1021/nl1034573.

[66] C. Dong, R. Zhao, L. Yao, Y. Ran, X. Zhang, Y. Wang, A review on WO_3 based gas sensors: Morphology control and enhanced sensing properties, J. Alloys Compd. 820 (2020). https://doi.org/10.1016/j.jallcom.2019.153194.

[67] Z. Wang, X. Zhou, Z. Li, Y. Zhuo, Y. Gao, Q. Yang, X. Li, G. Lu, Monodisperse WO_3 hierarchical spheres synthesized via a microwave assisted hydrothermal method: time dependent morphologies and gas sensing characterization, RSC Adv. 4 (2014) 23281. https://doi.org/10.1039/c4ra01946f.

[68] Y. Yao, M. Yin, J. Yan, S. (Frank) Liu, P-type sub-tungsten-oxide based urchin-like nanostructure for superior room temperature alcohol sensor, Appl. Surf. Sci. 441 (2018) 277–284. https://doi.org/10.1016/j.apsusc.2018.02.004.

[69] L. You, X. He, D. Wang, P. Sun, Y.F. Sun, X.S. Liang, Y. Du, G.Y. Lu, Ultrasensitive and low operating temperature NO2 gas sensor using nanosheets assembled hierarchical WO_3 hollow microspheres, Sensors Actuators B Chem. 173 (2012) 426–432. https://doi.org/10.1016/j.snb.2012.07.029.

[70] Y. Qin, F. Wang, W. Shen, M. Hu, Mesoporous three-dimensional network of crystalline WO_3 nanowires for gas sensing application, J. Alloys Compd. 540 (2012) 21–26. https://doi.org/10.1016/j.jallcom.2012.06.058.

[71] X. Zheng, C. Zhang, J. Xia, G. Zhou, D. Jiang, S. Wang, X. Li, Y. Shen, M. Dai, B. Wang, Q. Li, Mesoporous tungsten oxide electrodes for YSZ-based mixed potential sensors to detect NO_2 in the sub ppm-range, Sensors Actuators B Chem. 284 (2019) 575–581. https://doi.org/10.1016/j.snb.2019.01.016.

[72] Y. Wang, B. Zhang, J. Liu, Q. Yang, X. Cui, Y. Gao, X. Chuai, F. Liu, P. Sun, X. Liang, Y. Sun, G. Lu, Au-loaded mesoporous WO_3: Preparation and n-butanol sensing performances, Sensors Actuators B Chem. 236 (2016) 67–76. https://doi.org/10.1016/j.snb.2016.05.097.

[73] Y. Wang, J. Liu, X. Cui, Y. Gao, J. Ma, Y. Sun, P. Sun, F. Liu, X. Liang, T. Zhang, G. Lu, NH3 gas sensing performance enhanced by Pt-loaded on mesoporous WO_3, Sensors Actuators B Chem. 238 (2017) 473–481. https://doi.org/10.1016/j.snb.2016.07.085.

[74] Y. Li, W. Luo, N. Qin, J. Dong, J. Wei, W. Li, S. Feng, J. Chen, J. Xu, A.A. Elzatahry, M.H. Es-Saheb, Y. Deng, D. Zhao, Highly Ordered Mesoporous Tungsten Oxides with a Large Pore Size and Crystalline Framework for H_2S Sensing, Angew. Chemie Int. Ed. 53 (2014) 9035–9040. https://doi.org/10.1002/anie.201403817.

[75] Y. Li, X. Zhou, W. Luo, X. Cheng, Y. Zhu, A.M. El-Toni, A. Khan, Y. Deng, D. Zhao, Pore Engineering of Mesoporous Tungsten Oxides for Ultrasensitive Gas Sensing, Adv. Mater. Interfaces. 6 (2019) 1801269. https://doi.org/10.1002/admi.201801269.

[76] C. Wang, M. Ding, X. Kou, L. Guo, C. Feng, X. Li, H. Zhang, P. Sun, Y. Sun, G. Lu, Detection of nitrogen dioxide down to ppb levels using flower-like tungsten oxide nanostructures under different annealing temperatures, J. Colloid Interface Sci. 483 (2016) 314–320. https://doi.org/10.1016/j.jcis.2016.08.050.

[77] B. Xiao, Q. Zhao, C. Xiao, T. Yang, P. Wang, F. Wang, X. Chen, M. Zhang, Low-temperature solvothermal synthesis of hierarchical flower-like WO_3 nanostructures and their sensing properties for H 2 S, CrystEngComm. 17 (2015) 5710–5716. https://doi.org/10.1039/C5CE00870K.

[78] Y. Zhang, W. Zeng, Y. Li, NO2 and H2 sensing properties for urchin-like hexagonal WO_3 based on experimental and first-principle investigations, Ceram. Int. 45 (2019) 6043–6050. https://doi.org/10.1016/j.ceramint.2018.12.075.

[79] Z. Jin, P. Hu, W. Xu, J. Zhou, W. Guo, Y. Chen, C. Qiu, Hydrothermal synthesis and gas sensing properties of hybrid WO3 nano-materials using octadecylamine, J. Alloys Compd. 785 (2019) 1047–1055. https://doi.org/10.1016/j.jallcom.2019.01.248.

[80] D. Nunes, A. Pimentel, L. Santos, P. Barquinha, L. Pereira, E. Fortunato, R. Martins, Synthesis, design, and morphology of metal oxide nanostructures, in: Met. Oxide Nanostructures, Elsevier, 2019: pp. 21–57. https://doi.org/10.1016/B978-0-12-811512-1.00002-3.

[81] A. Tricoli, M. Righettoni, S.E. Pratsinis, Minimal cross-sensitivity to humidity during ethanol detection by SnO_2 –TiO_2 solid solutions, Nanotechnology. 20 (2009) 315502. https://doi.org/10.1088/0957-4484/20/31/315502.

[82] D. GARCIA, D. SPEIDEL, Reexamination of the System TiO_2-SnO_2, J. Am. Ceram. Soc. 55 (1972) 322–322. https://doi.org/10.1111/j.1151-2916.1972.tb11295.x.

[83] M.C. Carotta, A. Cervi, S. Gherardi, V. Guidi, C. Malagu', G. Martinelli, B. Vendemiati, M. Sacerdoti, G. Ghiotti, S. Morandi, S. Lettieri, P. Maddalena, A. Setaro, (Ti, Sn)O_2 solid solutions for gas sensing: A systematic approach by different techniques for different calcination temperature and molar composition, Sensors Actuators B Chem. 139 (2009) 329–339. https://doi.org/10.1016/j.snb.2009.03.025.

[84] T. Hirata, Oxygen Position, Octahedral Distortion, and Bond-Valence Parameter from Bond Lengths in $Ti_{1-x}Sn_xO_2$ ($0 \leq x \leq 1$), J. Am. Ceram. Soc. 83 (2000) 3205–3207. https://doi.org/10.1111/j.1151-2916.2000.tb01706.x.

[85] M.C. Carotta, M. Ferroni, V. Guidi, G. Martinelli, Preparation and Characterization of Nanostructured Titania Thick Films, Adv. Mater. 11 (1999) 943–946. https://doi.org/10.1002/(SICI)1521-4095(199908)11:11<943::AID-ADMA943>3.3.CO;2-C.

[86] M. Ferroni, M.. Carotta, V. Guidi, G. Martinelli, F. Ronconi, O. Richard, D. Van Dyck, J. Van Landuyt, Structural characterization of Nb–TiO_2 nanosized thick-films for gas sensing application, Sensors Actuators B Chem. 68 (2000) 140–145. https://doi.org/10.1016/S0925-4005(00)00474-3.

[87] V. Guidi, M.C. Carotta, M. Ferroni, G. Martinelli, M. Sacerdoti, Effect of Dopants on Grain Coalescence and Oxygen Mobility in Nanostructured Titania Anatase and Rutile, J. Phys. Chem. B. 107 (2003) 120–124. https://doi.org/10.1021/jp013572u.

[88] D. Smyth, The effects of dopants on the properties of metal oxides, Solid State Ionics. 129 (2000) 5–12. https://doi.org/10.1016/S0167-2738(99)00312-4.

[89] M.C. Carotta, M. Benetti, V. Guidi, S. Gherardi, C. Malagu', B. Vendemiati, G. Martinelli, Nanostructured (Sn,Ti, Nb)O_2 Solid Solution for Hydrogen Sensing, MRS Proc. 915 (2006) 0915-R07-10. https://doi.org/10.1557/PROC-0915-R07-10.

[90] E. Spagnoli, S. Krik, B. Fabbri, M. Valt, M. Ardit, A. Gaiardo, L. Vanzetti, M. Della Ciana, V. Cristino, G. Vola, S. Caramori, C. Malagù, V. Guidi, Development and characterization of WO_3 nanoflakes for selective ethanol sensing, Sensors Actuators B Chem. 347 (2021) 130593.

https://doi.org/10.1016/j.snb.2021.130593.

[91] D. Ma, H. Wang, Q. Zhang, Y. Li, Self-weaving WO_3 nanoflake films with greatly enhanced electrochromic performance, J. Mater. Chem. 22 (2012) 16633. https://doi.org/10.1039/c2jm32784h.

[92] W. Li, P. Da, Y. Zhang, Y. Wang, X. Lin, X. Gong, G. Zheng, WO_3 Nanoflakes for Enhanced Photoelectrochemical Conversion, ACS Nano. 8 (2014) 11770–11777. https://doi.org/10.1021/nn5053684.

[93] M.C. Carotta, A. Fioravanti, S. Gherardi, C. Malagù, M. Sacerdoti, G. Ghiotti, S. Morandi, (Ti,Sn) solid solutions as functional materials for gas sensing, Sensors Actuators B Chem. 194 (2014) 195–205. https://doi.org/10.1016/j.snb.2013.12.021.

[94] S. Mourdikoudis, R.M. Pallares, N.T.K. Thanh, Characterization techniques for nanoparticles: comparison and complementarity upon studying nanoparticle properties, Nanoscale. 10 (2018) 12871–12934. https://doi.org/10.1039/C8NR02278J.

[95] Fred A. Stevie and Carrie L. Donley, Introduction to x-ray photoelectron spectroscopy, J. Vac. Sci. Technol. A. 38 (2020) 063204. https://doi.org/10.1116/6.0000412.

[96] G. Speranza, R. Canteri, RxpsG a new open project for Photoelectron and Electron Spectroscopy data processing, SoftwareX. 10 (2019) 100282. https://doi.org/10.1016/j.softx.2019.100282.

[97] P. Makuła, M. Pacia, W. Macyk, How To Correctly Determine the Band Gap Energy of Modified Semiconductor Photocatalysts Based on UV–Vis Spectra, J. Phys. Chem. Lett. 9 (2018) 6814–6817. https://doi.org/10.1021/acs.jpclett.8b02892.

[98] M. LATINO, G. NERI, Chemoresistive metal oxide gas sensor: working principles and applications, AAPP Atti Della Accad. Peloritana Dei Pericolanti, Cl. Di Sci. Fis. Mat. e Nat. 99 (2021) 1–16. https://doi.org/10.1478/AAPP.99S1A41.

[99] Y. Gao, J. Feng, F. Liu, Z. Liu, Effects of Organic Vehicle on the Rheological and Screen-Printing Characteristics of Silver Paste for LTCC Thick Film Electrodes, Materials (Basel). 15 (2022) 1953. https://doi.org/10.3390/ma15051953.

[100] J.M. Chalmers, P.R. Griffiths, eds., Handbook of Vibrational Spectroscopy, John Wiley & Sons, Ltd, Chichester, UK, 2001. https://doi.org/10.1002/0470027320.

[101] B.H. Stuart, Infrared Spectroscopy: Fundamentals and Applications, Wiley, 2004. https://doi.org/10.1002/0470011149.

[102] P.R. Griffiths, J.A. de Haseth, Fourier Transform Infrared Spectrometry, John Wiley & Sons, Inc., Hoboken, NJ, USA, 2007. https://doi.org/10.1002/047010631X.

[103] T. Petit, L. Puskar, FTIR spectroscopy of nanodiamonds: Methods and interpretation, Diam. Relat. Mater. 89 (2018) 52–66. https://doi.org/10.1016/j.diamond.2018.08.005.

[104] S. Emiroglu, N. Bârsan, U. Weimar, V. Hoffmann, In situ diffuse reflectance infrared spectroscopy study of CO adsorption on SnO_2, Thin Solid Films. 391 (2001) 176–185. https://doi.org/10.1016/S0040-6090(01)00979-8.

[105] R.M. Rioux, J.D. Hoefelmeyer, M. Grass, H. Song, K. Niesz, P. Yang, G.A. Somorjai, Adsorption and Co-adsorption of Ethylene and Carbon Monoxide on Silica-Supported Monodisperse Pt Nanoparticles: Volumetric Adsorption and Infrared Spectroscopy Studies, Langmuir. 24 (2008) 198–207. https://doi.org/10.1021/la702685a.

[106] M.A. Newton, M. Di Michiel, A. Kubacka, M. Fernández-García, Combining Time-Resolved Hard X-ray Diffraction and Diffuse Reflectance Infrared Spectroscopy To Illuminate CO Dissociation and Transient Carbon Storage by Supported Pd Nanoparticles during CO/NO Cycling, J. Am. Chem. Soc. 132 (2010) 4540–4541. https://doi.org/10.1021/ja9107512.

[107] H. Sheng, H. Zhang, W. Song, H. Ji, W. Ma, C. Chen, J. Zhao, Activation of Water in Titanium Dioxide Photocatalysis by Formation of Surface Hydrogen Bonds: An In Situ IR Spectroscopy Study, Angew. Chemie Int. Ed. 54 (2015) 5905–5909. https://doi.org/10.1002/anie.201412035.

[108] D.J. Cumming, C. Tumilson, S.F.R. Taylor, S. Chansai, A. V. Call, J. Jacquemin, C. Hardacre, R.H. Elder, Development of a diffuse reflectance infrared fourier transform spectroscopy (DRIFTS) cell for the in situ analysis of co-electrolysis in a solid oxide cell, Faraday Discuss. 182 (2015) 97–111. https://doi.org/10.1039/C5FD00030K.

[109] M. Valt, M. Della Ciana, B. Fabbri, D. Sali, A. Gaiardo, V. Guidi, Design and validation of a novel operando spectroscopy reaction chamber for chemoresistive gas sensors, Sensors Actuators B Chem. 341 (2021) 130012. https://doi.org/10.1016/j.snb.2021.130012.

[110] M. Della Ciana, M. Valt, B. Fabbri, A. Gaiardo, E. Spagnoli, S. Krik, P. Bernardoni, N. Gilli, A. Migliori, A. Quaranta, V. Morandi, V. Guidi, SO_2 sensing mechanism of nanostructured SiC-SiO_xC core shell: An operando DRIFT investigation, Sensors Actuators B Chem. 371 (2022) 132497. https://doi.org/10.1016/j.snb.2022.132497.

[111] S. Wicker, M. Guiltat, U. Weimar, A. Hémeryck, N. Barsan, Ambient Humidity Influence on CO Detection with SnO_2 Gas Sensing Materials. A Combined DRIFTS/DFT Investigation, J. Phys. Chem. C. 121 (2017) 25064–25073. https://doi.org/10.1021/acs.jpcc.7b06253.

[112] P.M. Woodward, A.W. Sleight, T. Vogt, Structure refinement of triclinic tungsten trioxide, J. Phys. Chem. Solids. 56 (1995) 1305–1315. https://doi.org/10.1016/0022-3697(95)00063-1.

[113] J. Oi, A. Kishimoto, T. Kudo, M. Hiratani, Hexagonal tungsten trioxide obtained from peroxo-polytungstate and reversible lithium electro-intercalation into its framework, J. Solid State Chem. 96 (1992) 13–19. https://doi.org/10.1016/S0022-4596(05)80292-0.

[114] A. Martínez-de la Cruz, D.S. Martínez, E.L. Cuéllar, Synthesis and characterization of WO_3 nanoparticles prepared by the precipitation method: Evaluation of photocatalytic activity under vis-irradiation, Solid State Sci. 12 (2010) 88–94. https://doi.org/10.1016/j.solidstatesciences.2009.10.010.

[115] S.S. Kalanur, Structural, Optical, Band Edge and Enhanced Photoelectrochemical Water Splitting Properties of Tin-Doped WO_3, Catalysts. 9 (2019) 456. https://doi.org/10.3390/catal9050456.

[116] F. Amano, D. Li, B. Ohtani, Fabrication and photoelectrochemical property of tungsten(vi) oxide films with a flake-wall structure, Chem. Commun. 46 (2010) 2769. https://doi.org/10.1039/b926931b.

[117] A. Gaiardo, G. Zonta, S. Gherardi, C. Malagù, B. Fabbri, M. Valt, L. Vanzetti, N. Landini, D. Casotti, G. Cruciani, M. Della Ciana, V. Guidi, Nanostructured $SmFeO_3$ Gas Sensors: Investigation of the Gas Sensing Performance Reproducibility for Colorectal Cancer Screening, Sensors. 20 (2020) 5910. https://doi.org/10.3390/s20205910.

[118] M. Vasilopoulou, A. Soultati, D.G. Georgiadou, T. Stergiopoulos, L.C. Palilis, S. Kennou, N.A. Stathopoulos, D. Davazoglou, P. Argitis, Hydrogenated under-stoichiometric tungsten oxide anode interlayers for efficient and stable organic photovoltaics, J. Mater. Chem. A. 2 (2014) 1738–1749. https://doi.org/10.1039/C3TA13975A.

[119] D. Barreca, G. Carta, A. Gasparotto, G. Rossetto, E. Tondello, P. Zanella, A Study of Nanophase Tungsten Oxides Thin Films by XPS, Surf. Sci. Spectra. 8 (2001) 258–267. https://doi.org/10.1116/11.20020801.

[120] Q. Liu, F. Wang, H. Lin, Y. Xie, N. Tong, J. Lin, X. Zhang, Z. Zhang, X. Wang, Surface oxygen vacancy and defect engineering of WO_3 for improved visible light photocatalytic performance, Catal. Sci. Technol. 8 (2018) 4399–4406. https://doi.org/10.1039/C8CY00994E.

[121] X. Zheng, F. Ren, S. Zhang, X. Zhang, H. Wu, X. Zhang, Z. Xing, W. Qin, Y. Liu, C. Jiang, A General Method for Large-Scale Fabrication of Semiconducting Oxides with High SERS Sensitivity, ACS Appl. Mater. Interfaces. 9 (2017) 14534–14544. https://doi.org/10.1021/acsami.7b03839.

[122] C.J. Howard, T.M. Sabine, F. Dickson, Structural and thermal parameters for rutile and anatase, Acta Crystallogr. Sect. B Struct. Sci. 47 (1991) 462–468. https://doi.org/10.1107/S010876819100335X.

[123] T. Yamanaka, R. Kurashima, J. Mimaki, X-ray diffraction study of bond character of rutile-type SiO_2 , GeO_2 and SnO_2, Zeitschrift Für Krist. - Cryst. Mater. 215 (2000) 424–428. https://doi.org/10.1524/zkri.2000.215.7.424.

[124] R.D. Shannon, Revised effective ionic radii and systematic studies of interatomic distances in halides and chalcogenides, Acta Crystallogr. Sect. A. 32 (1976) 751–767. https://doi.org/10.1107/S0567739476001551.

[125] W. Jung, H.L. Tuller, Investigation of surface Sr segregation in model thin film solid oxidefuel cell perovskite electrodes, Energy Environ. Sci. 5 (2012) 5370–5378. https://doi.org/10.1039/C1EE02762J.

[126] I. Hamada, A. Uozumi, Y. Morikawa, A. Yanase, H. Katayama-Yoshida, A Density Functional Theory Study of Self-Regenerating Catalysts $LaFe_{1-x}M_xO_{3-y}$ (M = Pd, Rh, Pt), J. Am. Chem. Soc. 133 (2011) 18506–18509. https://doi.org/10.1021/ja110302t.

[127] A.M. Ruiz, G. Dezanneau, J. Arbiol, A. Cornet, J.R. Morante, Insights into the Structural and Chemical Modifications of Nb Additive on TiO_2 Nanoparticles, Chem. Mater. 16 (2004) 862–871. https://doi.org/10.1021/cm0351238.

[128] X. Pan, M.-Q. Yang, X. Fu, N. Zhang, Y.-J. Xu, Defective TiO_2 with oxygen vacancies: synthesis, properties and photocatalytic applications, Nanoscale. 5 (2013) 3601. https://doi.org/10.1039/c3nr00476g.

[129] Q. Chen, Nb_2O_5 improved photoluminescence, magnetic and Faraday rotation properties of magneto-optical glasses, J. Non. Cryst. Solids. 519 (2019) 119451. https://doi.org/10.1016/j.jnoncrysol.2019.05.027.

[130] U. Farva, J. Kim, Growth temperature-dependent morphological, optical, and electrical study of SnO_2 thin film by atomic layer deposition, Mater. Chem. Phys. 267 (2021) 124584. https://doi.org/10.1016/j.matchemphys.2021.124584.

[131] Y. Xu, S. Wu, P. Wan, J. Sun, Z.D. Hood, Introducing Ti^{3+} defects based on lattice distortion for enhanced visible light photoreactivity in TiO_2 microspheres, RSC Adv. 7 (2017) 32461–32467. https://doi.org/10.1039/C7RA04885H.

[132] C. Di Valentin, G. Pacchioni, A. Selloni, Reduced and n-Type Doped TiO_2 : Nature of Ti^{3+} Species, J. Phys. Chem. C. 113 (2009) 20543–20552. https://doi.org/10.1021/jp9061797.

[133] B.A. Goodman, J.B. Raynor, Electron Spin Resonance of Transition Metal Complexes, in: 1970: pp. 135–362. https://doi.org/10.1016/S0065-2792(08)60336-2.

[134] M.C. Carotta, S. Gherardi, V. Guidi, C. Malagù, G. Martinelli, B. Vendemiati, M. Sacerdoti, G. Ghiotti, S. Morandi, Electrical and spectroscopic properties of $Ti_{0.2}Sn_{0.8}O_2$ solid solution for gas sensing, Thin Solid Films. 517 (2009) 6176–6183. https://doi.org/10.1016/j.tsf.2009.04.002.

[135] L. Kong, C. Wang, H. Zheng, X. Zhang, Y. Liu, Defect-Induced Yellow Color in Nb-Doped TiO_2 and Its Impact on Visible-Light Photocatalysis, J. Phys. Chem. C. 119 (2015) 16623–16632. https://doi.org/10.1021/acs.jpcc.5b03448.

[136] D.Y. Lee, J.-H. Park, Y.-H. Kim, M.-H. Lee, N.-I. Cho, Effect of Nb doping on morphology, crystal structure, optical band gap energy of TiO_2 thin films, Curr. Appl. Phys. 14 (2014) 421–427. https://doi.org/10.1016/j.cap.2013.12.025.

[137] Y. Qu, H. Wang, H. Chen, M. Han, Z. Lin, Synthesis, characterization and sensing properties of mesoporous C/SnO_2 nanocomposite, Sensors Actuators B Chem. 228 (2016) 595–604. https://doi.org/10.1016/j.snb.2016.01.077.

[138] C. Song, C. Li, Y. Yin, J. Xiao, X. Zhang, M. Song, W. Dong, Preparation and gas sensing properties of partially broken WO_3 nanotubes, Vacuum. 114 (2015) 13–16. https://doi.org/10.1016/j.vacuum.2014.12.019.

[139] S. Wei, Y. Xing, Y. Li, Y. Zhao, W. Du, M. Zhou, Preparation and gas sensing properties of flower-like WO_3 hierarchical architecture, Vacuum. 129 (2016) 13–19. https://doi.org/10.1016/j.vacuum.2016.04.010.

[140] A. Staerz, S. Somacescu, M. Epifani, T. Kida, U. Weimar, N. Barsan, WO_3-Based Gas Sensors: Identifying Inherent Qualities and Understanding the Sensing Mechanism, ACS Sensors. 5 (2020) 1624–1633. https://doi.org/10.1021/acssensors.0c00113.

[141] A. Haryanto, S. Fernando, N. Murali, S. Adhikari, Current Status of Hydrogen Production Techniques by Steam Reforming of Ethanol: A Review, Energy & Fuels. 19 (2005) 2098–2106. https://doi.org/10.1021/ef0500538.

[142] Threshold Limit Value (TLV), in: Encycl. Biometrics, Springer US, Boston, MA, 2009: pp. 1333–1333. https://doi.org/10.1007/978-0-387-73003-5_533.

[143] Z. Wang, D. Wang, J. Sun, Controlled synthesis of defect-rich ultrathin two-dimensional WO_3 nanosheets for NO_2 gas detection, Sensors Actuators, B Chem. 245 (2017) 828–834. https://doi.org/10.1016/j.snb.2017.02.038.

[144] M. Epifani, E. Comini, R. Díaz, T. Andreu, A. Genç, J. Arbiol, P. Siciliano, G. Faglia, J.R. Morante, Solvothermal, Chloroalkoxide-based Synthesis of Monoclinic WO_3 Quantum Dots and Gas-Sensing Enhancement by Surface Oxygen Vacancies, ACS Appl. Mater. Interfaces. 6 (2014) 16808–16816. https://doi.org/10.1021/am504158r.

[145] A.J. Gardecka, G.K.L. Goh, G. Sankar, I.P. Parkin, On the nature of niobium substitution in niobium doped titania thin films by AACVD and its impact on electrical and optical properties, J. Mater. Chem. A. 3 (2015) 17755–17762. https://doi.org/10.1039/C5TA03772G.

[146] V. Lantto, P. Rompplainen, S. Leppävuori, A study of the temperature dependence of the barrier energy in porous tin dioxide, Sensors and Actuators. 14 (1988) 149–163. https://doi.org/10.1016/0250-6874(88)80062-3.

[147] J. Arbiol, J. Cerdà, G. Dezanneau, A. Cirera, F. Peiró, A. Cornet, J.R. Morante, Effects of Nb doping on the TiO_2 anatase-to-rutile phase transition, J. Appl. Phys. 92 (2002) 853–861. https://doi.org/10.1063/1.1487915.

[148] E. Uyanga, A. Gibaud, P. Daniel, D. Sangaa, G. Sevjidsuren, P. Altantsog, T. Beuvier, C.H.

Lee, A.M. Balagurov, Structural and vibrational investigations of Nb-doped TiO_2 thin films, Mater. Res. Bull. 60 (2014) 222–231. https://doi.org/10.1016/j.materresbull.2014.08.035.

[149] J. Huang, Q. Wan, Gas Sensors Based on Semiconducting Metal Oxide One-Dimensional Nanostructures, Sensors. 9 (2009) 9903–9924. https://doi.org/10.3390/s91209903.

[150] A. Gaiardo, B. Fabbri, V. Guidi, P. Bellutti, A. Giberti, S. Gherardi, L. Vanzetti, C. Malagù, G. Zonta, Metal Sulfides as Sensing Materials for Chemoresistive Gas Sensors, Sensors. 16 (2016) 296. https://doi.org/10.3390/s16030296.

[151] A. Gaiardo, B. Fabbri, A. Giberti, M. Valt, S. Gherardi, V. Guidi, C. Malagù, P. Bellutti, G. Pepponi, D. Casotti, G. Cruciani, G. Zonta, N. Landini, M. Barozzi, S. Morandi, L. Vanzetti, R. Canteri, M. Della Ciana, A. Migliori, E. Demenev, Tunable formation of nanostructured SiC/SiOC core-shell for selective detection of SO_2, Sensors Actuators B Chem. 305 (2020) 127485. https://doi.org/10.1016/j.snb.2019.127485.

[152] M. Valt, M. Caporali, B. Fabbri, A. Gaiardo, S. Krik, E. Iacob, L. Vanzetti, C. Malagù, M. Banchelli, C. D'Andrea, M. Serrano-Ruiz, M. Vanni, M. Peruzzini, V. Guidi, Air Stable Nickel-Decorated Black Phosphorus and Its Room-Temperature Chemiresistive Gas Sensor Capabilities, ACS Appl. Mater. Interfaces. 13 (2021) 44711–44722. https://doi.org/10.1021/acsami.1c10763.

[153] N.-H. Kim, S.-J. Choi, D.-J. Yang, J. Bae, J. Park, I.-D. Kim, Highly sensitive and selective hydrogen sulfide and toluene sensors using Pd functionalized WO_3 nanofibers for potential diagnosis of halitosis and lung cancer, Sensors Actuators B Chem. 193 (2014) 574–581. https://doi.org/10.1016/j.snb.2013.12.011.

[154] T. Hibbard, A.J. Killard, Breath Ammonia Analysis: Clinical Application and Measurement, Crit. Rev. Anal. Chem. 41 (2011) 21–35. https://doi.org/10.1080/10408347.2011.521729.

[155] H. Zhang, Z. Sun, Y.H. Hu, Steam reforming of methane: Current states of catalyst design and process upgrading, Renew. Sustain. Energy Rev. 149 (2021) 111330. https://doi.org/10.1016/j.rser.2021.111330.

[156] D.. Wilhelm, D.. Simbeck, A.. Karp, R.. Dickenson, Syngas production for gas-to-liquids applications: technologies, issues and outlook, Fuel Process. Technol. 71 (2001) 139–148. https://doi.org/10.1016/S0378-3820(01)00140-0.

[157] L. Soares, C.H. Gonçalves de Brito, C. Maia, J.R. Sodré, OVERVIEW OF THE ETHANOL STEAM REFORMING FOR HYDROGEN PRODUCTION, in: Procceedings 24th ABCM Int. Congr. Mech. Eng., ABCM, 2017. https://doi.org/10.26678/ABCM.COBEM2017.COB17-2447.

[158] A.L. Chiew, N.A. Buckley, Carbon monoxide poisoning in the 21st century, Crit. Care. 18 (2014) 221. https://doi.org/10.1186/cc13846.

[159] D. Degler, S. Wicker, U. Weimar, N. Barsan, Identifying the active oxygen species in SnO_2 based gas sensing materials: An operando IR spectrsocopy study, J. Phys. Chem. C. 119 (2015) 11792–11799. https://doi.org/10.1021/acs.jpcc.5b04082.

[160] T. Hakkarainen, E. Mikkola, J. Laperre, F. Gensous, P. Fardell, Y. Le Tallec, C. Baiocchi, K. Paul, M. Simonson, C. Deleu, E. Metcalfe, Smoke gas analysis by Fourier transform infrared spectroscopy - summary of the SAFIR project results, Fire Mater. 24 (2000) 101–112. https://doi.org/10.1002/1099-1018(200003/04)24:2<101::AID-FAM729>3.0.CO;2-2.

[161] M. Takeuchi, L. Bertinetti, G. Martra, S. Coluccia, M. Anpo, States of H_2O adsorbed on oxides: An investigation by near and mid infrared spectroscopy, Appl. Catal. A Gen. 307 (2006) 13–20. https://doi.org/10.1016/j.apcata.2006.03.002.

[162] J.H. Anderson, K.A. Wickersheim, Near infrared characterization of water and hydroxyl groups on silica surfaces, Surf. Sci. 2 (1964) 252–260. https://doi.org/10.1016/0039-6028(64)90064-0.

[163] D.A. Panayotov, J.T. Yates, Depletion of conduction band electrons in TiO_2 by water chemisorption - IR spectroscopic studies of the independence of Ti-OH frequencies on electron concentration, Chem. Phys. Lett. 410 (2005) 11–17. https://doi.org/10.1016/j.cplett.2005.03.146.

[164] A.A. Bunaciu, H.Y. Aboul-Enein, Vibrational Spectroscopy Applications in Drugs Analysis, in: Encycl. Spectrosc. Spectrom., Elsevier, 2017: pp. 575–581. https://doi.org/10.1016/B978-0-12-409547-2.12214-0.

[165] T.H. Tan, J. Scott, Y.H. Ng, R.A. Taylor, K.F. Aguey-Zinsou, R. Amal, C-C Cleavage by Au/TiO_2 during Ethanol Oxidation: Understanding Bandgap Photoexcitation and Plasmonically Mediated Charge Transfer via Quantitative in Situ DRIFTS, ACS Catal. 6 (2016) 8021–8029. https://doi.org/10.1021/acscatal.6b01833.

[166] S.S. Shendage, V.L. Patil, S.A. Vanalakar, S.P. Patil, N.S. Harale, J.L. Bhosale, J.H. Kim, P.S. Patil, Sensitive and selective NO_2 gas sensor based on WO_3 nanoplates, Sensors Actuators, B Chem. 240 (2017) 426–433. https://doi.org/10.1016/j.snb.2016.08.177.

[167] J. Huang, X. Xu, C. Gu, M. Yang, M. Yang, J. Liu, Large-scale synthesis of hydrated tungsten oxide 3D architectures by a simple chemical solution route and their gas-sensing properties, J. Mater. Chem. 21 (2011) 13283. https://doi.org/10.1039/c1jm11292a.

[168] T. Li, W. Zeng, B. Miao, S. Zhao, Y. Li, H. Zhang, Urchinlike hex-WO_3 microspheres: Hydrothermal synthesis and gas-sensing properties, Mater. Lett. 144 (2015) 106–109. https://doi.org/10.1016/j.matlet.2015.01.019.

[169] B. Miao, W. Zeng, Y. Mu, W. Yu, S. Hussain, S. Xu, H. Zhang, T. Li, Controlled synthesis of monodisperse $WO_3 \cdot H_2O$ square nanoplates and their gas sensing properties, Appl. Surf. Sci. 349 (2015) 380–386. https://doi.org/10.1016/j.apsusc.2015.04.226.

[170] W. Zeng, B. Miao, T. Li, H. Zhang, S. Hussain, Y. Li, W. Yu, Hydrothermal synthesis, characterization of h-WO_3 nanowires and gas sensing of thin film sensor based on this powder, Thin Solid Films. 584 (2015) 294–299. https://doi.org/10.1016/j.tsf.2014.12.037.

[171] W. Xu, C. Qiu, J. Zhou, Y. Chen, Regulation of specific surface area of 3D flower-like WO_3 hierarchical structures for gas sensing application, Ceram. Int. 46 (2020) 11372–11378. https://doi.org/10.1016/j.ceramint.2020.01.167.

[172] R. Li, S. Chen, Z. Lou, L. Li, T. Huang, Y. Song, D. Chen, G. Shen, Fabrication of porous SnO_2 nanowires gas sensors with enhanced sensitivity, Sensors Actuators B Chem. 252 (2017) 79–85. https://doi.org/10.1016/j.snb.2017.05.161.

[173] L. Zhang, R. Tong, W. Ge, R. Guo, S.E. Shirsath, J. Zhu, Facile one-step hydrothermal synthesis of SnO_2 microspheres with oxygen vacancies for superior ethanol sensor, J. Alloys Compd. 814 (2020) 152266. https://doi.org/10.1016/j.jallcom.2019.152266.

[174] S. Zhao, Y. Shen, X. Yan, P. Zhou, Y. Yin, R. Lu, C. Han, B. Cui, D. Wei, Complex-surfactant-assisted hydrothermal synthesis of one-dimensional ZnO nanorods for high-performance ethanol gas sensor, Sensors Actuators B Chem. 286 (2019) 501–511. https://doi.org/10.1016/j.snb.2019.01.127.

[175] J. Tan, M. Dun, L. Li, J. Zhao, X. Li, Y. Hu, G. Huang, W. Tan, X. Huang, Self-template derived CuO nanowires assembled microspheres and its gas sensing properties, Sensors Actuators B Chem. 252 (2017) 1–8. https://doi.org/10.1016/j.snb.2017.05.107.

[176] Y. Liu, X. Li, Y. Wang, X. Li, P. Cheng, Y. Zhao, F. Dang, Y. Zhang, Hydrothermal synthesis of Au@SnO_2 hierarchical hollow microspheres for ethanol detection, Sensors Actuators B Chem. 319 (2020) 128299. https://doi.org/10.1016/j.snb.2020.128299.

[177] Y. Wang, H. Li, D. Huang, X. Wang, L. Cai, Y. Chen, W. Wang, Y. Song, G. Han, B. Zhen, A high-performance ethanol gas sensor based on Ce-doped SnO_2 nanomaterials prepared by the Pechini method, Mater. Sci. Semicond. Process. 137 (2022) 106188. https://doi.org/10.1016/j.mssp.2021.106188.

[178] X. Yang, H. Li, T. Li, Z. Li, W. Wu, C. Zhou, P. Sun, F. Liu, X. Yan, Y. Gao, X. Liang, G. Lu, Highly efficient ethanol gas sensor based on hierarchical SnO_2/Zn_2SnO_4 porous spheres, Sensors Actuators B Chem. 282 (2019) 339–346. https://doi.org/10.1016/j.snb.2018.11.070.

[179] J. Liu, T. Wang, B. Wang, P. Sun, Q. Yang, X. Liang, H. Song, G. Lu, Highly sensitive and low detection limit of ethanol gas sensor based on hollow ZnO/SnO_2 spheres composite material, Sensors Actuators B Chem. 245 (2017) 551–559. https://doi.org/10.1016/j.snb.2017.01.148.

[180] H. Fan, X. Zheng, Q. Shen, W. Wang, W. Dong, Hydrothermal synthesis and their ethanol gas sensing performance of 3-dimensional hierarchical nano Pt/SnO_2, J. Alloys Compd. 909 (2022) 164693. https://doi.org/10.1016/j.jallcom.2022.164693.

[181] P. Das, B. Mondal, K. Mukherjee, Simultaneous Adsorption–Desorption Processes in the Conductance Transient of Anatase Titania for Sensing Ethanol: A Distinctive Feature with Kinetic Perception, J. Phys. Chem. C. 121 (2017) 1146–1152. https://doi.org/10.1021/acs.jpcc.6b10041.

[182] A. Umar, H.Y. Ammar, R. Kumar, T. Almas, A.A. Ibrahim, M.S. AlAssiri, M. Abaker, S. Baskoutas, Efficient H2 gas sensor based on 2D SnO_2 disks: Experimental and theoretical studies, Int. J. Hydrogen Energy. 45 (2020) 26388–26401. https://doi.org/10.1016/j.ijhydene.2019.04.269.

[183] F. Wang, K. Hu, H. Liu, Q. Zhao, K. Wang, Y. Zhang, Low temperature and fast response hydrogen gas sensor with Pd coated SnO_2 nanofiber rods, Int. J. Hydrogen Energy. 45 (2020) 7234–7242. https://doi.org/10.1016/j.ijhydene.2019.12.152.

[184] L. Liu, C. Guo, S. Li, L. Wang, Q. Dong, W. Li, Improved H_2 sensing properties of Co-doped SnO_2 nanofibers, Sensors Actuators B Chem. 150 (2010) 806–810. https://doi.org/10.1016/j.snb.2010.07.022.

[185] W. Ding, N. Ansari, Y. Yang, K. Bachagha, Superiorly sensitive and selective H_2 sensor based on p-n heterojunction of WO_3–CoO nanohybrids and its sensing mechanism, Int. J. Hydrogen Energy. 46 (2021) 28823–28837. https://doi.org/10.1016/j.ijhydene.2021.06.070.

[186] U.T. Nakate, G.H. Lee, R. Ahmad, P. Patil, Y.-B. Hahn, Y.T. Yu, E. Suh, Nano-bitter gourd like structured CuO for enhanced hydrogen gas sensor application, Int. J. Hydrogen Energy. 43 (2018) 22705–22714. https://doi.org/10.1016/j.ijhydene.2018.09.162.

[187] S. Agarwal, S. Kumar, H. Agrawal, M.G. Moinuddin, M. Kumar, S.K. Sharma, K. Awasthi, An efficient hydrogen gas sensor based on hierarchical Ag/ZnO hollow microstructures, Sensors Actuators B Chem. 346 (2021) 130510. https://doi.org/10.1016/j.snb.2021.130510.

[188] A. GERVASINI, Acidity and basicity of metal oxide surfaces II. Determination by catalytic decomposition of isopropanol, J. Catal. 131 (1991) 190–198. https://doi.org/10.1016/0021-9517(91)90335-2.

[189] G. Busca, The surface acidity of solid oxides and its characterization by IR spectroscopic methods. An attempt at systematization, Phys. Chem. Chem. Phys. 1 (1999) 723–736.

https://doi.org/10.1039/a808366e.

[190] A.E.-A. A. Said, M.M.M.A. El-Wahab, M.A. El-Aal, The Role of Acid Sites in the Catalytic Performance of Tungsten Oxide during the Dehydration of Isopropyl and Methyl Alcohols, Chem. Mater. Eng. 4 (2016) 17–25. https://doi.org/10.13189/cme.2016.040202.

[191] A.K. Nayak, R. Ghosh, S. Santra, P.K. Guha, D. Pradhan, Hierarchical nanostructured WO_3 – SnO_2 for selective sensing of volatile organic compounds, Nanoscale. 7 (2015) 12460–12473. https://doi.org/10.1039/C5NR02571K.

[192] D. Zhao, X. Zhang, L. Sui, W. Wang, X. Zhou, X. Cheng, S. Gao, Y. Xu, L. Huo, C-doped TiO_2 nanoparticles to detect alcohols with different carbon chains and their sensing mechanism analysis, Sensors Actuators B Chem. 312 (2020) 127942. https://doi.org/10.1016/j.snb.2020.127942.

[193] C. Wang, Y. Zhang, X. Sun, Y. Sun, F. Liu, X. Yan, C. Wang, P. Sun, L. Geyu, Fast detection of alcohols by novel sea cucumber-like indium tungsten oxide, Sensors Actuators B Chem. 319 (2020) 128158. https://doi.org/10.1016/j.snb.2020.128158.

[194] A. Sáaedi, P. Shabani, R. Yousefi, High performance of methanol gas sensing of ZnO/PAni nanocomposites synthesized under different magnetic field, J. Alloys Compd. 802 (2019) 335–344. https://doi.org/10.1016/j.jallcom.2019.06.088.

[195] W. Liu, X. Zhang, Z. Wang, R. Wang, C. Chen, C. Dong, Nanoparticles Assembled $CdIn_2O_4$ Spheres with High Sensing Properties towards n-Butanol, Nanomaterials. 9 (2019) 1714. https://doi.org/10.3390/nano9121714.

[196] L. Biette, F. Carn, M. Maugey, M.-F. Achard, J. Maquet, N. Steunou, J. Livage, H. Serier, R. Backov, Macroscopic Fibers of Oriented Vanadium Oxide Ribbons and Their Application as Highly Sensitive Alcohol Microsensors, Adv. Mater. 17 (2005) 2970–2974. https://doi.org/10.1002/adma.200501368.

[197] B. Sakintuna, O. Çuhadar, Y. Yürüm, Diffusion of Volatile Organic Chemicals in Porous Media. 2. Alcohol/Templated Porous Carbon Systems, Energy & Fuels. 20 (2006) 1269–1274. https://doi.org/10.1021/ef0503461.

[198] W.-T. Koo, H.-J. Cho, D.-H. Kim, Y.H. Kim, H. Shin, R.M. Penner, I.-D. Kim, Chemiresistive Hydrogen Sensors: Fundamentals, Recent Advances, and Challenges, ACS Nano. 14 (2020) 14284–14322. https://doi.org/10.1021/acsnano.0c05307.

[199] A.S. Mokrushin, T.L. Simonenko, N.P. Simonenko, P.Y. Gorobtsov, N.C. Kadyrov, E.P. Simonenko, V.G. Sevastyanov, N.T. Kuznetsov, Chemoresistive gas-sensing properties of highly dispersed Nb_2O_5 obtained by programmable precipitation, J. Alloys Compd. 868 (2021) 159090. https://doi.org/10.1016/j.jallcom.2021.159090.

[200] M. Egashira, M. Nakashima, S. Kawasumi, T. Selyama, Temperature programmed desorption study of water adsorbed on metal oxides. 2. Tin oxide surfaces, J. Phys. Chem. 85 (1981) 4125–4130. https://doi.org/10.1021/j150626a034.

[201] A. V. Bandura, J.D. Kubicki, J.O. Sofo, Comparisons of Multilayer H_2O Adsorption onto the (110) Surfaces of α-TiO_2 and SnO_2 as Calculated with Density Functional Theory, J. Phys. Chem. B. 112 (2008) 11616–11624. https://doi.org/10.1021/jp711763y.

[202] G. Korotcenkov, V. Golovanov, V. Brinzari, A. Cornet, J. Morante, M. Ivanov, Distinguishing feature of metal oxide films' structural engineering for gas sensor applications, J. Phys. Conf. Ser. 15 (2005) 256–261. https://doi.org/10.1088/1742-6596/15/1/043.

[203] S. Cao, C. Zhao, T. Han, L. Peng, Hydrothermal synthesis, characterization and gas sensing

properties of the WO_3 nanofibers, Mater. Lett. 169 (2016) 17–20. https://doi.org/10.1016/j.matlet.2016.01.053.

[204] T.-A. Nguyen, S. Park, J.B. Kim, T.K. Kim, G.H. Seong, J. Choo, Y.S. Kim, Polycrystalline tungsten oxide nanofibers for gas-sensing applications, Sensors Actuators B Chem. 160 (2011) 549–554. https://doi.org/10.1016/j.snb.2011.08.028.

[205] J. Leng, X. Xu, N. Lv, H. Fan, T. Zhang, Synthesis and gas-sensing characteristics of WO_3 nanofibers via electrospinning, J. Colloid Interface Sci. 356 (2011) 54–57. https://doi.org/10.1016/j.jcis.2010.11.079.

[206] D.-H. Kim, J.-S. Jang, W.-T. Koo, S.-J. Choi, H.-J. Cho, M.-H. Kim, S.-J. Kim, I.-D. Kim, Bioinspired Cocatalysts Decorated WO_3 Nanotube Toward Unparalleled Hydrogen Sulfide Chemiresistor, ACS Sensors. 3 (2018) 1164–1173. https://doi.org/10.1021/acssensors.8b00210.

[207] W.-T. Koo, S.-J. Choi, N.-H. Kim, J.-S. Jang, I.-D. Kim, Catalyst-decorated hollow WO_3 nanotubes using layer-by-layer self-assembly on polymeric nanofiber templates and their application in exhaled breath sensor, Sensors Actuators B Chem. 223 (2016) 301–310. https://doi.org/10.1016/j.snb.2015.09.095.

[208] X. Shen, G. Wang, D. Wexler, Large-scale synthesis and gas sensing application of vertically aligned and double-sided tungsten oxide nanorod arrays, Sensors Actuators B Chem. 143 (2009) 325–332. https://doi.org/10.1016/j.snb.2009.09.015.

[209] B. Behera, S. Chandra, Synthesis of WO_3 nanorods by thermal oxidation technique for NO_2 gas sensing application, Mater. Sci. Semicond. Process. 86 (2018) 79–84. https://doi.org/10.1016/j.mssp.2018.06.022.

[210] Z.-X. Cai, H.-Y. Li, X.-N. Yang, X. Guo, NO sensing by single crystalline WO_3 nanowires, Sensors Actuators B Chem. 219 (2015) 346–353. https://doi.org/10.1016/j.snb.2015.05.036.

[211] S. Zeb, X. Peng, G. Yuan, X. Zhao, C. Qin, G. Sun, Y. Nie, Y. Cui, X. Jiang, Controllable synthesis of ultrathin WO_3 nanotubes and nanowires with excellent gas sensing performance, Sensors Actuators B Chem. 305 (2020) 127435. https://doi.org/10.1016/j.snb.2019.127435.

[212] J. Ma, J. Zhang, S. Wang, T. Wang, J. Lian, X. Duan, W. Zheng, Topochemical Preparation of WO_3 Nanoplates through Precursor H_2WO_4 and Their Gas-Sensing Performances, J. Phys. Chem. C. 115 (2011) 18157–18163. https://doi.org/10.1021/jp205782a.

[213] Z. Wang, M. Hu, Y. Wei, J. Liu, Y. Qin, Low-temperature NO2-sensing properties and morphology-controllable solvothermal synthesis of tungsten oxide nanosheets/nanorods, Appl. Surf. Sci. 362 (2016) 525–531. https://doi.org/10.1016/j.apsusc.2015.11.140.

[214] A. M. Maghraby, Introductory Chapter: Electron Paramagnetic Resonance, in: Top. From EPR Res., IntechOpen, 2019. https://doi.org/10.5772/intechopen.83028.

[215] J.K. Burdett, T. Hughbanks, G.J. Miller, J.W. Richardson, J. V. Smith, Structural-electronic relationships in inorganic solids: powder neutron diffraction studies of the rutile and anatase polymorphs of titanium dioxide at 15 and 295 K, J. Am. Chem. Soc. 109 (1987) 3639–3646. https://doi.org/10.1021/ja00246a021.

[216] P. Ballirano, R. Caminiti, Rietveld refinements on laboratory energy dispersive X-ray diffraction (EDXD) data, J. Appl. Crystallogr. 34 (2001) 757–762. https://doi.org/10.1107/S0021889801014728.

[217] W.H. Baur, A.A. Khan, Rutile-type compounds. IV. SiO_2, GeO_2 and a comparison with other rutile-type structures, Acta Crystallogr. Sect. B Struct. Crystallogr. Cryst. Chem. 27 (1971) 2133–2139. https://doi.org/10.1107/S0567740871005466.

[218] A.A. Bolzan, C. Fong, B.J. Kennedy, C.J. Howard, Structural Studies of Rutile-Type Metal Dioxides, Acta Crystallogr. Sect. B Struct. Sci. 53 (1997) 373–380. https://doi.org/10.1107/S0108768197001468.

[219] D.T. Cromer, K. Herrington, The Structures of Anatase and Rutile, J. Am. Chem. Soc. 77 (1955) 4708–4709. https://doi.org/10.1021/ja01623a004.

[220] W. Gonschorek, X-ray charge density study of rutile (TiO_2), Zeitschrift Für Krist. 160 (1982) 187–203. https://doi.org/10.1524/zkri.1982.160.3-4.187.

[221] J. Haines, J.M. Léger, X-ray diffraction study of the phase transitions and structural evolution of tin dioxide at high pressure:ffRelationships between structure types and implications for other rutile-type dioxides, Phys. Rev. B. 55 (1997) 11144–11154. https://doi.org/10.1103/PhysRevB.55.11144.

[222] C.M.B. Henderson, K.S. Knight, A.R. Lennie, Temperature Dependence of Rutile (TiO_2) and Geikielite ($MgTiO_3$) Structures Determined Using Neutron Powder Diffraction, Open Mineral. J. 3 (2009) 1–11. https://doi.org/10.2174/1874456700903010001.

[223] K.M.Ø. Jensen, M. Christensen, P. Juhas, C. Tyrsted, E.D. Bøjesen, N. Lock, S.J.L. Billinge, B.B. Iversen, Revealing the Mechanisms behind SnO_2 Nanoparticle Formation and Growth during Hydrothermal Synthesis: An In Situ Total Scattering Study, J. Am. Chem. Soc. 134 (2012) 6785–6792. https://doi.org/10.1021/ja300978f.

[224] R. Restori, D. Schwarzenbach, J.R. Schneider, Charge density in rutile, TiO_2, Acta Crystallogr. Sect. B Struct. Sci. 43 (1987) 251–257. https://doi.org/10.1107/S0108768187097921.

[225] H. SEKI, N. ISHIZAWA, N. MIZUTANI, M. KATO, High Temperature Structures of the Rutile-Type Oxides, TiO_2 and SnO_2, J. Ceram. Assoc. Japan. 92 (1984) 219–223. https://doi.org/10.2109/jcersj1950.92.1064_219.

Activity Report

During my Doctorate, I focused on the synthesis of nanostructured metal-oxide semiconductors for the fabrication of chemoresistive gas sensors. I dealt with the synthesis of the materials, the production of the sensitive films as well as their electrical characterization and sensing measurements. After the selection of the most promising samples, I followed their chemical-physical characterization in collaboration with experts in techniques for morphological, chemical and structural investigations. Then, I used all of the information to build an overview for understanding the sensor's features.

The research of the first year concerned the production of nanostructured films based on 1D and 2D WO_3 synthetized through solvothermal techniques. The performances of these sensors have been compared with nanograined-based WO_3 for internal laboratory evaluations. Unfortunately, WO_3 nanowires-based sensors were highly unstable and failed to complete electrical characterizations. Therefore, only the research on WO_3 nanoflakes-based sensors has been accomplished.

During the second and third year, I concentrated on the optimization of the solid solution based on $(Sn,Ti,Nb)_xO_2$ for gas sensing. This was compared to previous materials accessible in our groups, i.e. SnO_2 and $Sn_{70}Ti_{30}O_2$. Work on this material took longer since several tests were performed to better grasp its potential. Additionally, the comprehension of its chemical-physical properties and surface reactivity required the application of many techniques, including operando DRIFT spectroscopy.

In parallel with the work presented in this thesis, I collaborated in further activities within the research group headed by Professor Guidi. Firstly, I assisted in clarifying the ambient stability and gas sensing mechanism of nickel-decorated phosphorous for NO_2 detection. Secondly, I contributed to the comprehension of DRIFT spectra taken on nanostructured $SiC-SiO_xC$ for the investigation of its SO_2 sensing mechanism. Finally, I aided in the synthesis and characterization of a sensor for CO_2 detection, as well as in the subsequent drafting for patent pending publication.

In addition to the research on gas sensors, I also collaborated on the project CAT-SOS won by professor Ardit for advanced capture of SO_2 and SVHC from industrial emissions (https://www2.unife.it/at/altri-contenuti/2021/bando-per-il-finanziamento-della-ricerca-scientifica-fondo-per-lincentivazione-alla-ricerca-fir-anno-2016).

Publications

Articles in peer review journals:

- E. Spagnoli, S. Krik, B. Fabbri, M. Valt, A. Gaiardo, M. Ardit, M. Della Ciana, V. Cristino, G. Vola, S. Caramori, C. Malagù, V. Guidi, *Development and characterization of WO_3 nanoflakes for selective ethanol sensing*, Sensors and Actuators B: Chemical 347 (**2021**) 130593 https://doi.org/10.1016/j.snb.2021.130593
- E. Spagnoli, A. Gaiardo, B. Fabbri, M. Valt, S. Krik, M. Ardit, G. Cruciani, M. Della Ciana, L. Vanzetti, G.Vola, S. Gherardi, P. Bellutti, C. Malagu, and V. Guidi, *Design of a Metal-Oxide Solid Solution for Sub-ppm H_2 Detection*, ACS Sens. **2022**, 7, 573−583 https://doi.org/10.1021/acssensors.1c02481
- S. Krik, M. Valt, A. Gaiardo, B. Fabbri, E. Spagnoli, C. Malagù, M. Caporali, P. Belluti, V. Guidi, *Elucidating the Ambient Stability and Gas Sensing Mechanism of Nickel-Decorated Phosphorene for NO_2 Detection: A First-Principles Study*, ACS Omega **2022**, 7, 9808−9817 https://doi.org/10.1021/acsomega.2c00078
- E. Spagnoli, B. Fabbri, A. Gaiardo, M. Valt, M. Ardit, S. Krik, G. Cruciani, M. Della Ciana, L. Vanzetti, G. Vola, F. Di Benedetto, A. Migliori, C. Malagù, V. Guidi *Design of a metal-oxide solid solution for selective detection of ethanol with marginal influence by humidity*, Sensors & Actuators: B. Chemical 370 (**2022**) 132426 https://doi.org/10.1016/j.snb.2022.132426
- M. Della Ciana, M. Valt, B. Fabbri, A. Gaiardo, E. Spagnoli, S. Krik, P. Bernardoni, N. Gilli, A. Migliori, A. Quaranta, V. Morandi, V. Guidi, *SO_2 sensing mechanism of nanostructured SiC-SiOxC core shell: An operando DRIFT investigation*, Sensors & Actuators: B. Chemical 371 (**2022**) 132497 https://doi.org/10.1016/j.snb.2022.132497

Patent:

GUIDI Vincenzo, FABBRI Barbara, ROSSI Arianna, SPAGNOLI Elena, INVENTORI. A nome Università degli Studi di Ferrara. *Materiale semiconduttore nanostrutturato per la rilevazione di anidride carbonica*. Domanda di brevetto nazionale IT n. 102022000022314 del 28/10/2022.

Oral presentation at Conferences:

- E. Spagnoli, M. Valt, B. Fabbri, M. Ardit, V. Cristin, M. Della Ciana, A. Gaiardo, S. Krik, G. Zonta, S. Caramori, C. Malagù, V. Guidi, *WO_3 Nanoparticles and Nanoflakes Based Sensors for Selective Detection of Alcohols*, 2021 Meet. Abstr. MA2021-01 1437, https://iopscience.iop.org/article/10.1149/MA2021-01561437mtgabs/meta
- E. Spagnoli, M. Valt, B. Fabbri, M. Ardit, V. Cristino, M. Della Ciana, A. Gaiardo, G. Zonta, S. Caramori, C. Malagù, and V. Guidi, *WO_3 Nanoparticles and Nanoflakes Based Sensors for Selective Detection of Alcohols*, IMCS 2021, 30 Maggio – 3 Giugno 2021, USA
- E. Spagnoli, M. Valt, B. Fabbri, M. Ardit, V. Cristino, M. Della Ciana, A. Gaiardo, S. Krik, G. Zonta, S. Caramori, C. Malagù, and V. Guidi, *WO_3 Nanoflakes Based Sensors for Selective Detection of Ethanol*, NewTimes, 14-18 Giugno 2021, L'Aquila

- E. Spagnoli, A. Gaiardo, B. Fabbri, M. Valt, S. Krik, M. Ardit, G. Cruciani, M. Della Ciana, L. Vanzetti, S. Gherardi, P. Bellutti, G. Vola , C. Malagù, V. Guidi, *$(Sn,Ti,Nb)_xO_2$ Solid Solution: an Innovative Sensing Material for H_2 Detection, Sensors* 2021, 20-22 Ottobre 2021, Milano
- E. Spagnoli, A. Gaiardo, B. Fabbri, M. Valt, S. Kri1, M. Ardit, G. Cruciani, M. Della Ciana, L. Vanzetti, S. Gherardi, C. Malagù, P. Bellutti, V. Guidi, *Gas sensing properties of $(Sn,Ti,Nb)_xO_2$ solid solution* PhD GOSPEL Workshop 2022, 1 Giugno 2022 (LECTURE)
- E. Spagnoli, A. Gaiardo, B. Fabbria, M. Valt, S. Krik, M. Ardit, M. Della Ciana, L. Vanzetti, C. Malagù, V. Guidi, *Nanostructured $(Sn,Ti,Nb)_xO_2$ Solid Solution for Gas Sensing Applications*, Future Material 2022, 3-7 Ottobre 2022, Roma
- E. Spagnoli, A. Gaiardo, B. Fabbri, M. Valt, S. Krik, M. Ardit, M. Della Ciana, C. Malagù, V. Guidi, *Design of a Nanostructured Metal-Oxide Solid Solution Based on Sn, Ti, Nb for Gas Sensing Applications*, SEMICONMEET2022, 12-14 Settembre 2022, Barcellona, Spagna (INVITED)
- E. Spagnoli, M. Valt, B. Fabbri, M. Ardit, V. Cristino, M. Della Ciana , A. Gaiardo, S. Caramori, V. Guidi, *Influence of Morphology in WO_3-Based Gas Sensors for Selective Detection of Alcohols*, From surfaces to devices: novel perspectives from nanostructured oxides and carbon materials, 12-13 Dicembre 2022, Brescia

Poster Presentation at Conference:

- Elena Spagnoli, Andrea Gaiardo, Barbara Fabbri, Matteo Valt, Matteo Ardit, Soufiane Krik, Michele Della Ciana, Lia Vanzetti, Gabriele Vola, Vincenzo Guidi, *Design of a Nanostructured Metal-Oxide Solid Solution for Gas Sensing Applications*, Seventh International Conference on Multifunctional, Hybrid and Nanomaterials (HYMA 2022), 19 -22 Ottobre 2022, Genova